ORNL/TM-2003/222

NUCLEAR ENERGY RESEARCH INITIATIVE (NERI)

Forewarning of Failure in Critical Equipment at Next-Generation Nuclear Power Plants
NERI Project #2000-0109
FINAL PROJECT REPORT

Lee M. Hively
Vladimir A. Protopopescu
Oak Ridge National Laboratory

Karl M. Reichard
Kenneth P. Maynard
Pennsylvania State University, Applied Research Laboratory
(Collaborating Organization)

October 24, 2003

ORNL/TM/2003-222

FOREWARNING OF FAILURE IN CRITICAL EQUIPMENT AT NEXT-GENERATION NUCLEAR POWER PLANTS

Lee M. Hively
Vladimir A. Protopopescu

October 24, 2003

TABLE OF CONTENTS

Page

LIST OF TABLES

Table **Page**

LIST OF FIGURES

Figure **Page**

LIST OF FIGURES (continued)

Figure **Page**

EXECUTIVE SUMMARY

Title: Forewarning of Failure in Critical Equipment at Next-Generation Nuclear Power Plants
Investigator: Dr. Lee M. Hively (Oak Ridge National Laboratory, Oak Ridge, TN)
Collaborators: Duke Engineering and Services Inc.; Pennsylvania State University
Project # 00-109
Start Date: August 18, 2000
End Date: September 30, 2003

The objective of this project is forewarning of machine failures in critical equipment at next-generation nuclear power plants (NPP). Test data were provided by two collaborating institutions: Duke Engineering and Services (first project year), and the Pennsylvania State University (Applied Research Laboratory) during the second and third project years. New nonlinear methods were developed and applied successfully to extract forewarning trends from process-indicative, time-serial data for timely, condition-based maintenance. Anticipation of failures in critical equipment at next-generation NPP will improve the scheduling of maintenance activities to minimize safety concerns, unscheduled non-productive downtime, and collateral damage due to unexpected failures. This approach provides significant economic benefit, and is expected to improve public acceptance of nuclear power.

The approach is a multi-tiered, model-independent, and data-driven analysis that uses ORNL's novel nonlinear method to extract forewarning of machine failures from appropriate data. The first tier of the analysis provides a robust choice for the process-indicative data. The second tier rejects data of inadequate quality. The third tier removes signal artifacts that would otherwise confound the analysis, while retaining the relevant nonlinear dynamics. The fourth tier converts the artifact-filtered time-serial data into a geometric representation, that is then transformed to a discrete distribution function (DF). This method allows for noisy, finite-length datasets. The fifth tier obtains dissimilarity measures (DM) between the nominal-state DF and subsequent test-state DFs. Forewarning of a machine failure is indicated by several successive occurrences of the DM above a threshold, or by a statistically significant trend in the DM. This paradigm yields robust nonlinear signatures of degradation and its progression, allowing earlier and more accurate detection of the machine failure.

Project-year-1 (PY1) results were as follows. Long-term failure monitoring of operational equipment was not feasible within the scope of this project since such failures typically take years to occur. Instead, data were acquired from a motor-driven pump for two test sequences, initially in nominal operation and subsequently with progressively larger (seeded) faults. Specifically, the experimenters carefully added larger amounts of mass imbalance in one test, and increasing misalignment between the motor and pump in the second test. ORNL's nonlinear measures of condition change correlated well with the experimental level of vibration, both below and above the applicable international standards (ISO 2372 and ISO 3945). The work included a robust implementation of the nonlinear analysis on a desktop computer, not unlike that for use at an advanced nuclear reactor.

PY2 results involved acquisition and analysis of additional test data, as summarized in Table 1. Some test sequences involved seeded faults (denoted by 'S' in Table 1), with the equipment initially in nominal operation, and subsequently with successively larger (controlled) faults. A second class of *accelerated* failure tests (denoted by 'A' in Table 1) likewise began with nominal operation. The over-stressed equipment subsequently experienced a gradual (uncontrolled) degradation, and ultimately failed. For example, the gearbox failed by the breakage of one or more gear teeth. Table 1 also shows the type of diagnostic data that was analyzed for failure forewarning. Electrical motor power was obtained from the three-phase motor currents and voltages. Vibration power was obtained from tri-axial acceleration data to capture the dynamics from all three acceleration directions. ORNL's patented nonlinear measures show clear change, as the tests progress from nominal operation, through degradation to failure for all nine PY2 test sequences. (Conventional statistical measures and traditional nonlinear measures give little if any forewarning.) This work also yielded a statistical criterion that distinguishes between the gradual rise in dissimilarity measures and the abrupt (additional) increase that gives forewarning of failure.

Table 1. Summary of Test Sequences

Data Provider	Equipment and Type of Failure	Diagnostic Data	PY
1) EPRI (S)	800-HP electric motor: air-gap offset	motor power	2
2) EPRI (S)	800-HP electric motor: broken rotor	motor power	2
3) EPRI (S)	500-HP electric motor: turn-to-turn short	motor power	2
4) Otero/Spain (S)	¼-HP electric motor: imbalance	acceleration	2
5) PSU/ARL (A)	30-HP motor: overloaded gearbox	load torque	2
6) PSU/ARL (A)	30-HP motor: overloaded gearbox	vibration power	2
7) PSU/ARL (A)	30-HP motor: overloaded gearbox	vibration power	2
8) PSU/ARL (S)	crack in rotating blade	motor power	2
9) PSU/ARL (A)	motor-driven bearing	vibration power	2
10) EPRI (S)	800-HP electric motor: air-gap offset	vibration power	3
11) EPRI (S)	800-HP electric motor: broken rotor	vibration power	3
12) EPRI (S)	500-HP electric motor: turn-to-turn short	vibration power	3
13) PSU/ARL (A)	30-HP motor: overloaded gearbox	vibration power	3
14) PSU/ARL (A)	30-HP motor: overloaded gearbox	vibration power	3
15) PSU/ARL (A)	30-HP motor: overloaded gearbox	vibration power	3
16) PSU/ARL (A)	30-HP motor: overloaded gearbox	vibration power	3
17) PSU/ARL (S)	crack in rotating blade	vibration power	3

PY3 results involved acquisition and analysis of additional test data, as summarized in Table 1. Items 10−12 during PY3 involved analysis of vibration power, while items 1−3 during PY2 used electrical motor power from the same test sequences. Items 13−15 involved the same test apparatus and protocol as items 5−7 to acquire additional test sequences. The PY3 results for items 10−16 showed clear forewarning reproducibility. In particular, four accelerated tests of gearbox failure gave end-of-life forewarning at 93.8–98.5% of the final failure time, as well as indication of the failure onset at 99–99.8% of the final failure time. The present results show no

false-negative indications (lack of forewarning when a change actually occurred), and no false-positive forewarnings (forewarning when no change really occurred). These results provide compelling evidence for forewarning of failures via the ORNL nonlinear paradigm. We also find that accurate forewarning can markedly reduce failures and improve cost-effectiveness.

Products of this work include U.S. Patents, patents pending, technical publications, oral presentations, and software implementation of the nonlinear technology. In addition, this work illustrates the cost-benefits for the prognostication technology via specific examples. Our work also provides a roadmap to bridge the gap from the present research-class technology to a commercial prototype. There are no software deliverables for this project. The ORNL nonlinear forewarning technology has substantial intellectual property protection in the form of six U.S. Patents and two patents pending. Two of these six patents were obtained during this NERI project, including an objective statistical test for the end-of-life forewarning and the failure onset indication. Both of the patents pending were submitted to the U.S. Patent Office during this NERI project to protect ideas that arose from this work. No licensing agreements presently exist for use of these patents. We have published six technical reports and four oral presentations on this NERI work. The work was completed on September 30, 2003.

1. TECHNICAL NARRATIVE

This project began in August 2000, and has three tasks. The first project year addressed Task 1, namely development of nonlinear prognostication for critical equipment in nuclear power facilities. That work is described in the first year's annual report. The second project year (FY02) addressed Task 2. The third project year addresses Tasks 2−3. This report describes the work status for the third (and final) project year, spanning August 2002 through September 2003, including the status of the tasks, issues/concerns for each task, cost performance, and status summary of tasks.

The objective of the third year's work is a compelling demonstration of the nonlinear prognostication algorithm via additional data and assessment of the economic impact of that prognostication. While long-term monitoring of operational utility equipment is possible in principle, it was not practically feasible for the following reason. Time and funding constraints for this project did not allow us to monitor the many components and machines (thousands) that will be necessary to obtain even a few failure sequences, due to relatively low failure/fault rates ($<10^{-3}$/year) in the operational environment. Consequently, we obtained controlled failure sequences by seeding progressively larger faults in test equipment. This method is the only way to guarantee a known, well-documented fault that leads to failure, but in general is infeasible for operational utility machinery. During the second project year, we also used accelerated failure testing, which eventually results in equipment breakdown, but in a less controlled fashion. Our subcontractor, Applied Research Laboratory at the Pennsylvania State University (PSU), provides test-sequence data, that Oak Ridge National Laboratory (ORNL) subsequently analyzes for prognostication. Recognizing the inherent constraints outlined above, ORNL contacted other researchers for additional data from a variety of test equipment. Consequently, we have revised Task 2, with corresponding changes to the work plan as shown in the Status Summary of NERI Tasks (below).

Task 2.1: *ORNL will obtain test data from PSU/ARL and other researchers for various test equipment. This task includes development of a test plan or a description of the historical testing, as appropriate: test facility, equipment to be tested, choice of failure mode, testing protocol, data acquisition equipment, and resulting data from the test sequence. ORNL will analyze this data for quality, and subsequently via the nonlinear paradigm for prognostication.*

Task 2.2: *ORNL will evaluate the prognostication capability of the nonlinear paradigm. The comparison metrics for reliability of the predictions will include the false positives, false negatives, and the forewarning times.*

Task 2.3: *ORNL will improve the nonlinear paradigm as appropriate, in accord with the results of Tasks 2.1−2.2, to minimize the number of false positive and false negative indications of failure, while maximizing the forewarning time.* (See App. A for details for the analysis methodology.)

Task 2.4: *ORNL will develop advanced algorithms for PS-DF* (phase space) *pattern change recognition, based on the results of Task 2.3. This implementation will provide a capability for*

prognostication, as a component of the long-term need for real-time maintenance decision-making.

The third phase of this work involves evaluation of the nonlinear paradigm, as described in Task 3.

Task 3.1: *This task will compare the economic and safety improvements for the nonlinear prognostication with previous efforts. Economic and quality gains will be documented.*

Task 3.2: *This task will map the pathway to potential commercialization of the nonlinear prognostication technology. Extrapolation of gains to other advanced reactor equipment will be included.*

We obtained and analyzed archival data from the Electric Power Research Institute (EPRI) during the second year's work of this project, as described in the FY02 annual report. EPRI published a report on that data and its analysis, "Electric Motor Predictive Maintenance Program," TR-108773-V2 (1999). The EPRI report included analysis of the safety and cost benefits of predictive maintenance that served as a guide for Task 3. Specifically, forewarning of an imminent failure allows the operator to anticipate or avoid the failure, thus avoiding concomitant damage (maintenance savings), downtime, lost generation capacity, potential injuries, and their associated costs.

Progress on Tasks 2.1–2.4 is described most easily for the acquisition and analysis of each sequence of test data, as described next. No issues or concerns exist for any components Tasks 2−3.

1.1 ADDITIONAL ANALYSIS OF EPRI MOTOR POWER DATA FOR THE AIRGAP-OFFSET FAULT

EPRI report # TR-108773-V2 (1999) included a CD-ROM of actual data from the testing. That work involved collaboration by several utilities and EPRI on seeded faults in large electric motors. The datasets were recorded in snap-shots of 1.5 s, sampled at 40 kHz (60,000 total time-serial samples), including three-phase voltages and currents, plus tri-axial accelerations at inboard and outboard locations on the motor. Several anomalies were introduced in the motors to simulate the most common pre-failure in-service conditions. ORNL has received data via the CD-ROM that accompanied the EPRI report for three different seeded faults. The specifications of the first motor were as follows.

Manufacturer:	Allis Chalmers	Bearing type:	sleeve
Rated voltage:	4160	Nameplate current:	100 amps
Rated HP:	800	Number of rotor bars:	94
Winding type:	form wound	Number of stator slots:	40
Phases:	3	Hertz:	60
RPM:	710	Motor type:	induction
Insulation class:	F	Poles:	10
Enclosure:	TEFC	Bar configuration:	copper

One test sequence began with the motor running in its nominal state (first dataset). Two different airgap-offset seeded-faults then were imposed via preinstalled jackscrews. The second dataset involved an inboard airgap offset of 8 mils from the nominal value of 30 mils. The third dataset retained the first fault, and added an additional seeded-fault outboard airgap offset by 20% in the opposite direction from the inboard shift. This additional fault resulted in the rotor being skewed relative to the stator. These offsets were static, because neither varied relative to the stator with the motor running.

We reiterate the PY2 analysis from the PY2 annual report, as a motivation for additional PY3 analysis. The three datasets for this test were concatenated into a single long dataset. Figure 1 shows typical three-phase voltages (V_i) and currents (I_i), that were converted into instantaneous motor power, $P = \Sigma_i I_i V_i$, where the sum runs over the three phases. The bottom subplot of Fig. 1 shows rich dynamical features in P, that are not present in the individual components of three-phase currents and voltages (upper six subplots). Consequently, we first analyzed the instantaneous power, rather than the individual currents or voltages. This power has a slow, low-amplitude variation with a period of roughly 0.1 s. We removed this artifact with ORNL's novel zero-phase quadratic filter. Otherwise, this artifact confounds the interpretation of our results. We split each of the three datasets into five subsets of 12,000 points each, giving fifteen total subsets for analysis. This artifact-filtered data showed no data quality problems. A systematic search revealed a set of parameters for which the phase-space dissimilarity measures (PSDM) are most sensitive to the condition change for the airgap seeded-fault test sequence, as shown in Fig. 2. An almost linear rise occurs in the connected-phase-space dissimilarities (second from the top and bottom plots) from near zero for the nominal state to approximately 20 for the double-seeded air-gap fault. The rise in non-connected dissimilarity measures is monotonic, but little changed between the two faulted states.

We performed additional analysis of this seeded-fault airgap test sequence during PY3. This analysis is motivated by the fact that electrical power is the sum of products of the three-phase currents and voltages. In principle, condition change should be extractable from one or more of the individual three-phase currents and voltages in this linear combination. Consequently, we determined the PSDM for each of the three-phase currents and voltages separately, using the same parameters as Fig. 2. Figure 3 shows an almost linear increase in $U(\chi^2)$ for V_1 (upper left subplot), and monotonic increases for the other three PSDM of V_1 (left column). All four PSDM of V_2 also increase monotonically (middle column of Fig. 3). Figure 3 also shows that $U(\chi^2)$ for V_3 (upper right subplot) increases monotonically, while the other three PSDM of V_3 rise from test No. 1 to test No. 2, then decrease for test No. 3. Figure 4 shows roughly linear increases in all four PSDM of I_2 (center column), and monotonic increases in all four PSDM of I_3 (right column). All four PSDM of I_1 increase from test No. 1 to test No. 2, then remain constant from test No. 2 to test No. 3. Figure 5 shows the PSDM for each component of three-phase power, $I_i V_i$. All four PSDM of $I_2 V_2$ (middle column) show an almost linear increase, and all four PSDM of $I_3 V_3$ increase monotonically. All four PSDM of $I_1 V_1$ increase from test No. 1 to test No. 2, then remain constant from test No. 2 to test No. 3. Thus, we find that the PSDM can extract condition change from most of the three-phase currents and voltages separately, as well as from two of the components of three-phase electrical power.

The EPRI data included tri-axial acceleration from inboard (IB) and outboard (OB) motor locations. However, the third component of the OB-acceleration failed the data quality check, due to initially small and erratic values, followed by an abrupt rise at 60 ms to a flat-top value. This problem continues periodically through the data, thus precluding use of the OB-accelerometer for condition change. Our analysis indicates adequate quality for the IB-acceleration data, which we analyze next. Tri-axial acceleration has an important advantage, as follows. Acceleration, $\underline{a}$, is a three-dimensional vector that can be integrated once in time to give velocity (vector), $\underline{v} = \int \underline{a}\, dt$. Mass, m, times acceleration (vector) is force (vector), $\underline{F} = m\underline{a}$. The dot-product of force and velocity converts these vector quantities into power (scalar), $P = \underline{F} \bullet \underline{v} = m\underline{a} \bullet \int \underline{a}\, dt$. Figure 6a shows a 20 ms segment of vibration power data with complex, nonlinear features. The corresponding statistical measures (Figs. 6b−6e) and traditional nonlinear measures (Figs. 6e−6g) do not provide a clear indication of the increasing severity of the seeded fault. Figure 7 shows that all four phase-space dissimilarity measures rise linearly with the increasing fault severity, thus yielding good change discrimination.

1.2 ADDITIONAL ANALYSIS OF EPRI MOTOR POWER DATA FOR THE BROKEN-ROTOR-BAR FAULT

A second EPRI test sequence began with the Allis Chalmers motor running in its nominal state (first dataset), followed by progressively more severe broken rotor bars. The second dataset involved a simulated failure that was one rotor bar cross section cut 50% in half at the 11 o'clock position. The third dataset was for the same rotor bar next cut through 100%. The fourth dataset was for a second rotor bar cut 100% at the 5 o'clock position, exactly 180° from, and in addition to, the first rotor failure. The fifth dataset was for two additional rotor bars cut adjacent to the original 11 o'clock bar, with one bar cut on each side of the original, yielding four bars completely open. Consequently, this sequence of seeded faults rises exponentially, as measured by the number of broken rotor bars (½ to 1 to 2 to 4). The EPRI report notes that the data-collection personnel noted a definite growling sound and a pulsating vibration during the last test (four broken rotors). We concatenated the five datasets into a single long dataset for ease of analysis, and converted the three-phase voltages and currents into instantaneous power, as described above.

We reiterate the PY2 analysis of this data, as motivation for the addition PY3 analysis. We split each of the five datasets into five subsets of 12,000 points each, giving 25 total subsets. The electrical power has a slow, low-amplitude variation with a period of roughly 0.1 s. As before, we removed this artifact, that otherwise confounds the interpretation of our results. A check of this artifact-filtered data revealed no data quality problems. We systematically varied the phase-space reconstruction parameters to obtain the most monotonic increase in condition change for the broken-rotor seeded-fault test sequence. Figure 8 shows that the phase-space dissimilarity measures rise by ten-fold over the test sequence. The exponential rise in the seeded-fault magnitude (doubling from 0.5 to 1.0 to 2.0 to 4.0) is mirrored in Fig. 8 by a linear rise in the logarithm of the dissimilarity measures.

We performed additional analysis of this seeded broken-rotor test during PY3. We focus on this analysis of vibration power only, based on the above results for the airgap test. As before, we reject the outboard acceleration due to the same data quality problem in the third component.

Figure 9a shows a 20 ms segment of vibration power data with complex, nonlinear features. The corresponding statistical measures (Figs. 9b−9e) and traditional nonlinear measures (Figs. 9e−9g) do not provide a clear indication of the exponentially-growing severity of the seeded fault. Figure 10 shows that all four phase-space dissimilarity measures rise linearly with the increasing fault severity, thus yielding good change discrimination.

1.3 ADDITIONAL ANALYSIS OF EPRI MOTOR POWER DATA: TURN-TO-TURN SHORTS

The EPRI data included a General Electric motor, with the following specifications.

Rated voltage:	4000	Bearing type:	sleeve
Rated HP:	500	Number of rotor bars:	84
Winding type:	form wound	Number of stator slots:	108
Phases:	3	Hertz:	60
RPM:	1185	Motor type:	induction
Insulation class:	B	Poles:	6
Enclosure:	open	Bar configuration:	copper rectangular

This test sequence began with the motor running in its nominal state (first dataset). The second dataset had a 2.70 ohm turn-to-turn short, via a large screw between two turns. The third dataset had a more severe, 1.35 ohm turn-to-turn, via a smaller screw between two turns. These three datasets were concatenated into a single long dataset for this analysis. The analysis sequence follows the increasing severity of the fault from the largest turn-to-turn resistance (infinite, corresponding to no short), to smaller (2.7 ohms), to smallest (1.35 ohms). We reiterate the PY2 analysis of this data, as motivation for the addition PY3 analysis. The three-phase voltages and currents were converted into instantaneous electrical power, as before. The three datasets were split into five subsets of 12,000 points each, giving 15 total subsets. This data has a low-amplitude, low-frequency artifact with a period of roughly 0.006 s. We remove this artifact, which would otherwise confound the analysis. The artifact-filtered power data has no data quality problems. Systematic variation of the phase-space reconstruction parameters revealed values that are most sensitive to the condition change for the turn-to-turn seeded-fault test sequence. Figure 11 shows that all four of the phase-space dissimilarity measures of electrical power rise linearly over the test sequence, mirroring the linear rise in the magnitude of the seeded faults (from 2.7 to 1.35 ohms).

We performed additional analysis of this turn-to-turn-short test during PY3, focusing on vibration power, based on the above results for the airgap test. The third component of outboard acceleration showed the same data quality problem as before, forcing its rejection. Figure 12a shows a 20 ms segment of vibration power data with complex, nonlinear features. The corresponding statistical measures (Figs. 12b−12e) and traditional nonlinear measures (Figs. 12e−12g) show some consistency with the increasing severity of the seeded fault. The minimum (P_N) rises and maximum (P_X) falls (Fig. 12b) monotonically over the test sequence. Kurtosis decreases and skewness increases monotonically (Fig. 12c) over the test sequence. Linear increases occur in the average number of time steps per cycle (Fig. 12d) over a very narrow range (7.2−7.6), and the first zero in the autocorrelation function (Fig. 12e). Figure 13 shows

that all four phase-space dissimilarity measures rise linearly with the increasing fault severity, thus yielding good change discrimination. We obtained the results in Sects. 1.1–1.3 by searching over the range of parameters for the best indication of condition change: $2 \le d \le 26$, $2 \le S \le 200$, and $1 \le \lambda \le 100$.

1.4 MOTOR DIAGNOSTICS TEST BED DATA FROM THE PENNSYLVANIA STATE UNIVERSITY

Appendix B is the statement of work for the subcontract to the Applied Research Laboratory at the Pennsylvania State University. Appendix C is the test plan for the Mechanical Diagnostics Test Bed (MDTB). This subsection describes details of the data acquisition, the nonlinear analysis, and results of the forewarning assessment for each of three MDTB accelerated failure test sequences. Previous work during FY2 of this NERI project determined that higher sampling rates for the data give superior failure forewarning, and that accelerometer data was more appropriate for the MDTB testing. Work during the second quarter of the present project year verified the adequacy of the data quality and sampling rate. Consequently, the tri-axial accelerometer data were sampled for each MDTB test sequence in ten-second snapshots at a sampling rate of 52 kHz. Data quality analysis revealed no problems with the MDTB data. The protocol for this test involves a break-in period at the nominal (1X) load (per the test plan in App. C) for one h, followed by twice (2X) the normal load until failure; our analysis uses the test data only during the overload period. Figure 14 shows the specific end-of-life failure for MDTB Run No. 36, including pinion damage, broken teeth, and a sheared shaft. PSU provided data snapshots at fifteen-min intervals. The failure occurred after 162.5 h, corresponding to 650 snapshots. Figure 15 shows the very complex, nonlinear features in the three components of the tri-axial accelerometer data ($\underline{a}$). The individual snapshots were combined into one long dataset (12.7 GB). Acceleration was subsequently converted to a long stream (4.1 GB) of vibration power (Fig. 16), using the previously described method to convert tri-axial acceleration into power via time-integration to velocity ($\underline{v} = \int \underline{a}\, dt$) with a subsequent vector dot-product to produce power ($P \sim \underline{a} \bullet \underline{v}$). We obtained the traditional nonlinear measures for each of ten 50,000-point cutsets from each snapshot of P; these cutset-based measures were then averaged over all ten cutsets of each snapshot and displayed for that snapshot (Fig. 17). Correlation dimension (top plot of Fig. 17) varies erratically between 2.9 and 3.1 before 65 h, then rises irregularly to 3.6 as a forewarning indication, and finally falls abruptly to < 2 as a failure indication. Kolmogorov entropy (middle plot of Fig. 17) varies irregularly between 0.025 and 0.045 prior to 65 hours, then rises erratically to > 0.07 as a forewarning of failure, and finally falls to < 0.01 as a failure indication. The first minimum in the mutual information function (bottom plot of Fig. 17) is constant at one time step, and then decreases abruptly to 0.1 at failure. The forewarnings are weak, because the variations are not inconsistent with the previous irregularities. The failure indications are unique and clear. The traditional nonlinear measures (TNM) vary erratically over small ranges of values, while the PSDM (below) show robust forewarning via variation over a much larger range of values.

Figure 18 shows the PSDM for PSU Run No. 36. The phase-space parameters are $S = 274$, $d = 2$, $\lambda = 1$, which are the same values that we used for the PY2 MDTB data to show consistency with that earlier analysis. All four measures of dissimilarity rise systematically (Figs. 18a−18d) to provide forewarning of the failure. However, a more robust and specific end-of-life (EOL)

indicator is needed. We observe that all four of the PSDMs have similar tends, suggesting the definition of a composite measure, C_i, as the sum of the four renormalized PSDMs for the i-th dataset (Fig. 18e):

$$C_i = U(\chi^2) + U(\chi_c^2) + U(L) + U(L_c). \quad (1)$$

This composite measure is more robust than any one of the PSDM, while accurately indicating condition change. The end-of-life indication from this composite measure is quantified as follows. We use contiguous, non-overlapping windows of C_i to obtain the best straight-line fit in a least-squares sense:

$$y_i = ai + b. \quad (2)$$

The window length of $m = 10$ values of C_i (and y_i below) is chosen consistent with the number of cutsets in each snapshot. Other values of m give inferior indication of condition change. Next, the variance, σ^2, measures the variability of the C_i values about this straight-line fit:

$$\sigma^2 = \Sigma_i (y_i - C_i)^2/(m\text{-}1). \quad (3)$$

Other fits (quadratic, cubic, and quartic) extrapolate poorly outside the fitting window. Finally, G measures the variability of next m values of C_i about an extrapolation of this straight-line:

$$G = \Sigma_i (y_i - C_i)^2/\sigma^2. \quad (4)$$

The index, i, in Eqs. (2)–(4) runs over the m values of C_i and y_i. Note that G has the form of a conventional chi-squared statistic, but we do not use that notation to avoid confusion with the two χ^2 PSDMs, $U(\chi^2)$ and $U(\chi_c^2)$. A statistical test for G would involve the null hypothesis that deviations from the straight-line fit are normally distributed. Standard chi-squared statistical tables give the corresponding value of $G \leq 28.5$ for $m = 10$ degrees of freedom with a probability of one out of the number (650) of extrapolations ($1/650 \sim 1.5 \times 10^{-3}$). However, we observe that many instances, for which $G > 28.5$ throughout this test sequence. These outliers occur because the underlying three-dimensional acceleration has dynamical correlations, thus violating the requirement for independent, identically distributed samples. Instead, we use G (solid curve in Fig. 18f) as a *relative* measure of end-of-life. We compare each value of G to the previous values to obtain a running maximum G_{max} (dashed curve in Fig. 18f), neglecting the first six G-values to avoid startup transients. This running maximum rises in modest increments to 376 over the first 159.75 h of the test, while intermediate values of G fall well below the running maximum. The chain curve (-.-) in Fig. 18f is the ratio, $R = (G_{max})_k/(G_{max})_{k-1}$, of the current maximum in G $(G_{max})_k$ to the previous maximum in G $(G_{max})_{k-1}$. G rises to 2,493 at 160 h, with a corresponding $R = 6.62$, that is substantially more than the largest non-end-of-life value, $R = 2.22$, at 2 h. Thus, G provides clear end-of-life forewarning, plus indication of the failure ($G = 244{,}655$).

The protocol for MDTB Run No. 37 involves a break-in period at the nominal 1X load (per the test plan in App. C) for 1 h, followed by 3X the normal load until failure; our analysis uses only the test data during the overload period. Figure 19 shows the specific end-of-life failure for MDTB Run No. 37, including pinion damage and broken teeth. PSU provided snapshots of

accelerometer data at 1 min intervals until the failure. The three components of acceleration as well as vibration power are not unlike Run No. 36, and are not shown. The individual snapshots were combined into one long dataset (10 GB), and subsequently converted to a long stream (3.5 GB) of vibration power, as described above. We obtained the traditional nonlinear measures for each of ten 50,000-point cutsets from each snapshot; these cutset-based measures were then averaged over all ten cutsets and displayed for each snapshot (Fig. 20). Correlation dimension (top plot of Fig. 20) decreases from 3.7 gradually but irregularly to 3.5 at 5.3 h. The next irregular decrease to 2.3 at 8 h is an early forewarning, while the more abrupt drop to <0.5 is an indication of failure onset. Kolmogorov entropy (middle plot of Fig. 20) likewise decreases erratically from 0.09 to 0.04 at 8 h. The abrupt drop to near zero after 8 h is an indication of failure onset. The first minimum in the mutual information function (bottom plot of Fig. 20) is constant at one time step over the entire test. Moreover, the TNM vary erratically over small ranges of values, while the PSDM (below) show robust forewarning via variation over a much larger range of values.

Figure 21 shows the PSDM for PSU Run No. 37. The phase-space parameters also are $S = 274$, $d = 2$, $\lambda = 1$, which are the same as those for the PY2 MDTB data to show consistency with the earlier analysis. All four measures of dissimilarity rise systematically (Figs. 21a−21d) to provide forewarning of the failure. As before, we use G as a *relative* measure of end-of-life, as shown in Fig. 21f. We compare each value of G to the previous values to obtain a running maximum G_{max} (dashed curve in Fig. 21f), neglecting the first five values to avoid startup transients. This running maximum rises in modest increments to 333 over the first 5 h of the test, while intermediate values of G fall well below the running maximum. The chain-dashed curve (-.-) in Fig. 21f shows the ratio, $R = (G_{max})_k/(G_{max})_{k-1}$, of the current maximum in G $(G_{max})_k$ to the previous maximum in G $(G_{max})_{k-1}$. G rises to 2,690 at 8.1 h, with a corresponding value of $R = 8.07$ that is much more than the largest non-end-of-life value at 0.5 h ($R = 1.79$). Thus, G provides clear end-of-life forewarning, as well as distinct indication of the failure itself ($G = 16{,}284$).

The protocol for this MDTB test involves a break-in period at the nominal 1X load (per the test plan in App. C) for 1 h, followed by 3X the normal load until failure; our analysis uses only the test data during the overload period. Figure 22 shows the specific end-of-life failure for MDTB Run No. 38, including broken/rounded off teeth on both the pinion and the gear. PSU provided snapshots at one-minute intervals until the failure. The three components of acceleration as well as vibration power are not unlike Run No. 36, and are not shown. The individual snapshots were combined into one long dataset (4.7 GB), and subsequently converted to a long stream (1.6 GB) of vibration power, as described above. We obtained the traditional nonlinear measures for each of ten 50,000-point cutsets from each snapshot; these cutset-based measures were then averaged over all ten cutsets and displayed for each snapshot (Fig. 23). Correlation dimension (top plot of Fig. 23) is roughly constant at 2.85 until 1.3 hours, and then rises slowly and irregularly to 3 at 2.5 h. Finally, correlation dimension decreases very irregularly to < 0.3 at 4 h, as a failure indication. Kolmogorov entropy (middle plot of Fig. 23) likewise is roughly constant (but very erratic) at 0.02 until 2 h, and then rises irregularly to a peak of 0.04 at 2.7 h. Kolmogorov entropy then decreases erratically to near zero at 4 hours, as a clear failure indication. The first minimum (M_1) in the mutual information function (bottom plot of Fig. 23) is constant at one time step until 4 h, and then falls abruptly to a 0.1 at 4 h, as a failure indication. The TNM vary

erratically over small ranges of values, while the PSDM (below) show robust forewarning via variation over a much larger range of values.

Figure 24 shows the PSDM for PSU Run No. 38. The phase-space parameters again are $S = 274$, $d = 2$, $\lambda = 1$, which are the same as those for the PY2 MDTB data to show consistency with the earlier analysis. All four measures of dissimilarity rise systematically (Figs. 24a−24d) to provide forewarning of the failure. As before, we use G as a *relative* measure of end-of-life, as shown in Fig. 24f. We compare each value of G to the previous values to obtain a running maximum G_{max} (dashed curve in Fig. 24f), neglecting the first five values to avoid startup transients. This running maximum rises in modest increments to 374 over the first 2.6 h of the test, while intermediate values of G fall well below the running maximum. The chain-dashed curve (-.-) in Fig. 24f shows the ratio, $R = (G_{max})_k/(G_{max})_{k-1}$, of the current maximum in G, $(G_{max})_k$, to the previous maximum in G, $(G_{max})_{k-1}$. G rises to 13,486 at 3.77 h, with a corresponding $R = 11.71$, which is substantially more than the largest non-end-of-life value at 0.6 h ($R = 6.20$). Thus, G provides end-of-life forewarning, as well as indication of the failure ($G = 48{,}379$).

Run No. 39 involves a somewhat different test protocol with a one-hour break-in period at the nominal load 1X, followed by twice the normal load (2X) for 2 h, after which the load alternated between three times normal load 3X and 2X loads for 10 and 5 min, respectively. This experiment seeks failure forewarning in the presence of load changes. Figure 25 shows the failure state, including broken and rounded teeth on both the gear and pinion. Since the conventional statistical measures and traditional nonlinear measures previously provided no consistent failure forewarning, we show only the PSDM for PSU Run No. 39 in Figs. 26−27. The sawtooth features in each of the six subplots correspond to the transition between 2X and 3X loading with the straight-line portion in Fig. 26 corresponding to the 3X segment in Fig. 27, and inversely. The phase-space parameters again are $S = 274$, $d = 2$, $\lambda = 1$, which are the same as those for the PY2 MDTB data to show consistency with the earlier analysis. Figure 26 shows the PSDM results only for the 2X-portion of the experiment. All four PSDM rise systematically (Figs. 26a−26d) to provide forewarning of the failure, with a corresponding systematic rise in the composite measure, C_i. As before, we use G as a *relative* measure of end-of-life, as shown in Fig. 26f. We compare each value of G to the previous values to obtain a running maximum G_{max} (dashed curve in Fig. 26f), neglecting the first six values to avoid startup transients. This running maximum rises in modest increments to $G_{max} = 853$ over the first 3.68 h of the test, with a corresponding non-end-of-life value for $R = (G_{max})_k/(G_{max})_{k-1} = 3.89$, as shown by the chain-dashed curve in Fig. 26f. Subsequently, G rises to 5,231 at 8.43 h, with a corresponding $R = 3.89$. Thus, G provides end-of-life forewarning, but no indication of the failure onset ($G_{ONSET} = 5{,}231$), because the failure for this test is driven by the 3X loading. We analyze the 3X portion of MDTB Run No. 39 separately, as shown in Fig. 27. All four PSDM rise systematically (Figs. 27a−27d) to provide forewarning of the failure, with a corresponding systematic rise in the composite measure, C_i. We again use G as a *relative* measure of end-of-life, as shown in Fig. 27f, comparing each value of G to the previous values to obtain a running maximum G_{max} (dashed curve in Fig. 27f), neglecting the first six values to avoid startup transients. This running maximum rises in modest increments to $G_{max} = 1{,}151$ over the first 7.92 h of the test, with a corresponding non-end-of-life value for $R = (G_{max})_k/(G_{max})_{k-1} = 2.88$, as shown by the chain-dashed curve in Fig. 27f. Subsequently, G rises to 33,415 at 8.35 h, with a corresponding

R = 29.03. Thus, G provides end-of-life forewarning, as well as indication of the failure onset (G = 44,552) at 8.55 h.

The results for PSU Runs No. 36−39 are summarized in Table 2, which gives: (a) the largest non-EOL value of R (R_{NEOL}) and the corresponding value of G (G_{NEOL}); (b) values of R (R_{EOL}) and G (G_{EOL}) that indicate the end of life, and the matching time (T_{EOL}/T_{FAIL}); (c) the value of G at failure onset (G_{ONSET}) and the corresponding time (T_{ONSET}/T_{FAIL}); and (d) the failure-endpoint time (T_{FAIL}). Runs No. 36−38 have largest non-EOL values: R_{NEOL} = 6.20 and G_{NEOL} = 376. The smallest EOL values are: R_{EOL} = 6.62 and G_{EOL} = 2,493. Thus, limits (for example) of R > 6.4 and G > 1,800 provide EOL forewarning. Moreover, we find that the largest EOL value of G_{EOL} = 13,486, while the smallest failure-onset value is G_{ONSET} = 16,284. Thus, an intermediate value (for example) of G > 15,000 distinguishes the EOL from failure onset forewarning. This approach gives quantitative limits for transitions from nominal operation (green-light for "go" in a traffic signal metaphor), to forewarning of failure (yellow light for "caution"), and finally to failure onset (red-light for "stop").

We consider the results of MDTB Run No. 39 separately, because this experiment involves a different test protocol. Table 2 shows that the above limits for G and R also distinguish between the non-EOL (green) and EOL (yellow) states for the 3X portion of this test, because the higher overload drives the failure. These limits do not apply to the 2X test, due to the reduced damage at the lower overload. Unsurprisingly, a different limit of G > 38,000 (for example) distinguishes between the EOL and failure onset forewarnings, due to the change in test protocol. The green-yellow-red approach still applies for MDTB Run No. 39. Ignoring the Run No. 39 2X results, we find $T_{EOL}/T_{FAIL} \geq 0.938$ and $T_{ONSET}/T_{FAIL} \geq 0.990$.

Table 2. Summary of MDTB Test Results

Run	Over-load	$\Delta\tau$ min.	R_{NEOL}	G_{NEOL}	R_{EOL}	G_{EOL}	$\frac{T_{EOL}}{T_{FAIL}}$	G_{ONSET}	$\frac{T_{ONSET}}{T_{FAIL}}$	T_{FAIL} hr.
36	2X	15	2.22	376	6.62	2,493	0.985	244,655	0.998	162.50
37	3X	1	1.79	333	8.07	2,690	0.956	16,284	0.996	8.55
38	3X	1	6.20	374	11.71	13,486	0.938	48,379	0.990	4.02
39	2X	1	2.32	853	3.89	5,231	0.980	5,231	0.980	8.60
39	3X	1	2.88	1,151	29.03	33,415	0.972	44,552	0.994	8.60

1.5 SHAFT-CRACK SEEDED-FAULT DATA FROM THE PENNSYLVANIA STATE UNIVERSITY

ORNL received tri-axial accelerometer data from PSU for Run No. 17 of the Shaft-Crack test (see App. D for the test plan). The data sampling rate of the tri-axial acceleration is 128 kHz for each 10-s snapshot. Our analysis of the corresponding vibration power revealed inadequate quality for two reasons. First, the signal range for baseline data is between -18.9 and 15.5. This range drops abruptly for the first shaft notch (-10.9 to 8.6), then increases abruptly for the second shaft notch (-24.9 to 24.2), and rises still further for the third shaft notch (-32.5 to 28.0). The fourth through ninth shaft notches have roughly a consistent range between ±20. This unusual range variability in the first four datasets implies a problem with initial signal calibration or

scaling. A second data quality problem is that the first minimum (M_1) in the mutual information function is one time step, corresponding to under-sampling of the data. The value of M_1 should be four or more time steps for adequately sampled data. These quality problems prohibit further useful analysis of the acceleration data. PSU also supplied time-serial angle data from a toothed wheel (see App. D for details). ORNL analysis of this data revealed two additional quality problems. First, the width of the solid teeth and intervening gaps was not the same over the circumference. Second, the rotation speed was 23 Hz, corresponding to roughly 0.06 ms (16.6 kHz) between samples of the angular motion for each of the 360 teeth. However, the angular motion varied much faster than 16 kHz, resulting in under-sampling of the angular dynamics. These quality problems prohibit further useful analysis of the time-serial angle data.

ORNL received additional tri-axial accelerometer data from PSU for Run No. 18 of the seeded-fault Shaft-Crack test, also according to the test plan of App. D. The data were provided at two sampling rates: 128 kHz and 196 kHz. We analyzed the 196 kHz data with 1,000,000 data points (5.1 s) for each of ten snapshots, due to the data under-sampling problem with Run No. 17, as discussed above. The first minimum (M_1) in the mutual information function of the vibration power is constant at two time steps, which is substantially less than four time steps, indicating that this data also is under sampled at 196 kHz. This quality problem prohibits further useful analysis of the data.

ORNL received data for Run No. 19 of the Shaft-Craft test at 196 kHz sampling rate, with improvements in the experimental hardware to eliminate grounding loops that introduced high-frequency noise. Quality analysis of this data revealed that the sampling rate was adequate, as was the data precision (12−14 bits). However, the range of signal variation was markedly different between the baseline and the subsequent test cases. Moreover, the distribution function for the number of signal occurrences vs signal value is also very different between the baseline (abrupt rise to a peak at small signal values, followed by a gradual decrease at high values) and subsequent test cases (rise to central sinusoidal peak than roughly symmetry decrease). This difference arises because the waveforms are very different between the baseline (sharp positive spikes) and test cases (complex, nonlinear oscillations). Documentation for this test showed that the old tri-axial acceleration sensor was used for the baseline data, while the new acquisition hardware (three separate acceleration sensors) was used for the subsequent test cases. This change in sensors produced the confounding differences between the baseline and subsequent test cases. PSU later provided a new set of baseline data that is consistent with the other datasets, allowing further analysis. As before, data from the individual tests were concatenated into one long dataset (234 MB) for ease of analysis. Figure 28 shows a resultant segment of vibration power (Fig. 28a), along with conventional statistical measures (Figs. 28b−28e), and traditional nonlinear measures (Fig. 28e–28g). The magnitudes of minimum and maximum in vibration power (Fig. 28b) and constant, then rise abruptly for the last test. The number of time steps per cycle (Fig. 28d) rises slowly and monotonically, showing a large increase for the largest cut depth. None of the other measures in Fig. 28 show a consistent change over this test sequence. Figure 29 shows that all four PSDM rise monotonically by one-hundred-fold as the cut depth increases from zero (baseline) to 3/8 in. These strong indications of change are in sharp contrast to the weak ones of Fig. 28.

1.6 GENERATOR SEEDED-FAULT DATA FROM THE PENNSYLVANIA STATE UNIVERSITY

We analyzed additional PSU data with operator-imposed turn-to-turn shorts in the rotor of a motor-driven, three-phase electrical generator. The generator is a Kato Engineering, Model A267890000, (5 kW, 3-phase, 60 Hz, synchronous alternating current). The drive motor is a Kato Engineering, Model D267880000 (7.5 HP, synchronous, brushless, direct current). The sequence test states were: (a) nominal operation, (b) short across five rotor turns, (b) short across ten rotor turns, (c) short across twenty-five rotor turns, (d) short across fifty rotor turns, and (e) short across one hundred rotor turns, out of five hundred turns in one of four poles. The tri-axial accelerometer data were sampled at 102.4 kHz, concatenated into one long dataset for analysis, and converted to vibration power, as described above. The data are acquired under different resistive loads, corresponding to four different output powers: 0, 1.2kW, 2.4kW, and 3.6 kW. Figure 30a shows 5.9 ms of vibration power data at the zero load, displaying complex, nonlinear features. Conventional statistics and traditional nonlinear measures (Fig. 30b−30g) do not indicate the rising seeded-fault severity. Plots for other load levels are not unlike Fig. 30, and are not shown. Further analysis is beyond the scope of this present work.

1.7 COLLABORATION WITH ORNL'S HIGH FLUX ISOTOPE REACTOR (HFIR)

Lee Hively met with HFIR staff (Steve Burnette, Dave Davenport, Eric Griffis, and Mark Matthews) on January 17, 2003 to initiate collaboration. These discussions identified nuclear-grade equipment for condition monitoring. Specifically, the hot-off-gas fan No. 6 (HOG6) has a long and continuing failure history; this fan is belt-driven by a 10HP three-phase electric motor. Present predictive maintenance approaches at HFIR include vibration analysis (displacement, velocity, and acceleration), thermography, lubrication oil analysis, and motor current signature analysis. Acquisition of accelerometer data is covered by the present HFIR configuration control, and presently is by a hand-held instrument (Computational Sciences Inc., Knoxville, Tennessee) that samples 1024 points over 100 ms. This data is insufficient in both the sampling frequency and the total number of data points. Consequently, improved data acquisition is required, for which Hively committed $10K under this NERI project for the HFIR effort. Changes to the HFIR configuration control are necessary to acquire motor current and voltage data, which therefore may not be available for this project. Hively met with HFIR instrumentation and controls staff (Ken Hardin, Randy Welch, and Karl Zimmerman) on February 10, 2003 to outline the data acquisition needs for tri-axial accelerometer data from HOG6. Hively provided a personal computer, monitor, data acquisition board, isolation block, and associated LabView™ software to HFIR staff (Ron Miller and Sam Henley) on February 11, 2003. The data acquisition hardware and software were acquired under this project during PY2. Hively also provided a written description of the data acquisition needs to the appropriate supervisor (Karl Zimmerman) on February 11, 2003. The computer and software have been set up and are functional. However, two HFIR outages delayed the procurement of the sensors, final setup, and acquisition of operational data beyond the end of this project.

1.8 TASK 3.1 – ILLUSTRATION OF COST-BENEFIT FOR PROGNOSTICATION

A general and unambiguous cost-benefit evaluation of machinery health assessment technologies has remained an elusive goal of engineering planning. Indeed, an exhaustive cost-benefit evaluation would involve a complex risk assessment with fuzzy parameters, probabilities, confidence levels, and information gaps. Such an evaluation was attempted under the NERI program to track the cost of various machinery condition and maintenance scenarios for optimal scheduling.[1] Development of a systematic cost-benefit approach is beyond the scope of this project. Instead, we consider several scenarios that reflect actual plant problems to illustrate the benefits of timely failure forewarning via nonlinear analysis. This anecdotal approach provides insight into the cost benefits, while avoiding the issue of precise costs that are usually questionable at best.

Two of the most important factors for nuclear power plant (NPP) equipment failures are the risk of forced outage time and the cost of make-up power. Table 3 shows the ranking of the industry experience with system failures in terms of forced outage time.[2] The cost of make-up power is quite variable, as seen in the estimated costs of Fig. 31 (ref. 3). Thus, correct timing of maintenance is extremely important in determining and eventually minimizing the cost of outage make-up power.

The following examples are representative of the actual failure-forewarning equipment tests that were performed under this NERI project. We selected four pieces of equipment for cost-benefit analysis, as summarized in Table 4, based on the failure rates in Table 3 and the availability of cost information. We take the cost of replacement electrical power at $0.7M per 24-h/day.[1] This value assumes a 1300 MW plant at $22/Mwh, and should be adjusted for plant size.

The first example involves a turbine generator, which is responsible for a 16% of forced outages, as shown in Table 3. Our analysis assumes: (a) timely shutdown, (b) the outage time is the same for a forced-failure outage as for a planned outage, and (c) the maintenance/repair costs are the same in both cases. We consider only the replacement power cost, following the analysis of an earlier NERI project, “Smart Equipment in NPP.” For details, see the work by Campbell, et al, “Virtual Machine Equipment Simulation [Task 3.1 (ref. 2)].” This example postulates a forewarning on June 10, 2002 that a turbine failure would occur within 1 to 2 weeks. We analyze two cases. The first case allows the turbine to fail with a trip. The second case schedules turbine maintenance within a day of the forewarning. We further assume that the time-to-repair distribution for this second case is the same as the run-to-failure case. Cost calculations assume a 1300 MW plant. The average wholesale price for electricity, provided by Reliadigm, a subsidiary of Public Service Company of New Mexico for 2002 (Fig. 31), ranges from less than $20/Mwh to about $130/Mwh. Consequently, the timing of a plant outage may have a dramatic effect on the cost of lost generation. Figure 32 shows that the mean run-to-failure cost is $6.7M vs $2.9M when maintenance is scheduled immediately, based on the failure forewarning indication.

As a result of the greater wholesale electricity cost for the next few days after the forewarning, the cost rises with the increasing delay in maintenance time. If the forewarning occurs when the cost of electricity was projected to decline, a delay in the maintenance would be cost-effective, subject to the expected timing of the failure. Thus, ongoing condition assessment of the turbine-

generator system with a one-week forewarning window would result in substantial savings when projected make-up power costs are integrated with machinery health information in the maintenance decision process.

Table 3. Lost Availability Ranking of U.S. PWR Plant Systems/Components (1990-1995)

Rank	System/Component	Outage Time (Hours)	Percent of Outage	Number of Failures	MTTR (Hours)
1	Transformer	14,442.20	10.64	39	370.3
2	Main Generator	10,955.30	8.07	70	156.5
3	Turbine	10,654.10	7.85	115	92.6
4	Steam Generator	10,597.60	7.81	46	230.4
5	Reactor Coolant Pump	10,004.10	7.37	47	212.9
6	Service Water System	6,369.50	4.69	6	1061.6
7	Steam Extraction Piping	6,362.80	4.69	4	1590.7
8	Diesel Generator	5,828.10	4.29	12	485.7
9	Control Rod System	4,194.60	3.09	51	82.2
10	Main Feedwater Valve	4,147.40	3.06	60	69.1
11	Pressurizer	4,073.40	3	20	203.7
12	Safety Injection System	3,899.40	2.87	8	487.4
13	Reactor Coolant System	3,327.40	2.45	22	151.2
14	Main Steam Valve	3,319.70	2.45	33	100.6
15	Circuit Breaker	3,067.10	2.26	14	219.1
16	Steam Generator Feedpump	2,854.50	2.1	18	158.6
17	Auxiliary Feedwater Pump	2,776.40	2.05	4	694.1
18	Moisture Separator Reheater	2,413.60	1.78	19	127
19	Inverter	2,399.80	1.77	12	200
20	Condenser	2,185.10	1.61	19	115
21	Main Feedwater Pump	1,983.50	1.46	37	53.6
22	Main Steam System	1,225.80	0.9	15	81.7
23	Relay	1,183.70	0.87	12	98.6
24	Intake Valve	1,142.20	0.84	2	571.1
25	Circulating Water	955.4	0.7	8	119.4

Table 4. Sample Equipment Used in the Cost Benefit Analysis

Component(s)	Item Number in Table 3	Reasons for Selection
Turbine/Generator	2 & 3	Total of 16% of forced outage time is associated with these components. Failure results in full unit outage.
Centrifugal Charging Pump	NA	Although not specifically listed in Table 3, failure is considered to be a thorn in the side of utility maintenance personnel, and results in LCOs that are "black marks" against the utility.
Steam Generator Feedpump	16 & 21	Total of 2.5% of outage time. These pumps are the heart of the secondary system.
Reactor Coolant Pump	5	Failure results in 8 % of forced outage time. In addition, the issue of RCP shaft cracking has become very important.

The second example involves a centrifugal charging pump. Usually, plants have redundant pump components. Most Westinghouse pressurized water reactors (PWRs) have three pumps: one normal charging pump and two emergency charging pumps; see Figs. 33−34 for typical pump layouts. (Note that many plants originally had one of these pumps as a positive displacement pump, which now has been replaced in almost all plants by an additional centrifugal charging pump.) The abnormal operation or loss of one pump is considered to be a safety condition, and the subject pump must be reported to the NRC as "inoperable." The NRC may opt to issue a Limited Condition of Operation (LCO), requiring that restorative maintenance must be performed within 72 (normal) to 90 h (extended). If the equipment restoration cannot be completed within this time window, the unit must be shut down. Typical component failures in these pumps involve the motor, bearings, gears, and shaft cracking. Many experts believe that much of this damage may be accumulated during the mandated quarterly in-service testing (IST), since the flow conditions during those tests are more extreme than the normal design conditions. Consequently, most utilities maintain a spare pump on site, due to high pump-failure rates. However, pump replacement may require more time than the LCO allows, resulting in a unit shutdown.

Forewarning may allow maintenance during LCO, thus avoiding a unit outage or derating in some cases. We assume in this example that forewarning of a bearing failure allows a simple repair during the LCO. The total repair cost would be about $14,000: $4500 for parts; $9720 for labor (3 person crew, 90 work-hours per person); and no derating or unit trip. The second case involves running the bearing to failure, which would require a pump replacement. We estimate 114 h for the repair and declaration of inoperative status in this second case with the unit off-line

for 24 h (unit shutdown after the 90-h LCO), plus an equivalent of 12 h for unit startup. The pump replacement would cost $200,000, plus 36 h of lost electrical generation cost, for a total cost of $1.25M. The saving would be over $1.2M.

Under the current regulatory environment, knowledge of the specific condition of the centrifugal charging pump may be less than beneficial. Specifically, failure forewarning with a long remaining life would require that the pump must immediately be declared inoperative, and an LCO requested. A corresponding change in the regulatory environment is needed to accept that condition assessment of safety-related equipment is good, allowing the utility to ensure that the equipment is in the best possible operating state. Moreover, proper interpretation of such information may allow the reduction of redundancy, rather than the present heavy reliance on redundancy, because equipment health is unknown. Additionally, continuous machinery health monitoring may allow elimination of pump IST, thus reducing the damaging affects of non-nominal flow. IST could be performed only when the remaining useful life of the pump is deemed to be short enough to indicate the need for rotation to the stand-by pump.

The third example involves a steam generator feedpump/turbine. A unit trip is the typical result of the unexpected loss of a Steam Generator Feedpump (SGFP) in a PWR, or a Reactor Feedpump (RFP) in a boiling water reactor (BWR), with subsequent operation at reduced power. This pump is on the secondary side, but is the very heart of power production. When one pump is out of service, the unit cannot operate above approximately 70% power. For instance, the loss of a SGFP due to turbine shaft cracking occurred at Plant Vogtle (Southern Nuclear) in the mid-90's. The result was a unit trip, and the usual 3−4 days to get back on line. Subsequently, the unit operated at approximately 70% power for approximately one week during turbine repair. The resulting makeup power cost was approximately $3.5M.

When bearing overload is detected, the unit is derated to 70% and pump realignment is performed. If the fault is not detected, damage may progress to bearing failure, rotating element failure, or catastrophic failure of the entire pump. Consequently, we analyze four scenarios (from top to bottom in Table 5) as follows: (a) correction of bearing overload after failure forewarning via nonlinear analysis; (b) repair of failed bearing; (c) repair of failed rotating assembly; and (d) replacement of failed pump. Table 5 shows that the resulting cost savings are between $2.2M and $4.2M.

Table 5. Steam Generator Feedpump Cost Savings

Workers	Crew Hours	Work Hours	Labor Cost per Hour	Labor Cost	Parts Cost	Unit Outage	Unit Derate Hours	Unit Derated to percent	Cost of Replacement Power	Total Cost	Savings
3	24	72	36	$ 2,592	$ -	0	36	0.7	$ 315,000	$ 317,592	
3	30	90	36	$ 3,240	$ 4,500	72	48	0.7	$ 2,520,000	$2,527,740	$ 2,210,148
4	36	144	36	$ 5,184	$ 50,000	72	144	0.7	$ 3,360,000	$3,415,184	$ 3,097,592
4	62	248	37	$ 9,176	$ 200,000	72	250	0.7	$ 4,287,500	$4,496,676	$ 4,179,084

The fourth example involves a reactor coolant pump (RCP), that is a vital part of the power production cycle. Although not a safety-related component, its continued operation is essential to unit function. We consider the failure of an actual pump at the Tennessee Valley Sequoyah plant in early September of 2000 (six months after a refueling outage). A RCP on Unit 1 was brought down for balancing after exceeding the administrative limit for vibration of 10 mils peak-to-peak. The vibration increased on each successive balance test, subsequently exceeding the 15-mil alarm limit at 17 mils (peak to peak), and approaching the 20-mil required shutdown limit. Inspection revealed a crack encompassing 252 degrees circumferentially (Figs. 35−36).[4] The lack of a spare pump shaft resulted in a 40-day outage.

This scenario assumes forewarning of the crack fault allowed a spare pump shaft to be ordered and completion of the maintenance during the scheduled outage 6 months earlier. If the cost per day for make-up power is $0.7M (ref. 1), and the maintenance cost is the same whether it had been done during the scheduled or unscheduled outage, the resulting savings would be $28M.

We summarize the results of this cost-benefit analysis as follows. Timely forewarning and accurate diagnosis of just one NPP failure is sufficient to justify extensive monitoring of vital and safety related systems. Table 6 shows a summary of the scenarios used in evaluating the cost benefit. In each case, actual failures have occurred on the in-plant equipment. Typical cost savings range from $1M to $28M, depending on the specific equipment and failure scenario. While the precise cost savings vary with the underlying assumptions, the conclusion is that failure forewarning will allow millions of dollars in cost savings for each NPP unit, as well as important improvements to safety.

1.9 TASK 3.2 – COMMERCIALIZATION ROADMAP AND FUTURE WORK

The final component of this task is a roadmap to a commercial product from the current state-of-the-art. The present technology has the attributes, as shown on the left-hand side of Table 7. The highly desirable features of a commercial product are on the right-hand side of Table 7. Much work remains to bridge the wide gulf between today's retrospective analysis of archival data on a desktop computer to a future stand-alone commercial device for prospective analysis of real-time data on a portable computing platform.

Current technology will enable some improvements almost immediately, as shown by the center column in Table 7. Implementation of this approach on a portable computer platform (e.g., laptop) is possible now, because the typical size of the forewarning analysis is < 28 MB. Moreover, PSDM analysis is faster on a 2 GHz Pentium-4™ desktop computer than the wall-clock time to acquire the corresponding archival data. Modern laptop and digital-signal processor speeds are ≥ 3 GHz and have ≥ 64 MB of memory, so speed and memory are not a limitation for portability. The research-class FORTRAN software has been developed and used on a variety of different computers and operating systems over the past nine years: IBM RISC/6000 under IBM's version of UNIX, DEC-alpha under DEC's version of UNIX, Intel-PII under Windows NT and Windows 2000, and AMD-Athlon™ and Intel Pentium-4™

Table 6. Summary of Cost-Benefit Scenarios

System/Component	Demonstration Scenario	Source of Savings	Approx. Cost Savings (Per Event)	Environmental Cleanup	Applicable Monitored Components							
					800 HP Electric Motor	500 HP Electric Motor	1/4 HP Electric Motor	Gearbox	Turbine/Rotor Blade	Shaft	Electric Generator	Bearings
Turbine-Generator	Unit outage required for repair/maintenance. Outage time and maintenance cost assumed to be essentially uneffectied by choice of maintenance interval.	Cost difference based on difference in projected make-up power costs only.	$3.8 Million	PWR: Minimal (non-radioactive) BWR: Potentially major					X	X	X	X
Centrifugal Charging Pump	Maintenance resulting from failure will result in exceeding normal 72-90 hour LCO, therefore requiring unit shutdown.	Preventative maintenance based on machinery health monitoring may be accomplished during LCO window, thus eliminating unit outage.	$1.2 Million	Potentially major	X*	X*		X		X		X
Steam Generator Feed Pump	Thermal misalignment results in bearing failure, unit trip, then operation at approximately 70% power during repair. Bearing health monitoring allows repair during low-cost makeup power cost time, and avoids the unit trip.	Preventative maintenance based on machinery health monitoring averts unit trip, shortens repair	$2.2 Million	PWR: Minimal (non-radioactive) BWR: Potentially major				X	X	X		X
Steam Generator Feed Pump	Thermal misalignment results in rotating assembly failure (shaft or blade), unit trip, then operation at approximately 70% power during repair. Bearing health monitoring allows repair during scheduled outage, and avoids the unit trip.	Preventative maintenance based on machinery health monitoring is performed during scheduled outage, averts unit trip, shortens repair	$3.1 Million	PWR: Minimal (non-radioactive) BWR: Potentially major				X	X	X		X
Steam Generator Feed Pump	Thermal misalignment results in complete pump failure, unit trip, then operation at approximately 70% power during repair. Bearing health monitoring allows repair during scheduled outage, and avoids the unit trip.	Preventative maintenance based on machinery health monitoring is performed during scheduled outage, averts unit trip, shortens repair	$4.5 Million	PWR: Minimal (non-radioactive) BWR: Potentially major				X	X	X		X
Reactor Coolant Pump	Failure results in unit trip, followed by extended unscheduled 40 day outage.	With timely indication of crack in shaft, maintenance for pump shaft replacement, could be accomplished during refeuling outage, thus avoiding forced outage.	$28 Million	Potentially major	X**					X		X

* 600 HP Motor

** 5246 HP Motor

under Windows2000™ and Windows-XP™. The software required little (and usually no) change to move from one computer and/or operating system to the next. Thus, we anticipate no problems with implementation on a portable computer. Further improvements in speed and the memory requirement are possible by reducing unnecessary arrays and subroutines. In addition, real-time data acquisition is now available commercially: sensors, data acquisition software, data transfer, storage, and analysis. With the previous two improvements, prospective analysis is likewise possible in the near-term via software improvements and upgrades to analyze (near-) real-time data, including a user-friendly graphical user interface for interaction with the machine operator. Other aspects of the technology will require much more development, as discussed next.

Table 7. Summary of Improvements for Commercialization

Current state-of-the art for PSDM Forewarning	Bridge	Ideal for commercial forewarning device
(a) analyst-intensive	≤ 3 years	(a') analyst-independent
(b) retrospective analysis of	now	(b') prospective analysis of
(c) archival data via	now	(c') (near) real-time data via
(d) desktop computer to give	now	(d') portable computer to give
(e) binary forewarning that is	≤ 3 years	(e') the remaining time to failure that is
(f) machine- and fault-specific, after which the	> 3 years	(f') independent of specific machine or fault
(g) failure occurs in an uncontrolled fashion	> 3 years	(g') allowing failure avoidance or control
(h) at high cost of laboratory resources	≥ 5 years	(h') at reasonable cost
(i) depending on laboratory infrastructure	> 5 years	(i') reliably/independently for years

A first-generation commercial device will need one additional and vital feature: analyst-independence. The specific tasks develop this computational infrastructure involve: (1) choosing suitable process-indicative data, (2) checking the data quality and providing feedback to correct any quality problems, (3) identifying and removing artifacts in the data, and (4) determining the best forewarning parameters for PSDM analysis. We anticipate the algorithmic advancements will include: implementation of a robust, multi-channel phase-space analysis; improved filtering to remove signal artifacts with wide variations in time scale; and improved measures of forewarning that robustly indicate the increasing severity deterioration. A three-year effort will be needed to accomplish these tasks.

Longer-term effort is necessary for other desirable features of a commercial prognostication device. For example, determination of the remaining-time-to-failure requires substantial advancement of the data-driven, model-independent, nonlinear statistical paradigm for prognostication over a range of operational loads and usage scenarios, including appropriate

confidence intervals and/or error bounds. Development of forewarning that is independent of the specific machine or fault will require extensive tests to demonstrate the prognostics on many types of surrogate equipment and representative faults, because critical operating equipment is unavailable for testing. Moreover, generic forewarning requires an answer to the question, "What qualitative and quantitative changes in condition does phase-space dissimilarity measure?" The answer to this question probably will require an extensive library of test data across many different faults and machines, from which generic features are identified for specific faults and used for prognostication across a variety of machinery. Such data should also show forewarning consistency across multiple failures for the same fault and machine. Other desirable features are: global-positioning for mobile equipment; spread-spectrum wireless data transmission to minimize noise; and integrated computer-chip implementation with sensors and battery power. Finally, a commercial device must function reliably and independently in adverse environments for a long time at a reasonable cost.

2. ADDITIONAL WORK

Hively and Protopopescu prepared the third annual (and final) NERI2000-109 project presentation, including the results as of the middle of May 2003. At the request of the Department Of Energy (DOE) NE-20 program manager, Lisa Herrera, the principal investigator (Hively) traveled to Rockville, Maryland and gave the presentation. Based on the presentation and quarterly reports to date, our DOE Project Manager (Dr. Madeline Feltus) summarized the results of this NERI2000-109 work as "outrageously successful." During the three-day review meeting, Hively also served as a peer reviewer for other NERI project presentations under the category of advanced instrumentation and controls.

Hively diagnosed premature termination of long FORTRAN computational analyses as arising from numerous reads from very long data files. Hively constructed a test code that demonstrated the failure after 4.3×10^9 data points. The FORTRAN vendor (Compaq Visual FORTRAN) provided an alternative compilation approach (release configuration) that eliminated the problem and also increased the computational speed by two- to four-fold (depending on the application) by avoiding numerous internal diagnostic checks. The problem arose from overflow of a 32-bit unsigned-integer diagnostic counter in the default compilation mode (debug configuration) after 2^{32} ($= 4.3 \times 10^9$) advances.

Hively and Protopopescu are collaborating on development of analytic models that show chaos in individual variables (channels), but that also display very regular behavior when two (or more) of the channels are combined. This work demonstrates under well controlled and characterized conditions that very complex, chaotic processes can produce simple behavior that is very counter-intuitive but necessary for complex systems (such as robots or the human brain) to operate smoothly (e.g., continuous arm motion). This work also has been funded by the companion DOE/Basic Energy Sciences (BES) project under ORNL's Center for Engineering Science and Research (CESAR).

Vladimir Protopopescu gave a presentation, "Predictability and Control Issues in Complex Dynamical Systems," to the DOE/NSF/SIAM Workshop on Predictability of Complex Phenomena in Santa Fe on December 17, 2002. The co-authors on the paper were J. Barhen, Y. Braiman, and L. M. Hively. This work was funded by a companion CESAR project.

The DOE/NE-20 program office requested a full fiscal year's summary of the FY02 work in a prescribed three-page format. ORNL revised our earlier submission (described in the Q1/PY3 quarterly report) and sent it via e-mail to Marty Martinez on October 22, 2002. Martinez confirmed receipt of our submission in a return e-mail on October 23, 2002. A second revision was received from Martinez in PDF format. ORNL responded to Martinez with revisions on December 17, 2002. The final PY2 summary for this NERI2000-109 project was included in the DOE/NE-20 NERI 2002 Annual Report.

Hively and Protopopescu prepared and submitted an extended abstract, "Forewarning of Machine Failure via Nonlinear Analysis," to the San Diego meeting (June 1−5, 2003) of the

American Nuclear Society (ANS). This paper was presented by Protopopescu and summarizes work under this NERI project.

Hively presented a paper, "Detection of Changing Dynamics in Physiological Time Series," to the ANS meeting in Gatlinburg, Tennessee (April 8, 2003). This paper (and a companion proceeding paper with Protopopescu) describes forewarning of biomedical events: epileptic seizures from brain wave data, cardiac fibrillations from heart wave data, breathing difficulty from lung sounds, and sepsis onset in experimental rats from ECG data. This work has been funded by the ORNL Laboratory-Directed Research and Development (LDRD) program, a funds-in Cooperative Research and Development Agreement (CRADA), DOE/BES, DOE/Office of Emergency Management (OEM), and DOE/Office of Science (OS) under the Laboratory Technology Research Program. The paper also was published in the meeting proceedings. Hively gave another invited presentation, "Forewarning of Biomedical Events," to medical staff at Cincinnati Children's Hospital Medical Center (Cincinnati, Ohio) on December 20, 2002. Subsequent discussions with the physicians identified potential areas for collaboration on new proposals, focusing in forewarning of epileptic seizures in children via nonlinear analysis of scalp EEG.

The ORNL nonlinear technology has substantial intellectual property protection in the form of six U.S. Patents and two patents pending; see App. F. Two of these six patents were obtained during this NERI project. Both of the patents pending (items 1 and 4 of App. F) were submitted to the U.S. Patent Office to protect ideas that arose from work under this NERI project. No licensing agreements presently exist for use of these patents. Appendix G lists the technical publications and oral presentations of this NERI work. Appendix H lists recent technical publications and conference papers for related projects in forewarning of biomedical event and structural failures.

A graphical user interface (GUI) will facilitate practical use of this forewarning technology. Hively mentored an undergraduate student (Talisha Haywood) during the summer of 2003 to implement such a GUI. The user-friendly features include visualization of results and intuitively-obvious use with no user training. The implementation can work on many different computer platforms that run various operating systems. Remote use of the GUI is possible via the Internet using an appropriate server. The summer work included development of the functional requirements, software design, implementation using MatLab™, and testing for typical data. The work was funded by DOE's Research Alliance for Minorities (RAM) program. Hively verified that the same MATLAB procedure files yield the same results for the same data files on his own WindowsXP™ PC. See App. I for further details.

2.1 PERFORMANCE

The objective of this project is development of failure prognostication and extensive testing to provide compelling evidence that the forewarning technology is accurate and robust. This report provides a detailed description of the prognostication methodology, which is protected by six U.S. Patents and two patents pending (App. F). This report also presents results of extensive tests, showing that the same methodology provides robust and timely failure forewarning for a variety of equipment. One previous NERI[5] project showed failure forewarning for a single pump-lube system. Another previous NERI project[6] provided different scaling relationships for

each machine failure. In contrast to these very limited demonstrations, this project provides a single, general, robust approach for failure prognostication for several machines and different kinds of failure.

The project was completed on time and within budget. Total project spending (Fig. 37) through the fourth quarter of the third project year is $1,117,000 ($157K in PY1, $481K in PY2, and $479K in PY3). This project accomplished all of the original objectives, as follows: development of the prognostication capability, acquisition of the test data for a variety of equipment (by subcontractors at the Applied Research Laboratory of the Pennsylvania State University and at Duke Engineering and Services), demonstration of failure forewarning on those seeded-fault and accelerated-failure test sequences, cost-benefit analysis, and roadmap for commercialization of the technology. The work developed a novel approach to machine failure forewarning; two patent applications were submitted during the project to the U.S. Patent Office to protect this intellectual property. The project is complete, as summarized in Table 8 and as documented in detail by this final report.

2.2 ISSUES/CONCERNS

The PY2 subcontract with DE&S was set in place on 14 January 2002. Later that same week, DE&S informed the ORNL principal investigator (Lee Hively) of several project management concerns. First, DE&S had previous commitments that required their staff to work on weekends and evenings under this subcontract. Second, DE&S committed their data acquisition equipment to a different project for the first three weeks of February in California. Third, the combination of the previous two items required work by DE&S during the last week of February to meet the Task 1 delivery date. Fourth, DE&S informed the ORNL principal investigator on Monday February 25, 2002 that they had exceeded the Task 1 budget ($15K) by $2K. The DE&S request for additional funds to cover the $2K overage was declined. Both of the deliverables were complete by the Task 1 deadline of 1 March 2002 (two test sequences and characterization of those sequences). Fifth, a quality check of new DE&S data revealed that the data-sampling rate was too low, so no further analysis of their data was appropriate. These concerns mean that DE&S lost control of staff time, equipment resources, schedule, cost for the subcontract, and quality of the deliverables. Consequently, the principal investigator decided not to continue the subcontract beyond Task 1, which was ORNL's only commitment to DE&S under PY2 subcontract.

In light of the continuing delays by DE&S during the first quarter of the second project year, ORNL initiated a subcontract with the Applied Research Laboratory at the Pennsylvania State University to acquire test sequence data. The ORNL principal investigator (Lee Hively) obtained the concurrence of Dr. Madeline Feltus (DOE/NE-20) on 9 January 2002, before proceeding with this second subcontract, which was set in place on 12 February 2002. Deliverables from PSU were received by ORNL in a timely fashion and were of high quality. No further programmatic difficulties were encountered during this project. These issues did not impact cost performance or project schedule.

Table 8. Status Summary of NERI Tasks for First, Second, and Third Project Years

Milestone/task description	Planned Completion Date	Actual Completion Date
Task 1.1: ORNL set subcontract in place for DE&S	09/00	10/00
Subcontractor provide preliminary test data to ORNL	09/00	02/01
Subcontractor construct test plan for accelerated testing	11/00	04/01
Subcontractor provide datasets to ORNL	01/01	06/01
Task 1.2: ORNL analyze quality of DE&S test data	02/01	06/01
Subcontractor replace any inadequate data	02/01	06/01
Task 1.3: ORNL perform condition change analysis on data	08/01	08/01
Task 1.4: ORNL construct library of condition change signatures	08/01	08/01
Task 1.5: ORNL correlate condition change to failure	08/01	08/01
Task 1.6: ORNL procure new computer	08/01	05/01
ORNL implement nonlinear analysis on new PC	08/01	06/01
Task 2.1: Subcontractor provide test-sequence data	03/02, 06/03	06/02
Task 2.2: ORNL evaluate prognostication of nonlinear paradigm	08/02, 09/03	09/02
Task 2.3: ORNL improve nonlinear paradigm as appropriate	08/02, 09/03	09/02
Task 2.4: ORNL develop algorithm for change recognition	08/02, 09/03	09/02
Task 3.1: Collaborators assess benefits of prognostication	09/03	09/03
Task 3.2: Collaborators map potential commercialization	09/03	09/03

REFERENCES

1. M. W. Golay and C. W. Kang, "On-Line Monitoring for Improved Nuclear Power Plant Availability and Operational Advice -Active Equipment Monitoring: Rotating Machinery," pp. 12−13, MIT-ANP-TR-057, Vol. I, Massachusetts Institute of Technology, February 1998.

2. James E. Campbell and Bruce M. Thompson, Sandia National Laboratories, "Virtual Machine Equipment Simulation (Task 3.1)," Nuclear Energy Research Initiative (NERI), "Smart" Equipment and Systems to Improve Reliability and Safety in Future Nuclear Power Plant Operations, September 2001.

3. NERI Smart-NPP, Year 3 Annual Report, December 2002.

4. Phil Hitchcock, presentation at the *EPRI NMAC Pump Users Group Meeting*, Charlotte, NC, August 2001.

5. F. A. Durán, et al., "Smart Equipment and Systems to Improve Reliability and Safety in Nuclear Power Plant Operations," NERI99-306 Project Summary (August 1999 – December 2002) in "Nuclear Energy Initiative – 2002 Annual Report," DOE/NE-0122 (pp. 73−75).

6. L. Bond, "On-line, Intelligent, Self-Diagnostic Monitoring for Next Generation Nuclear Power Plants," NERI99-168 Project Summary (September 1999 – January 2003) in "Nuclear Energy Initiative – 2002 Annual Report," DOE/NE-0122 (pp. 53−56).

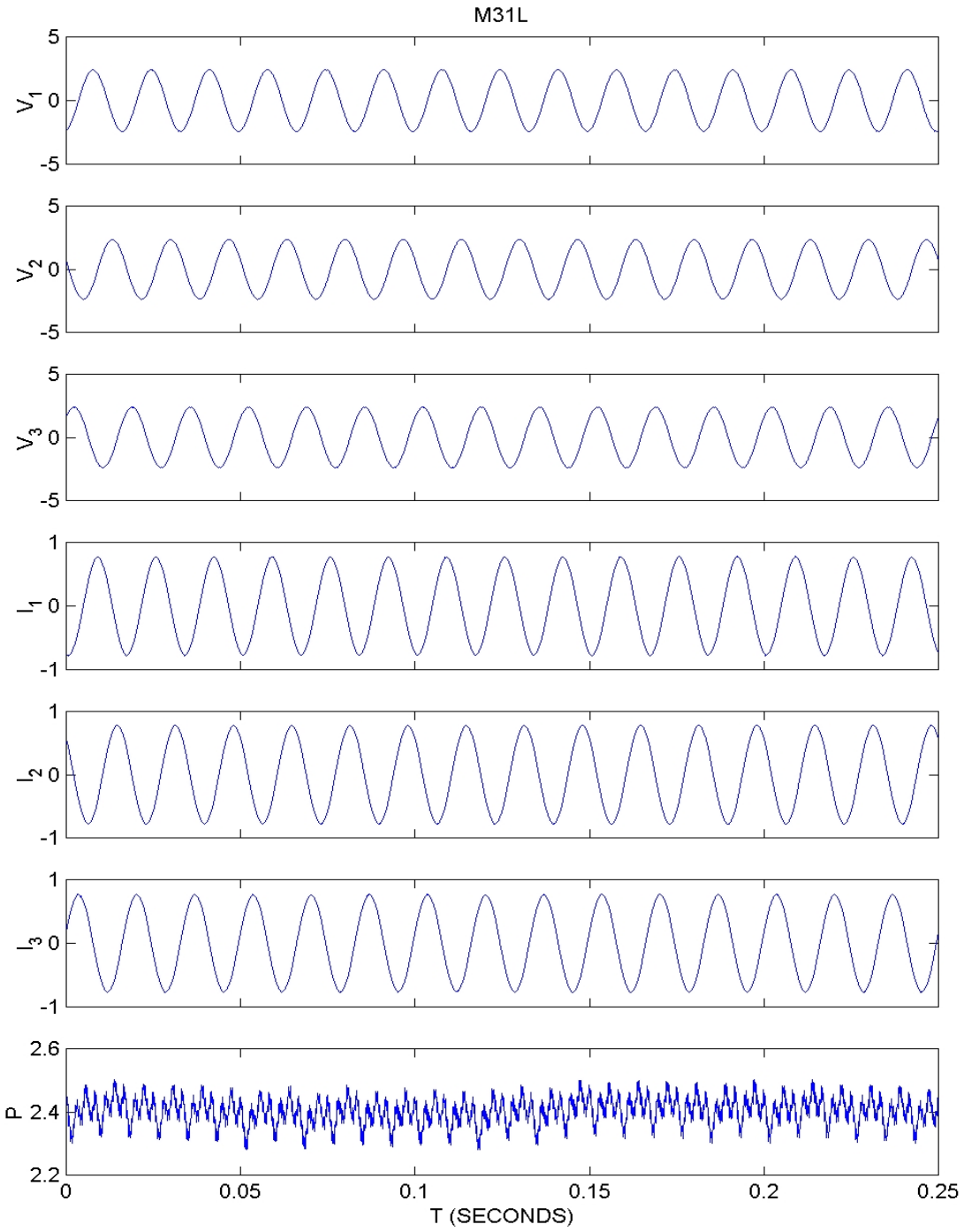

Fig. 1. Typical baseline EPRI data vs time from the Allis Chalmers motor. Top three plots show the three-phase voltages (V_i). Middle three plots show the three-phase currents (I_i). The sinusoidal variation in these plots corresponds to 60 Hz. The bottom plot shows instantaneous power, P, as the sum of the products of the three-phase currents times the corresponding voltages.

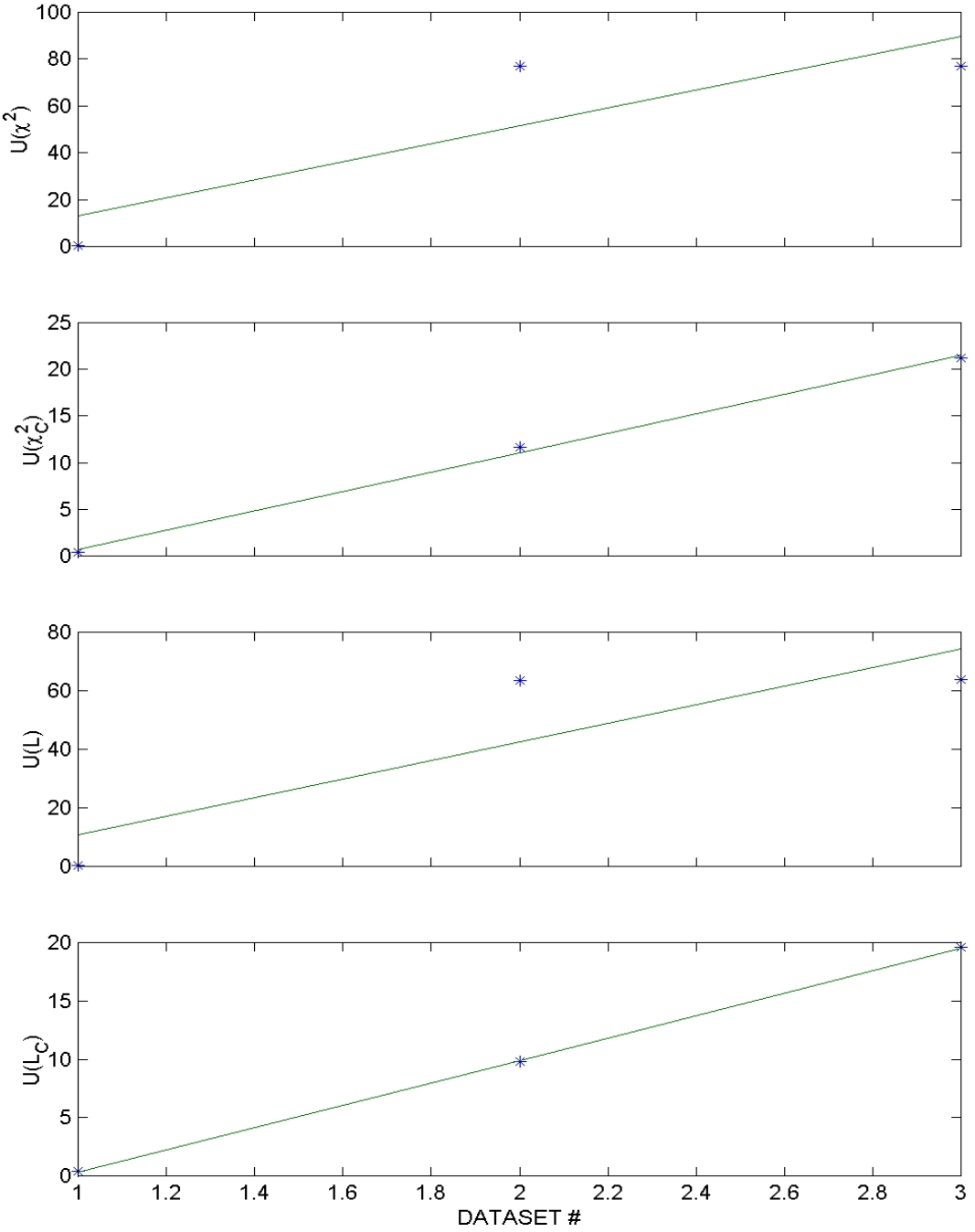

Fig. 2. Plots of the four nonlinear dissimilarity measures dataset vs analysis of the airgap-offset seeded-fault electrical power data, with the following parameters: $d = 3$, $S = 56$, $w = 573$, $\lambda = 88$, $N = 12000$, $B = 5$. Dataset No. 1 is for the nominal (no fault) state. Datasets No(s). 2−3 are for two different airgap-offset faults. Stars (*) show the dissimilarity values with the straight linear added as an aid for interpretation of the graphs.

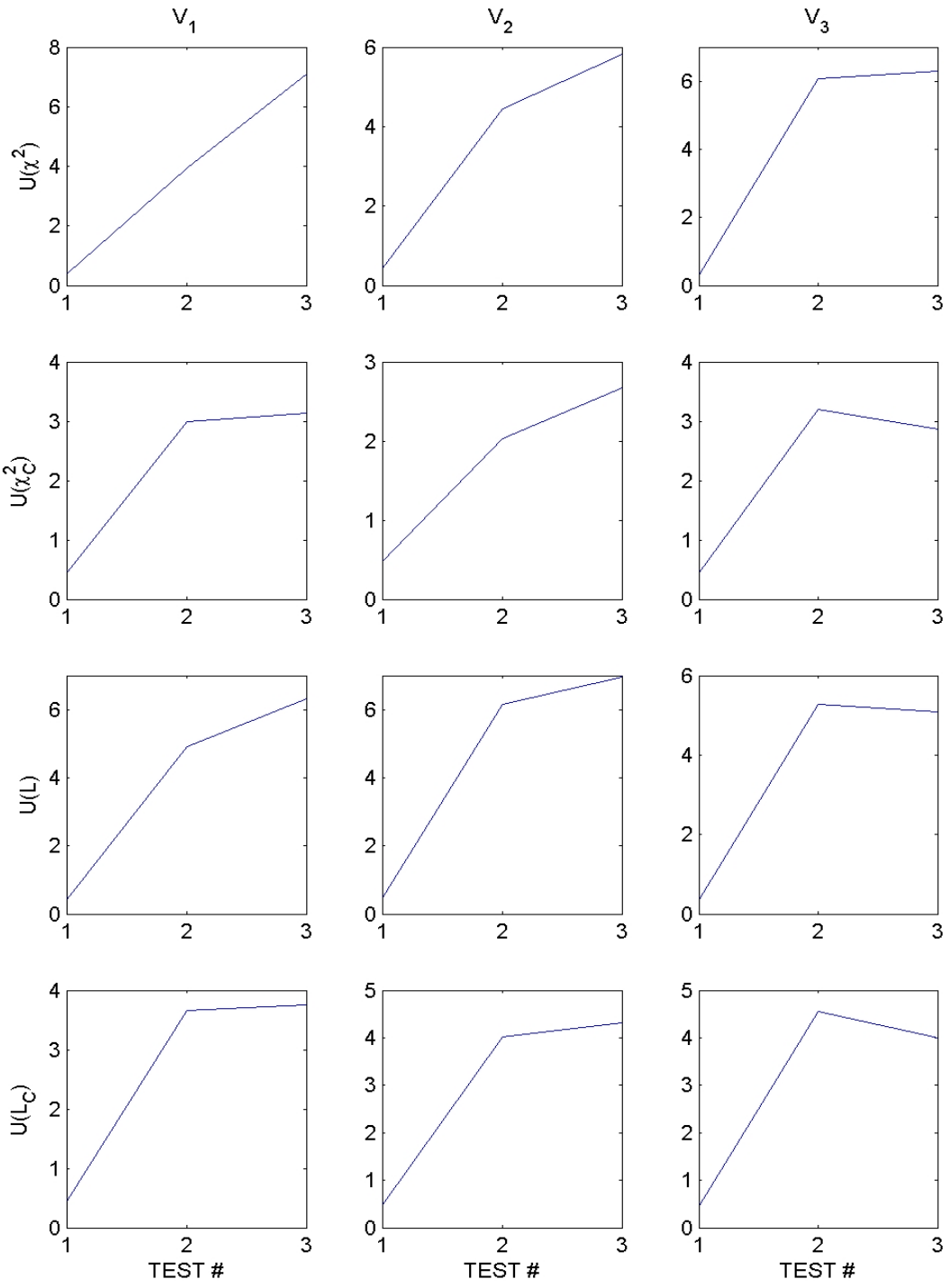

Fig. 3. Phase-space dissimilarity measures for the airgap-offset seeded-fault. Columns correspond to individual three-phase voltages, with the same parameters as Fig. 2. Dataset No. 1 is for the nominal (no fault) state. Datasets No.(s) 2−3 are for two different airgap-offset faults.

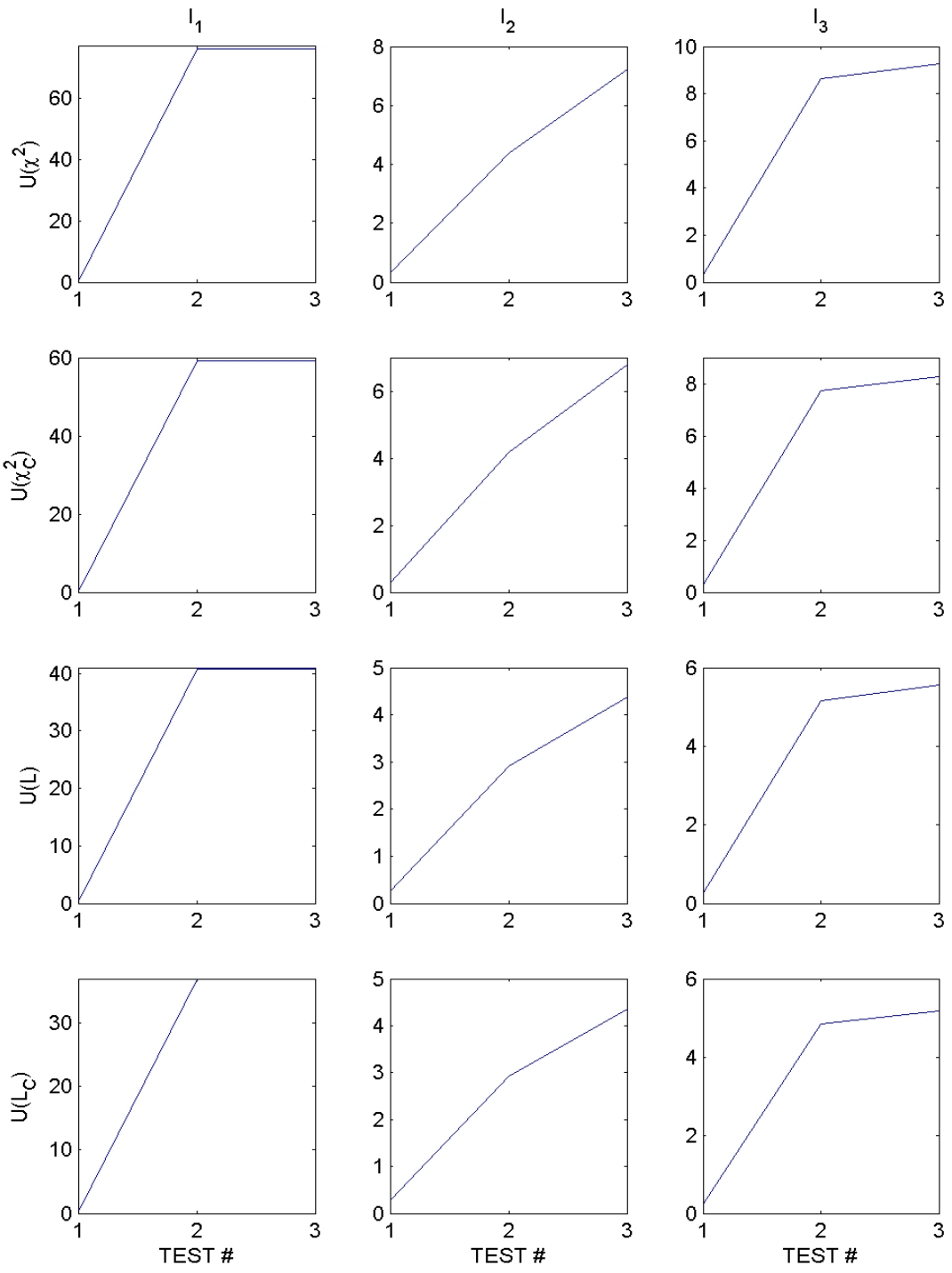

Fig. 4. Phase-space dissimilarity measures for the airgap-offset seeded-fault. Colums correspond to individual three-phase currents, with the same parameters as Fig. 2. Dataset No. 1 is for the nominal (no fault) state. Datasets No.(s) 2−3 are for two different airgap-offset faults.

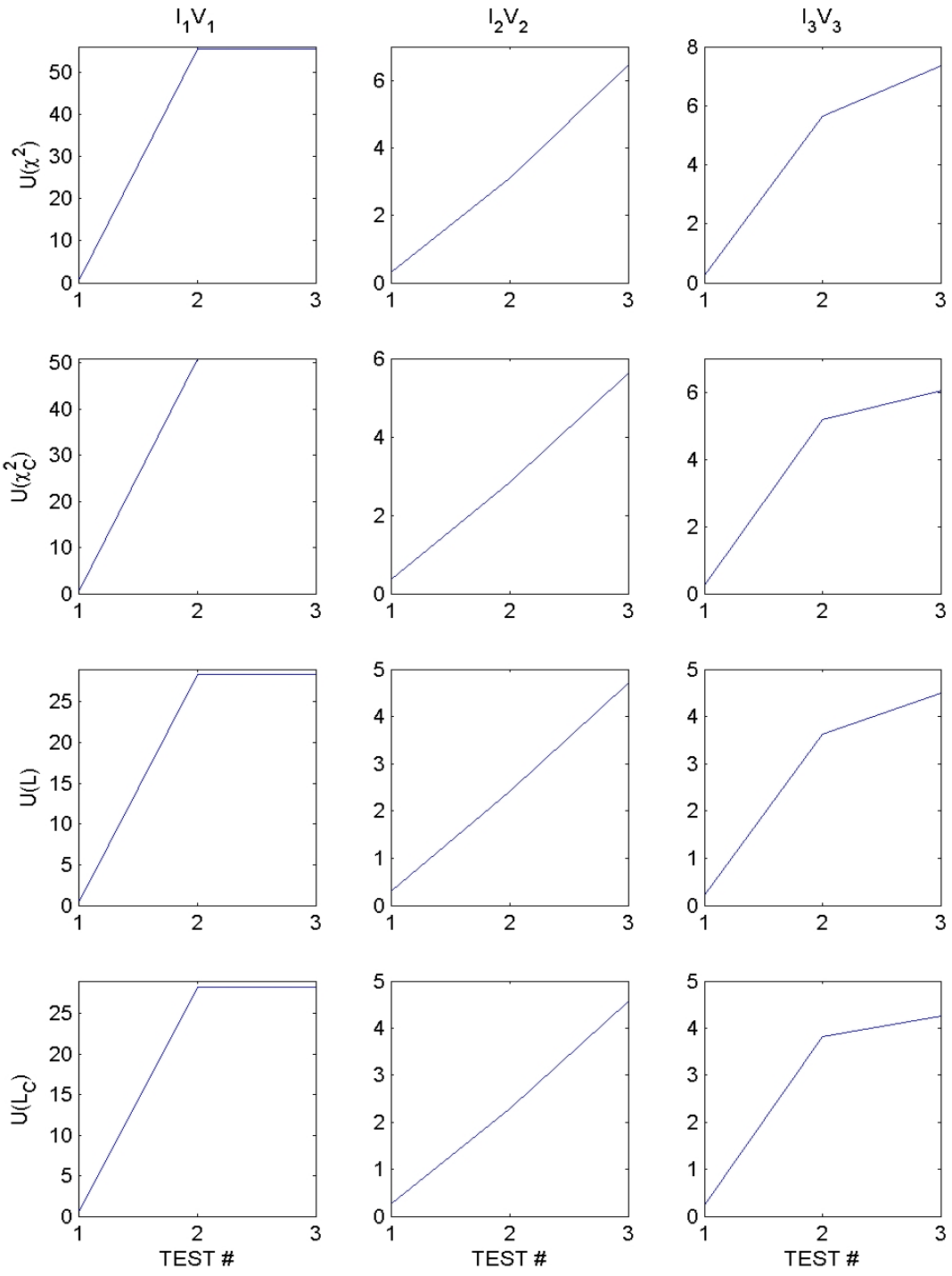

Fig. 5. Phase-space dissimilarity measures for the airgap-offset seeded-fault. Columns correspond to each component of three-phase power, I_iV_i, with the same parameters as Fig. 2. Dataset No. 1 is for the nominal (no fault) state. Datasets No.(s) 2−3 are for two different airgap-offset faults.

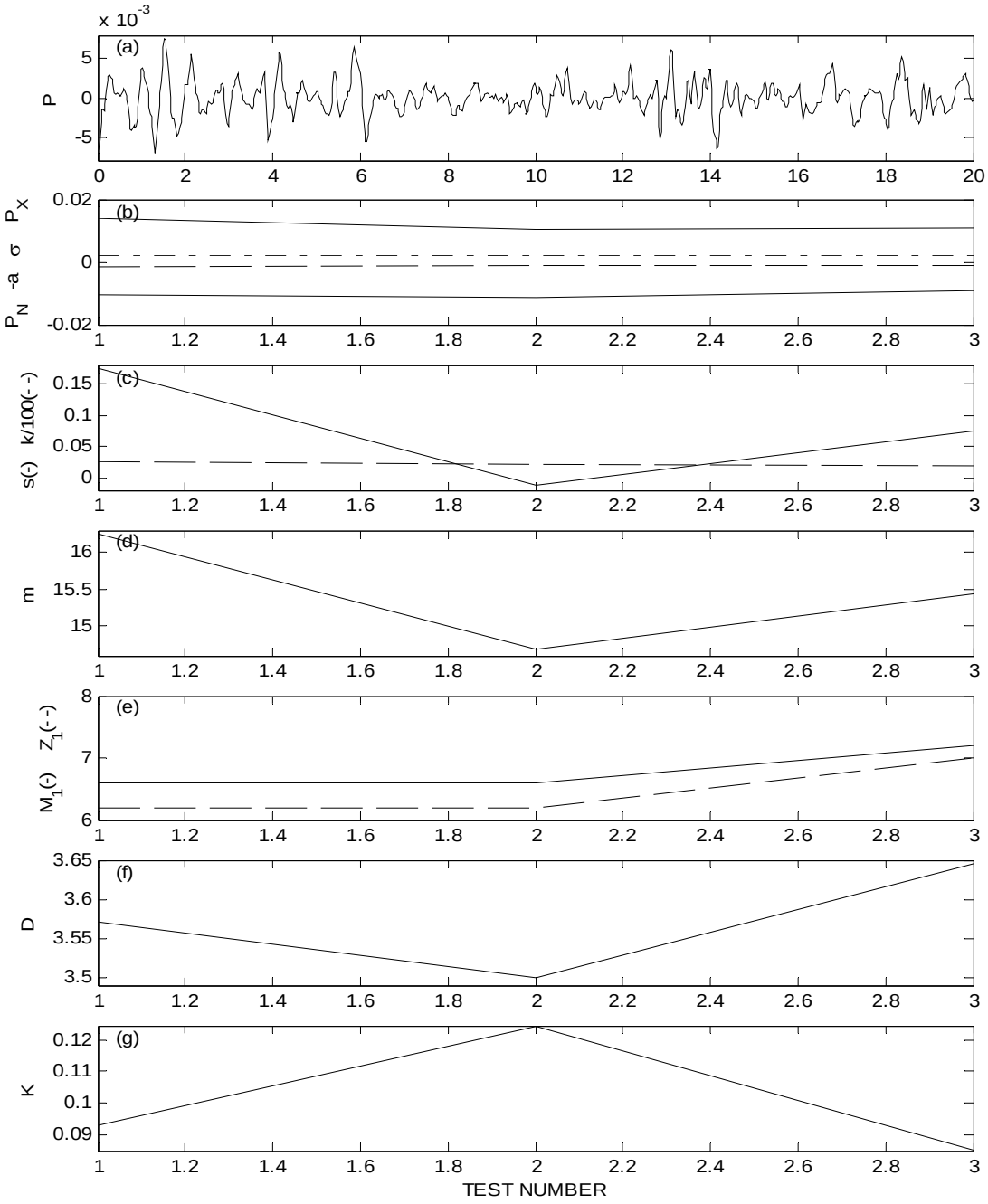

Fig. 6. Results for EPRI air-gap seeded fault from vibration power -- (a) Vibration power vs time (ms); (b) minimum (P_N), absolute average deviation (a), standard deviation (σ), and maximum (P_X) in vibration power vs test number; (c) skewness (s) and kurtosis (k) versus test number; (d) average number of time steps per cycle (m) vs test number; (e) first zero in the autocorrelation (Z_1) and first minimum in the mutual information function (M_1) vs test number; (f) correlation dimension (D) vs test number; and (g) Kolmogorov entropy (K) vs test number.

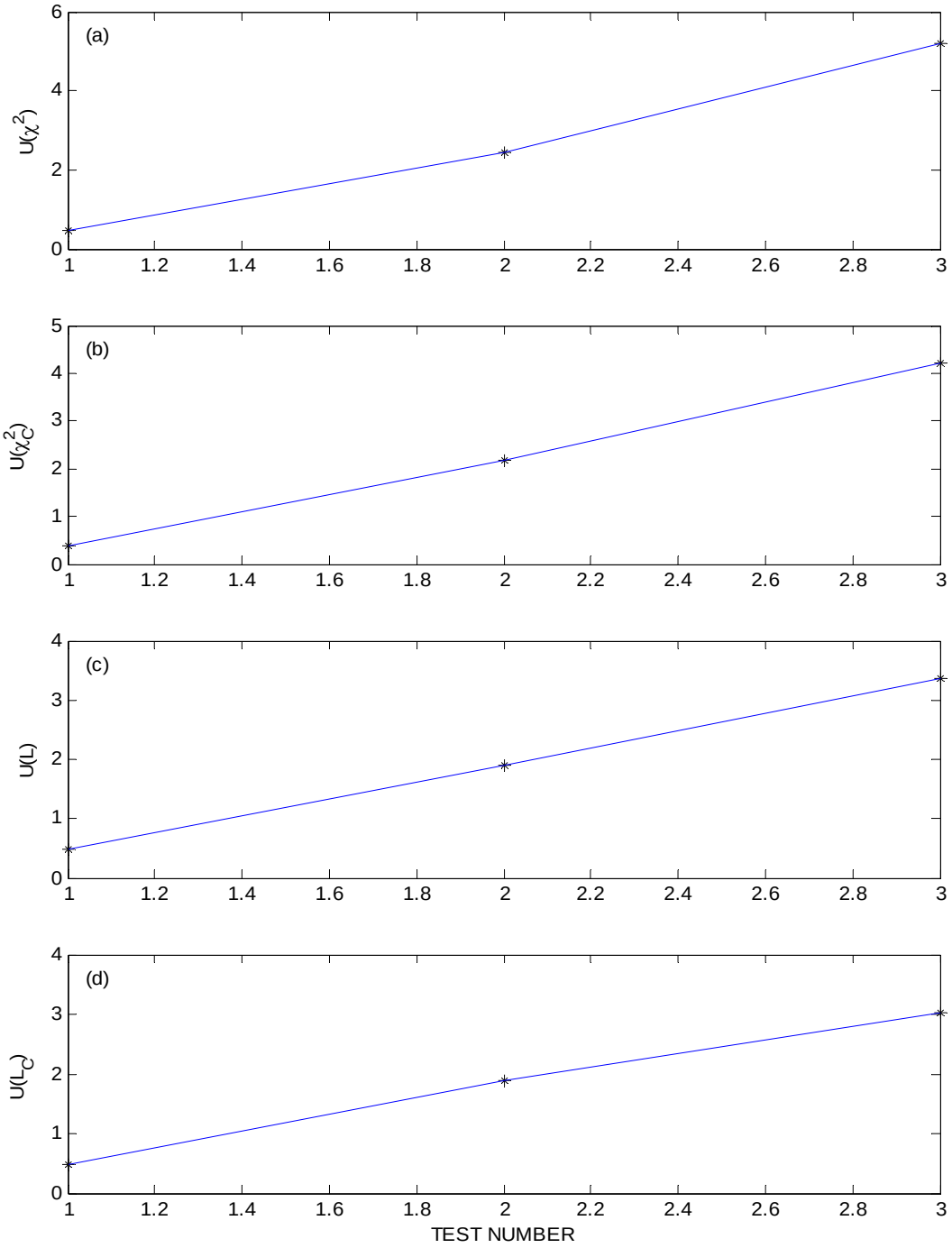

Fig. 7. Plots of the four nonlinear dissimilarity measures for the airgap-offset seeded-fault. The data are vibration power, with the following parameters: $d = 3$, $S = 3$, $\lambda = 11$, $N = 12000$, $B = 5$. Dataset No. 1 is for the nominal (no fault) state. Datasets No.(s) 2−3 are for two different airgap-offset faults.

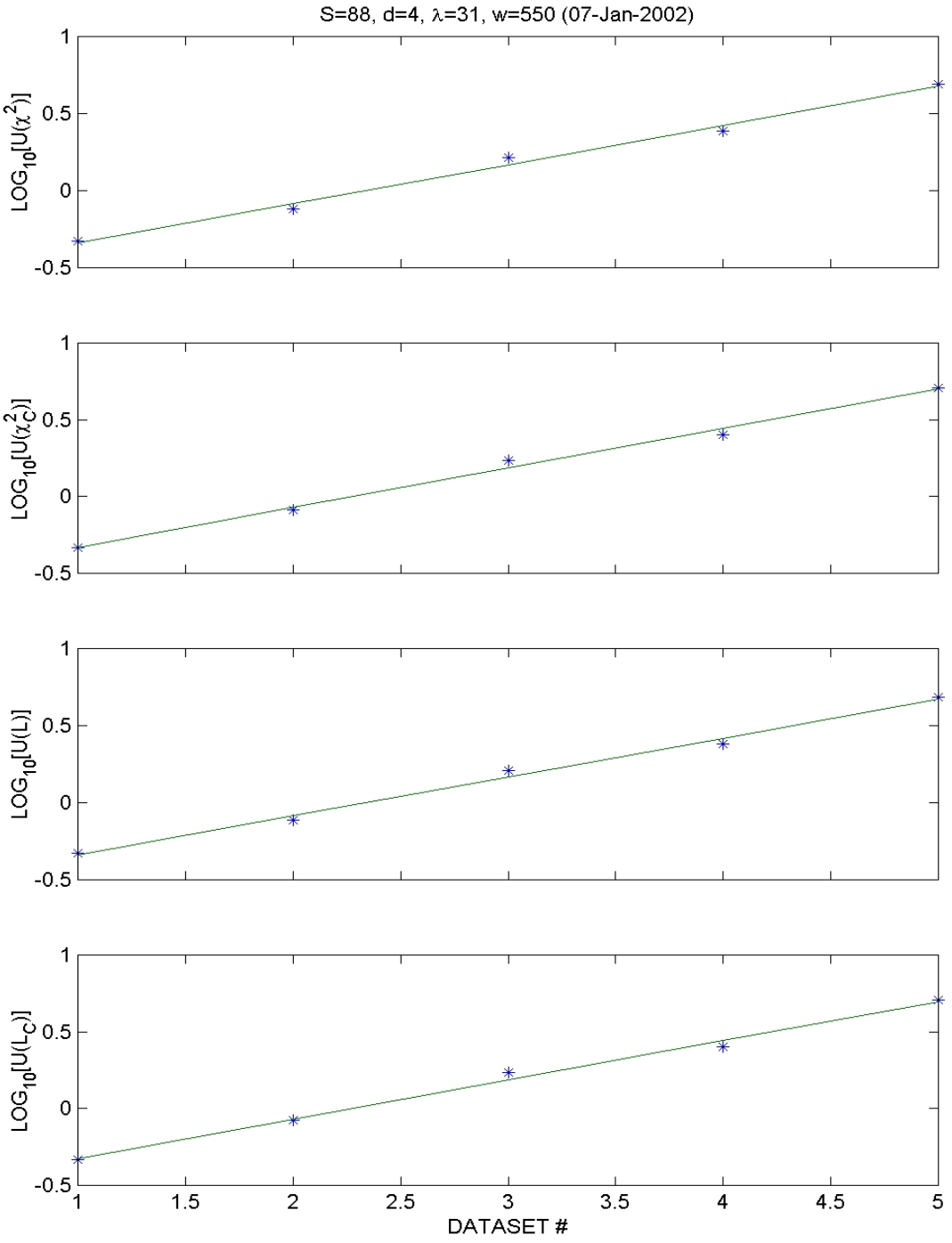

Fig. 8. Plots of the four nonlinear dissimilarity measures for the broken-rotor seeded-fault. The data are electrical power. The exponential rise in the severity of the seeded faults is shown as an almost linear rise (solid line) in the logarithm of all four dissimilarity measures (*) for the chosen set of phase-space parameters.

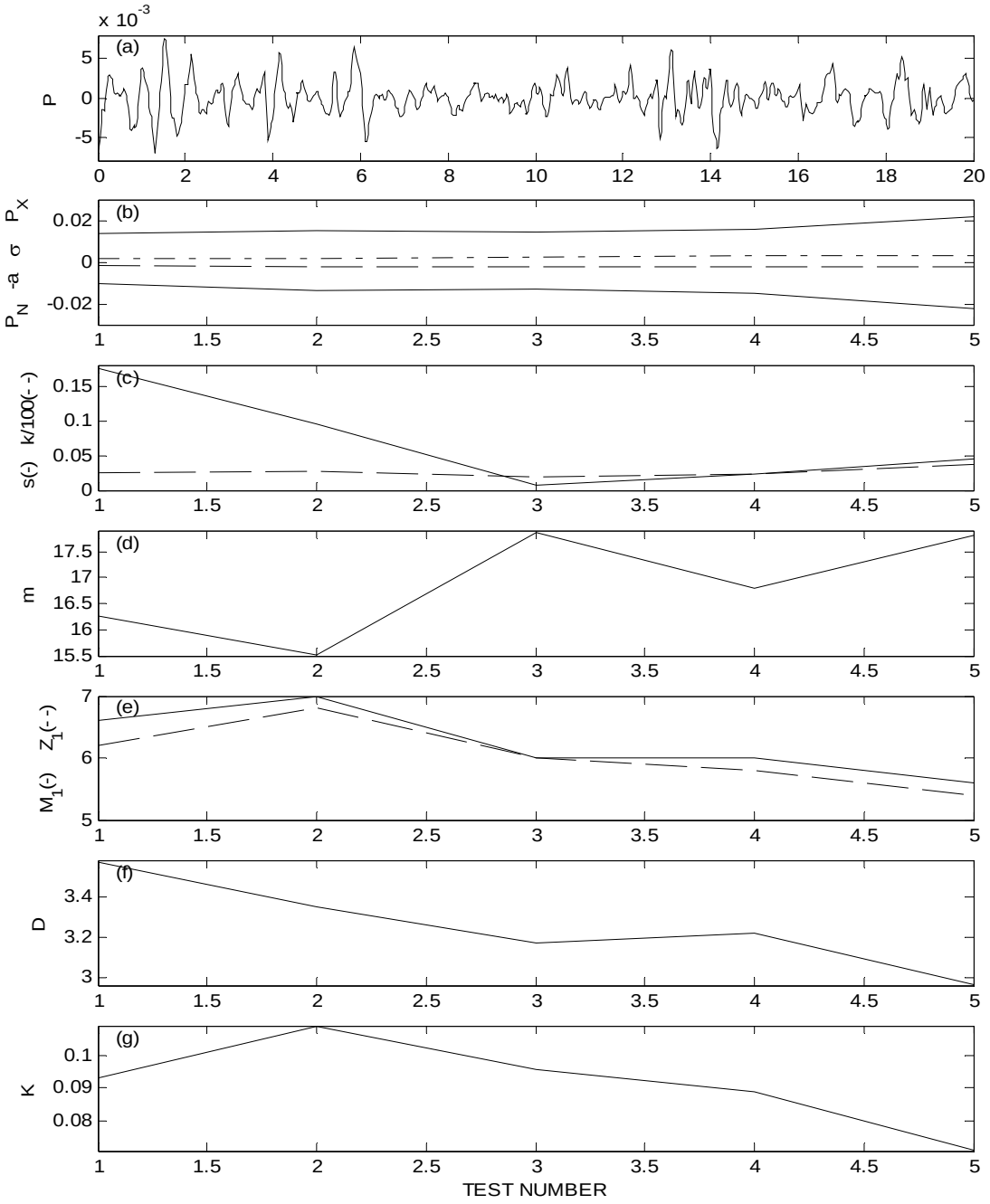

Fig. 9. Results for EPRI broken-rotor seeded fault from vibration power -- (a) Vibration power vs time (ms); (b) minimum (P_N), absolute average deviation (a), standard deviation (σ), and maximum (P_X) in vibration power vs test number; (c) skewness (s) and kurtosis (k) vs test number; (d) average number of time steps per cycle (m) vs test number; (e) first zero in the autocorrelation (Z_1) and first minimum in the mutual information function (M_1) vs test number; (f) correlation dimension (D) vs test number; and (g) Kolmogorov entropy (K) vs test number.

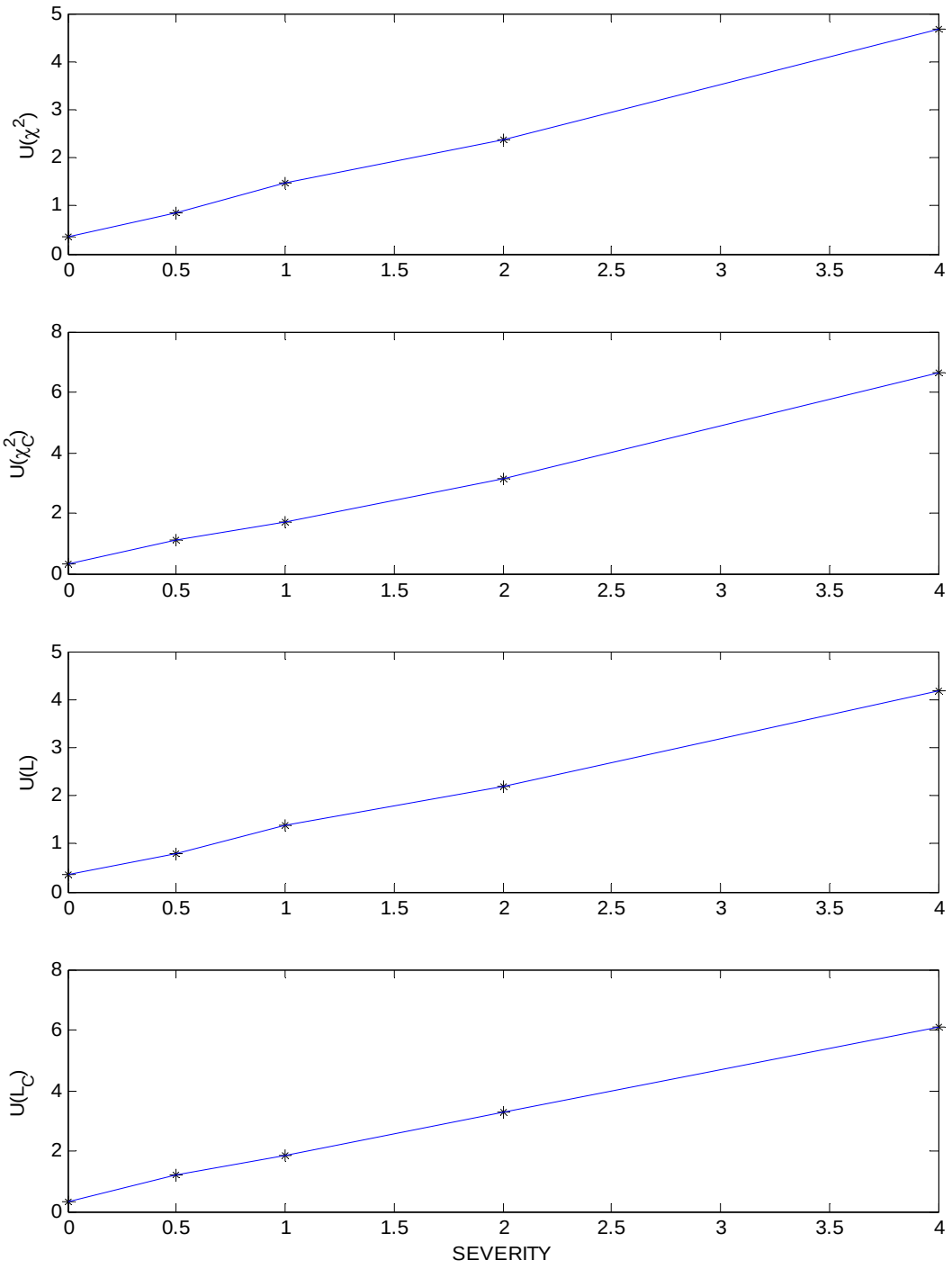

Fig. 10. Plots of the four nonlinear dissimilarity measures for the broken-rotor seeded-fault. The data are vibration power for the following phase-space parameters: $d = 3$, $S = 130$, $\lambda = 21$, $B = 5$, $N = 12000$.

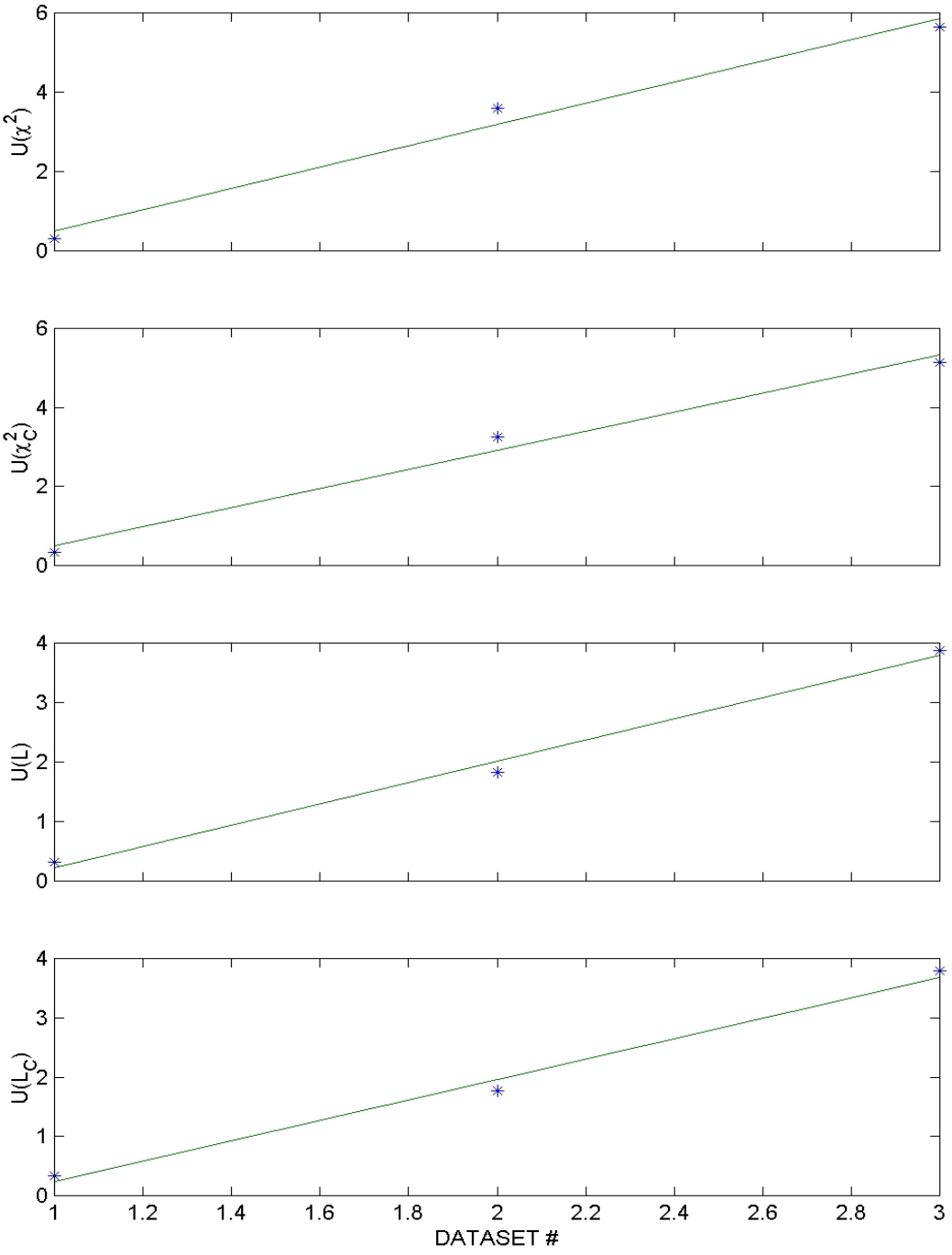

Fig. 11. The four nonlinear dissimilarity measures for the turn-to-turn short seeded-fault. The data are electrical power data. Dataset No. 1 is for the nominal (no fault) state. Dataset No. 2 is for the 2.7-ohm short. Dataset No. 3 is for the 1.35-ohm short. The straight line is the least-squares fit to the points (*) for the best set of phase-space parameters: $S = 129$, $d = 3$, $\lambda = 1$, and $w = 221$.

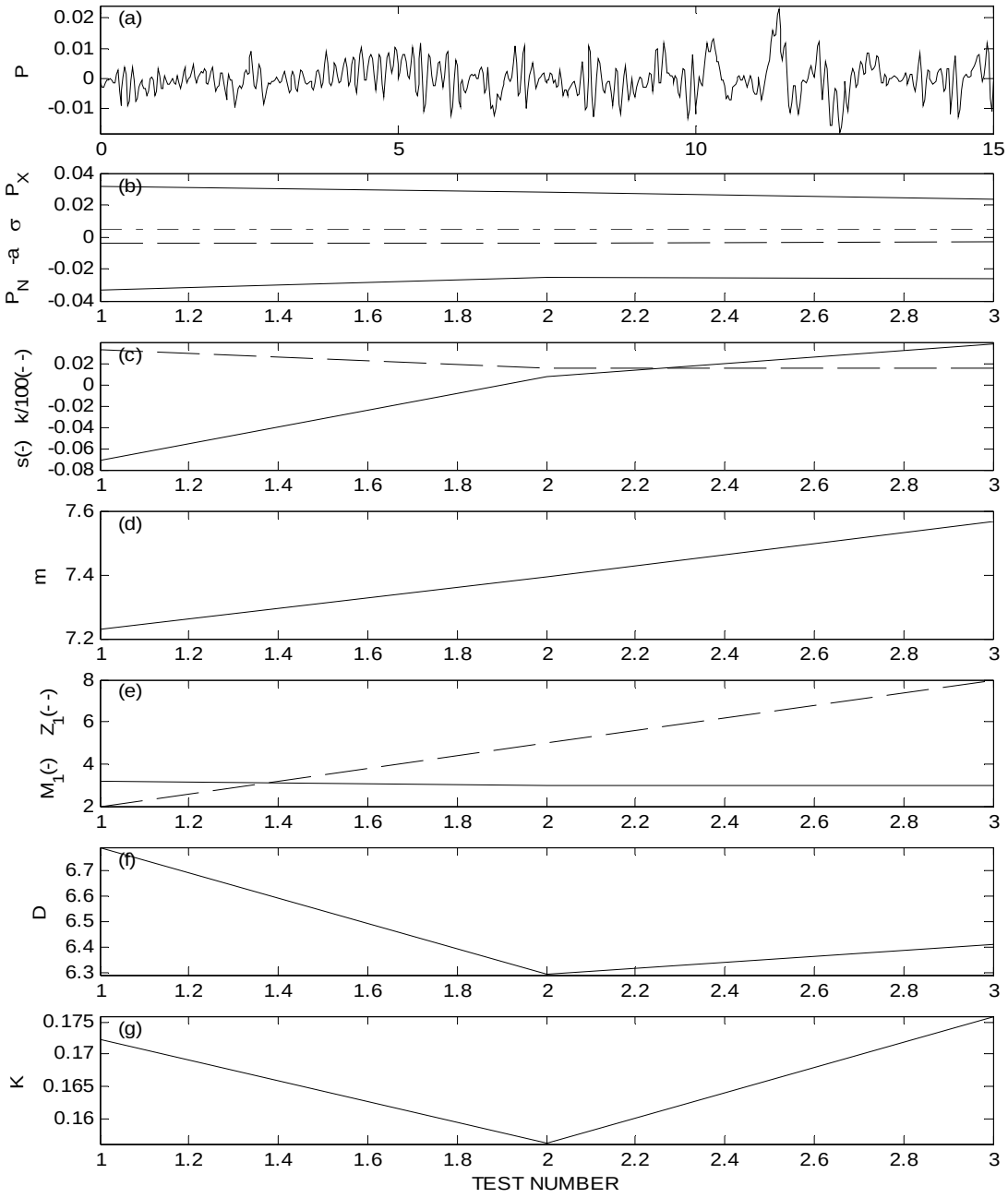

Fig. 12. Results for EPRI turn-to-turn seeded fault from vibration power -- (a) Vibration power vs time (ms); (b) minimum (P_N), absolute average deviation (a), standard deviation (σ), and maximum (P_X) in vibration power vs test number; (c) skewness (s) and kurtosis (k) vs test number; (d) average number of time steps per cycle (m) vs test number; (e) first zero in the autocorrelation (Z_1) and first minimum in the mutual information function (M_1) vs test number; (f) correlation dimension (D) vs test number; and (g) Kolmogorov entropy (K) vs test number.

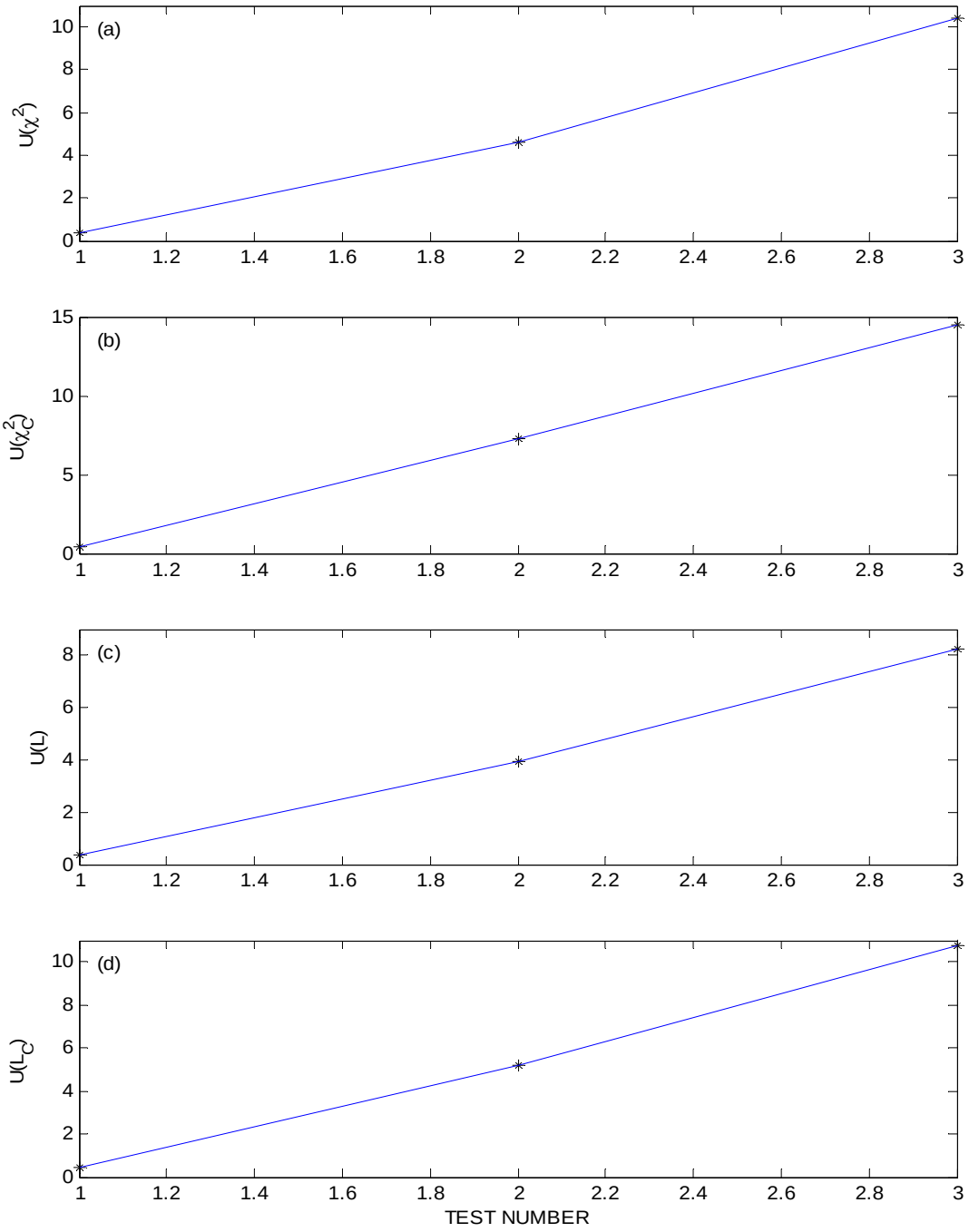

Fig. 13. The four nonlinear dissimilarity measures for the turn-to-turn short seeded-fault. The data are vibration power. Dataset No. 1 is for the nominal (no fault) state. Dataset No. 2 is for the 2.7-ohm short. Dataset No. 3 is for the 1.35-ohm short. This result is for the best set of phase-space parameters: $S = 2$, $d = 6$, $\lambda = 57$, $B = 5$, and $N = 12000$.

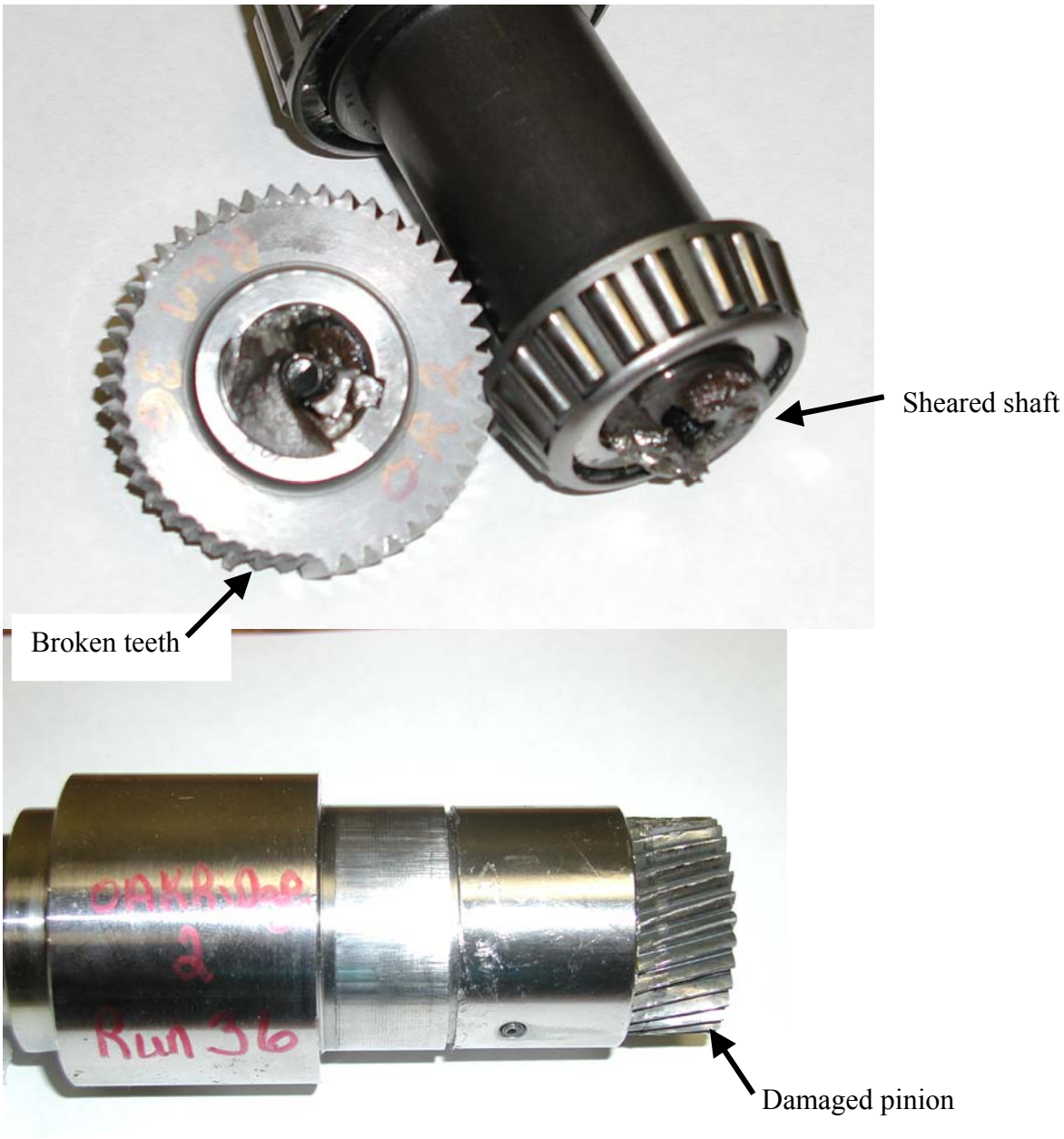

Fig. 14. End-of-life failure in PSU Run No. 36, (pinion damage, sheared shaft, and broken teeth.)

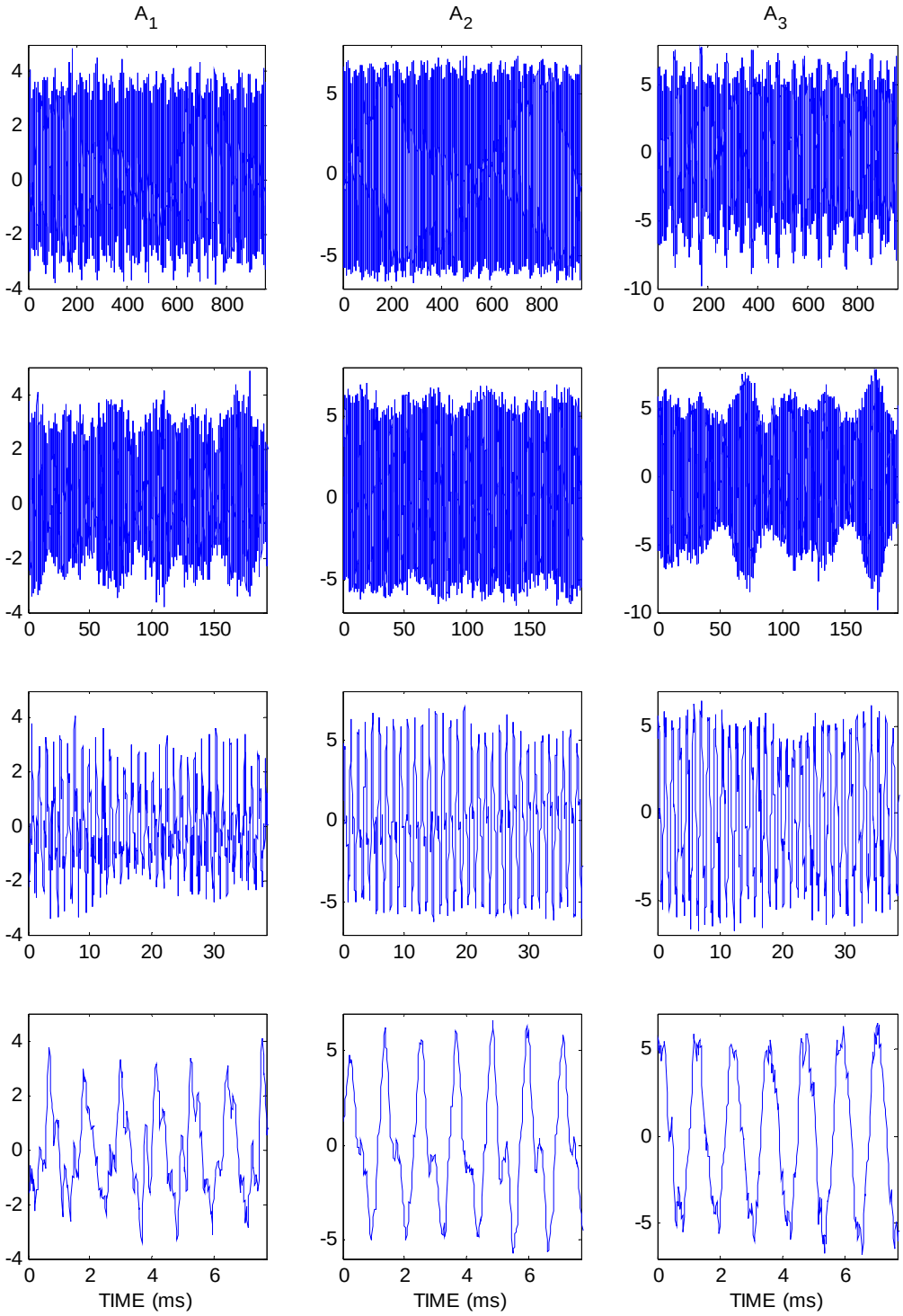

Fig. 15. Raw data for PSU MDTB Run No. 36. Data are from each of the three acceleration directions (A_i), over successively shorter time scales to show the complex, nonlinear features.

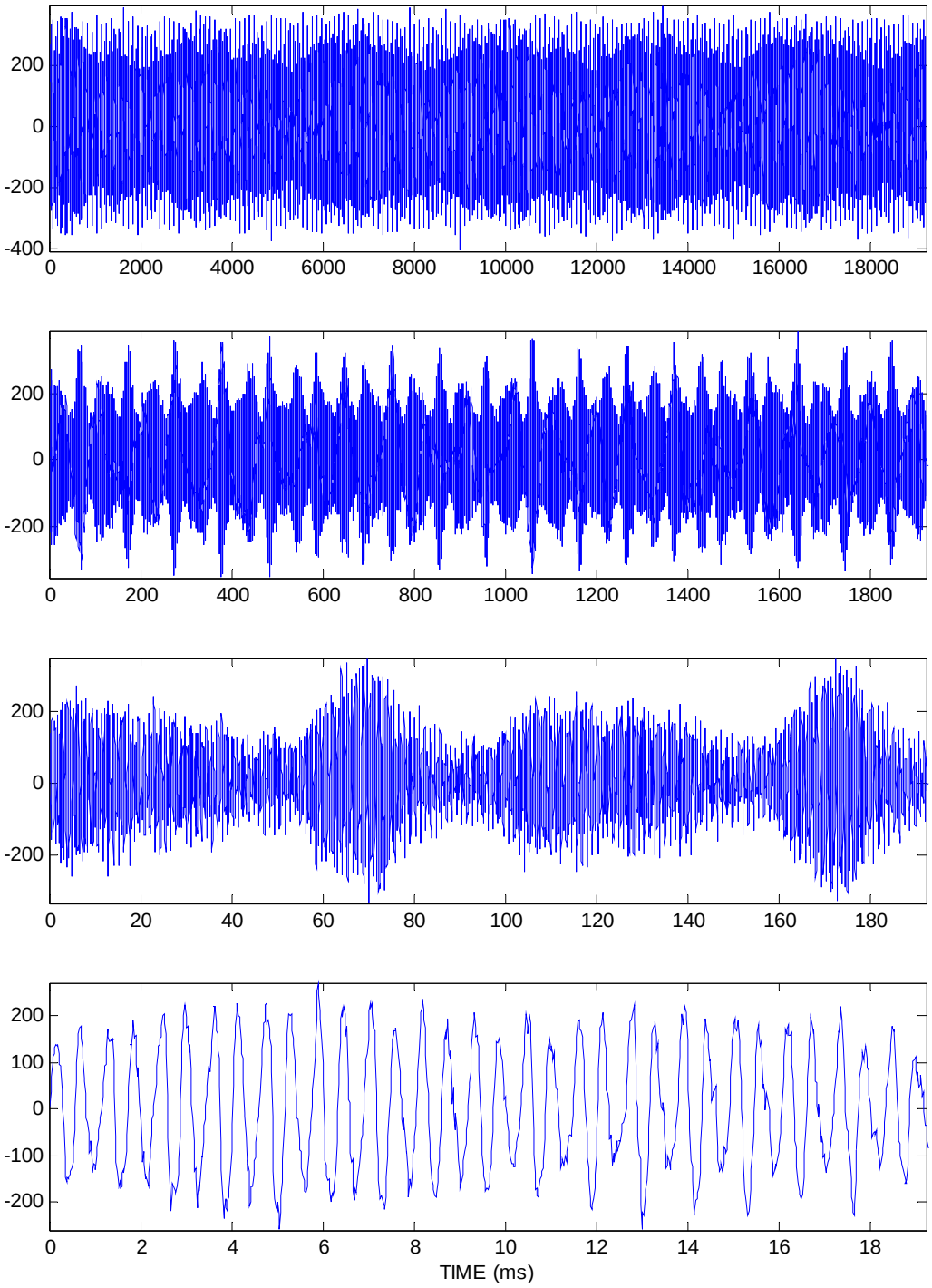

Fig. 16. Vibration power for PSU MDTB Run No. 36. Subplots show successively shorter time scales with complex, nonlinear features.

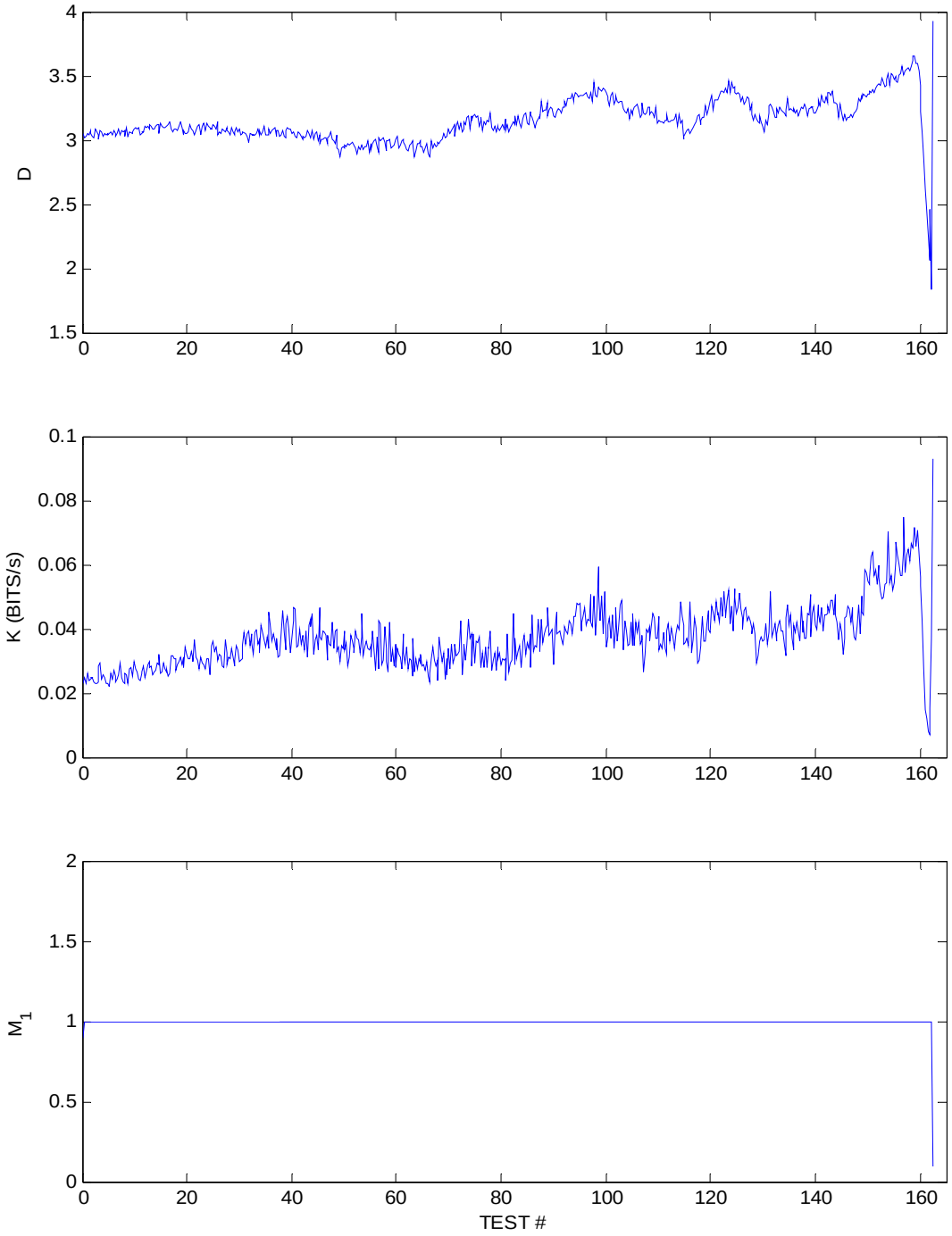

Fig. 17. Traditional nonlinear measures for the MDTB Run No. 36. Vibration power data were analyzed for this accelerated failure test: (top) correlation dimension, (middle) Kolmogorov entropy, and (bottom) first minimum in the mutual information function, M_1.

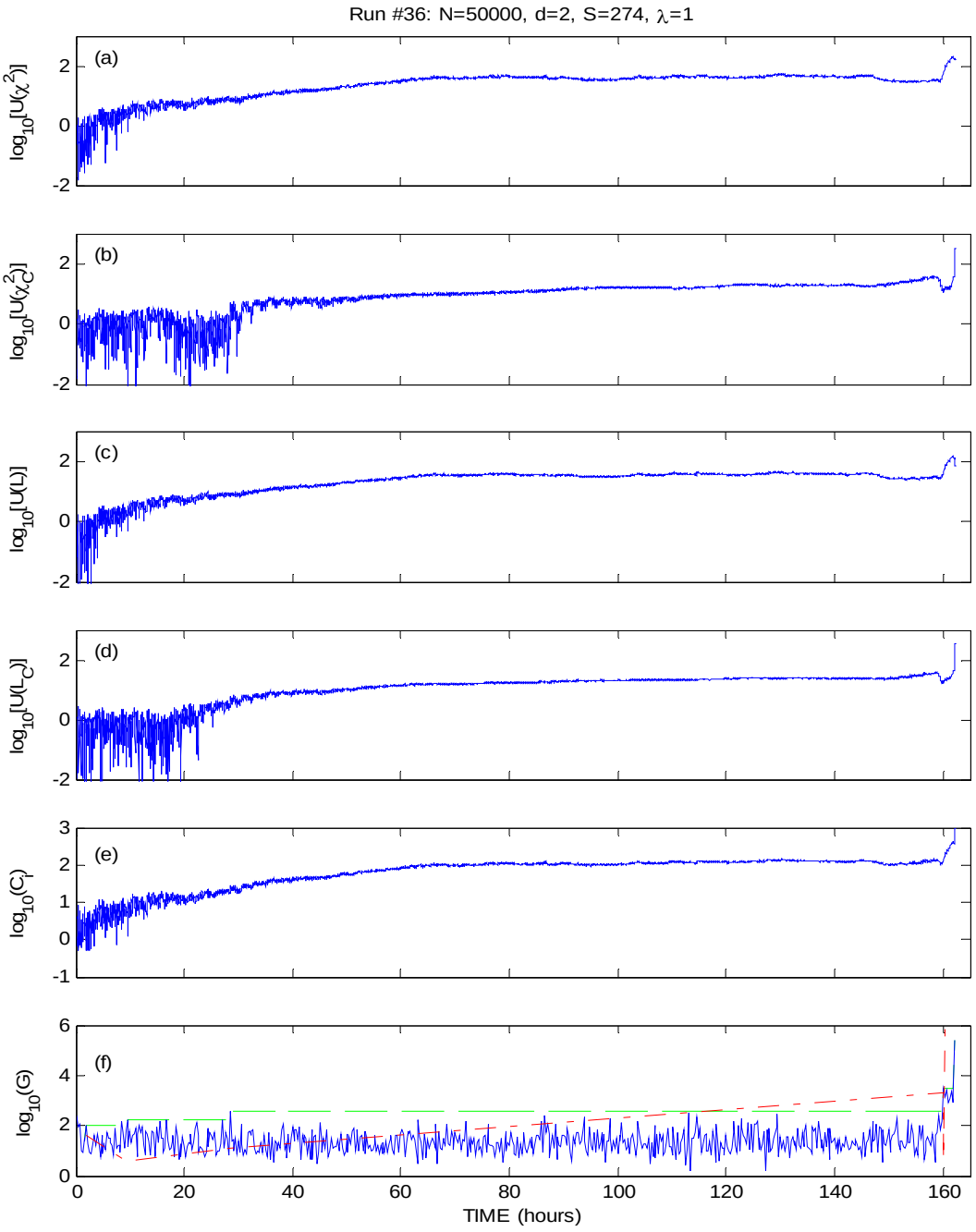

Fig. 18. Phase-space dissimilarity measures vs time for the MDTB (Run No. 36). The data are from vibration power: (a) – (d) the four renormalized PSDM; (e) composite measure, C_i, of the four PSDM; (f) end-of-life indicator, G (solid), running maximum of G (dashed), and ratio, r, of successive maxima (-.-) in G. Note that the vertical axis is the $\log_{10}$ of the parameter in subplots (a)−(f), and that $3\log_{10}(r)$ is plotted in (f) for clarity. The phase-space parameters are $S = 274$, $d = 2$, and $\lambda = 1$, that are identical to those used for analysis of PSU MDTB data in PY2 to show consistency.

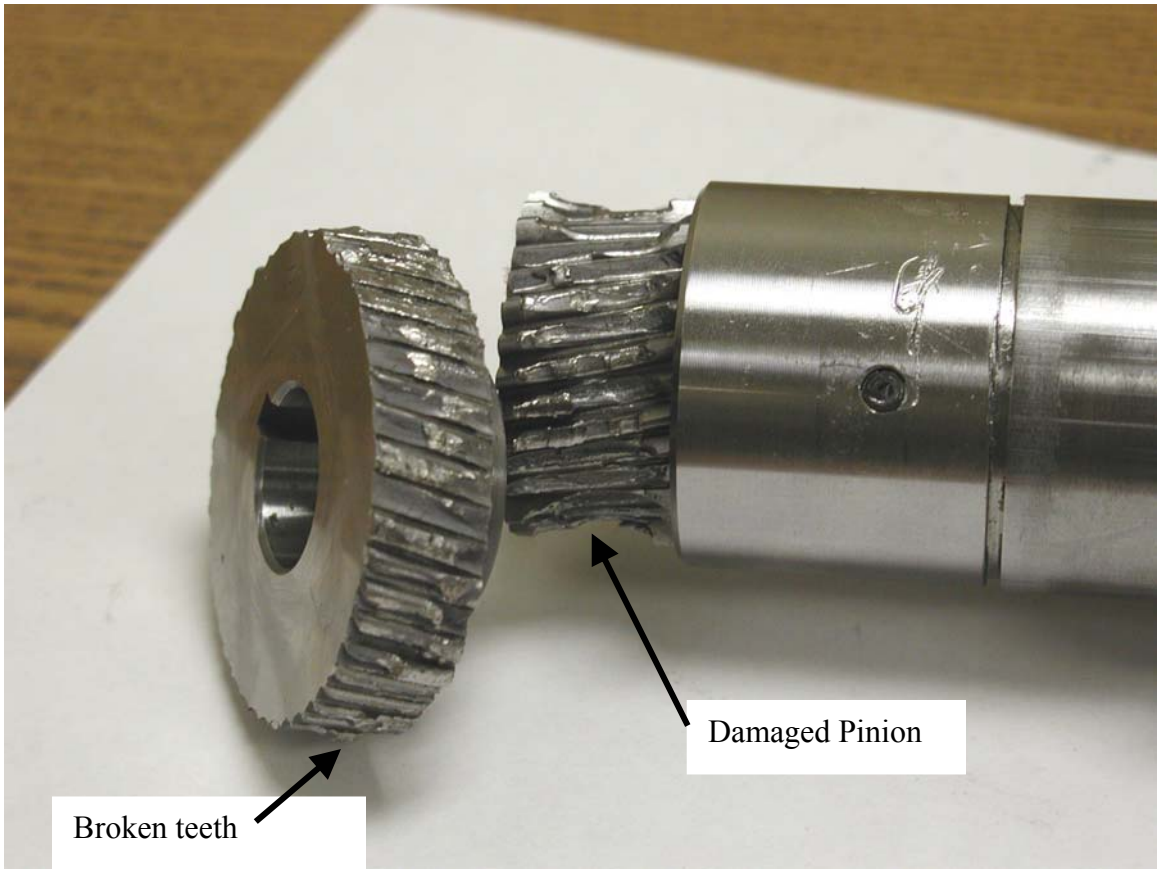

Fig. 19. End-of-life failure in PSU Run No. 37 (pinion damage and broken teeth).

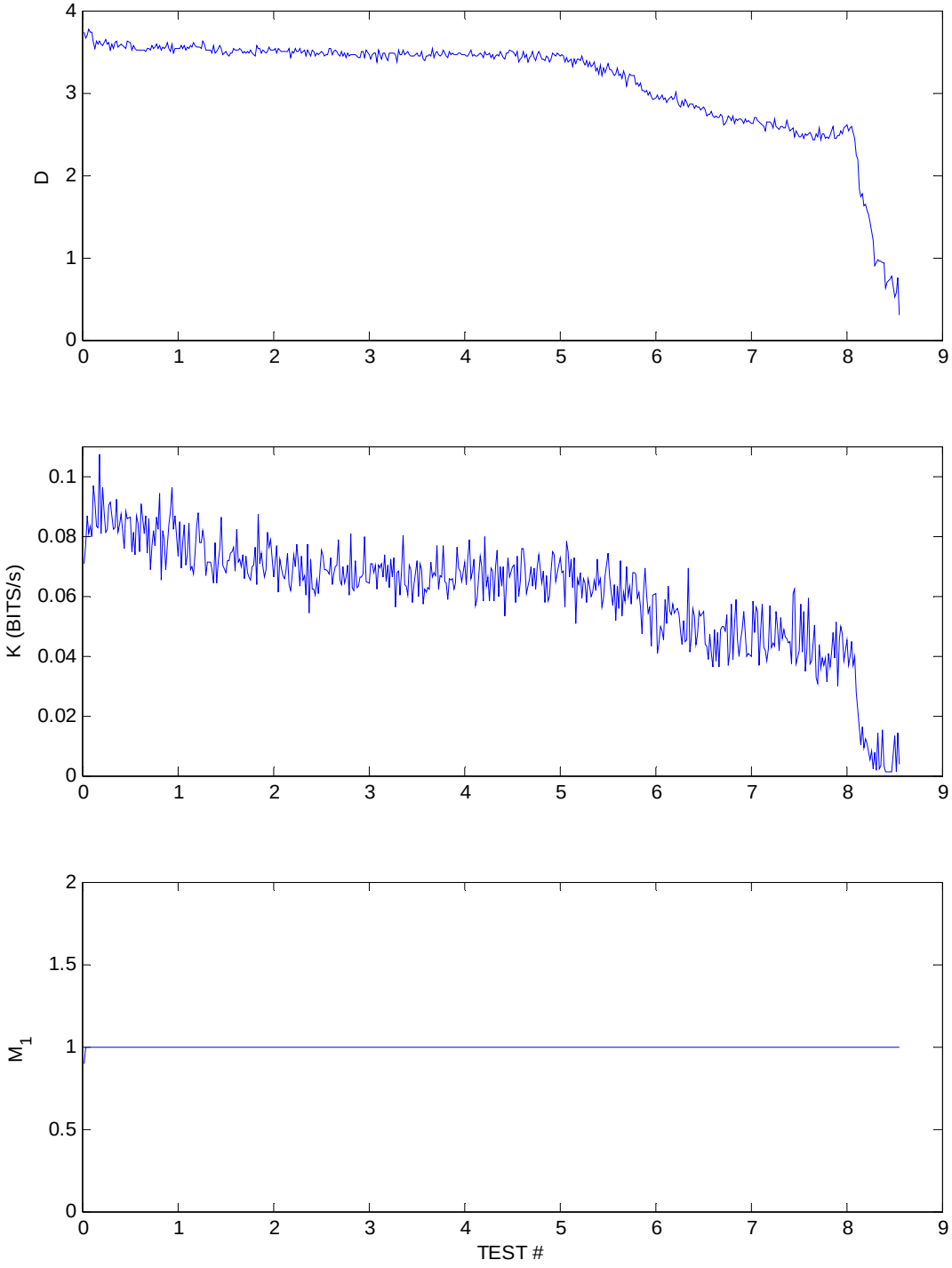

Fig. 20. Traditional nonlinear measures for the MDTB Run No. 37. The data are vibration power for this accelerated failure test.

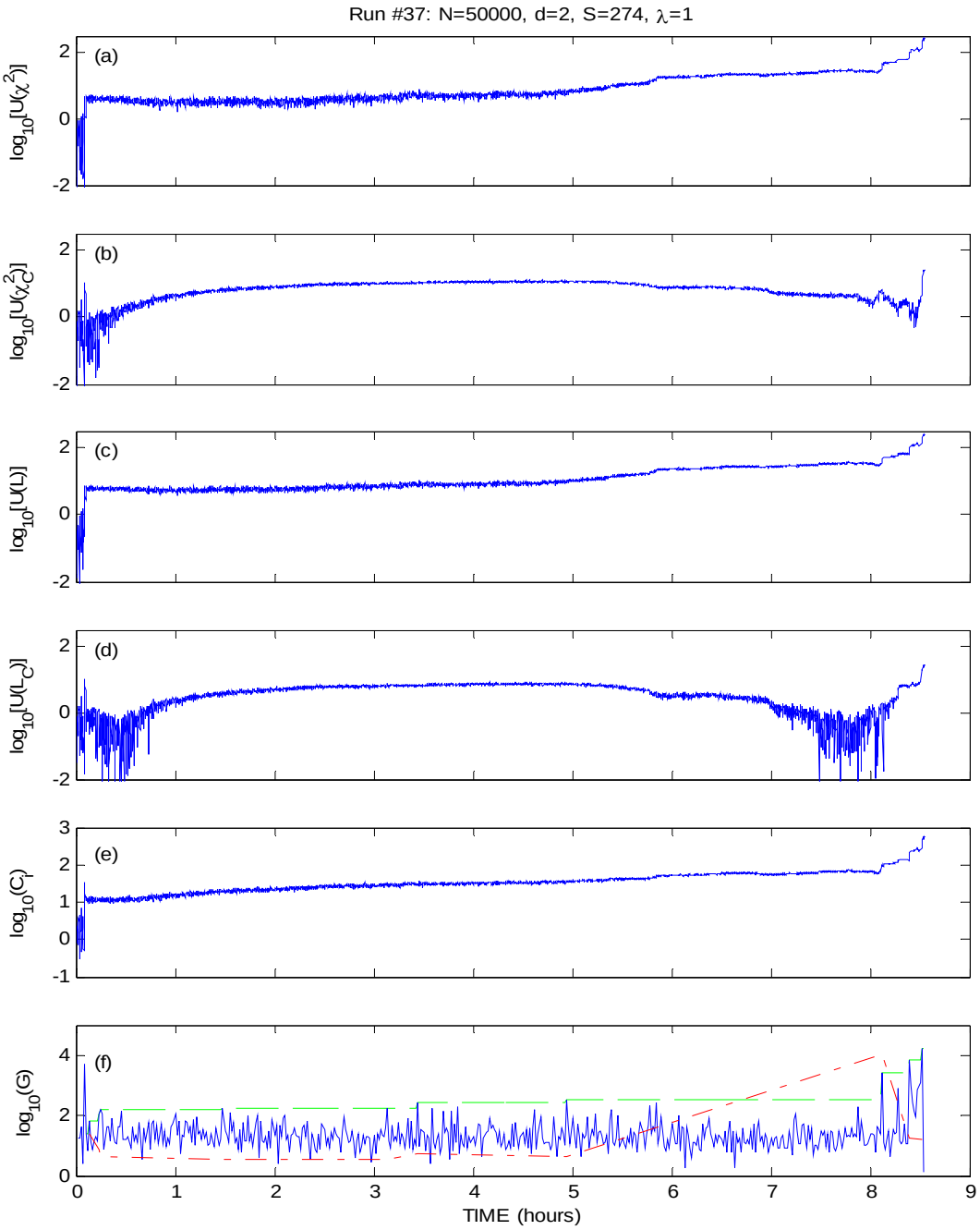

Fig. 21. Phase-space dissimilarity measures vs time for the MDTB (Run No. 37). He data are from vibration power: (a) – (d) the four renormalized PSDM; (e) composite measure, C_i, of the four PSDM; (f) end-of-life indicator, G (solid), running maximum of G (dashed), and ratio, r, of successive maxima (-.-) in G. Note that the vertical axis is the $\log_{10}$ of the parameters in subplots (a)−(f), and that $r/2$ is plotted in (f) for clarity. The phase-space parameters are $S = 274$, $d = 2$, and $\lambda = 1$, which are identical to those used for analysis of PSU MDTB data in PY2 to show consistency.

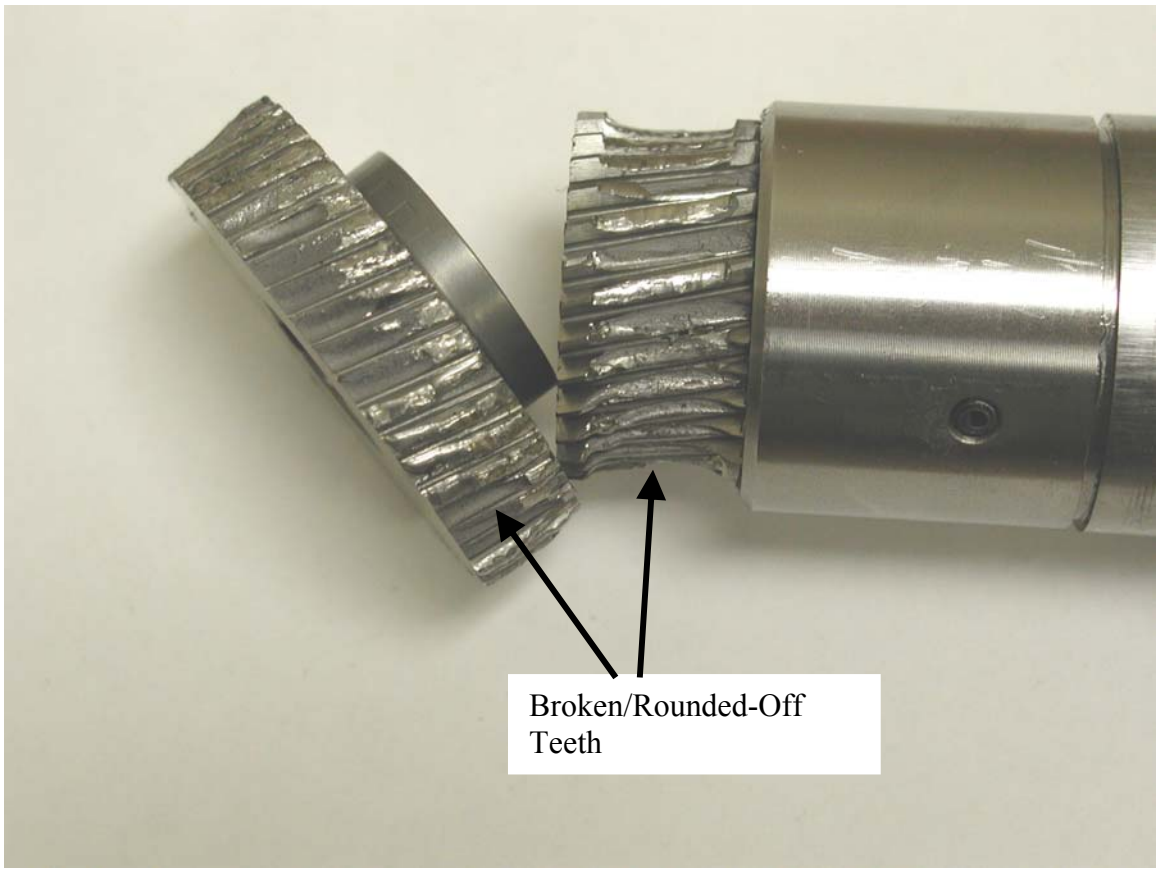

Fig. 22. End-of-life failure in PSU Run No. 38 (broken/rounded-off teeth on both the gear and pinion).

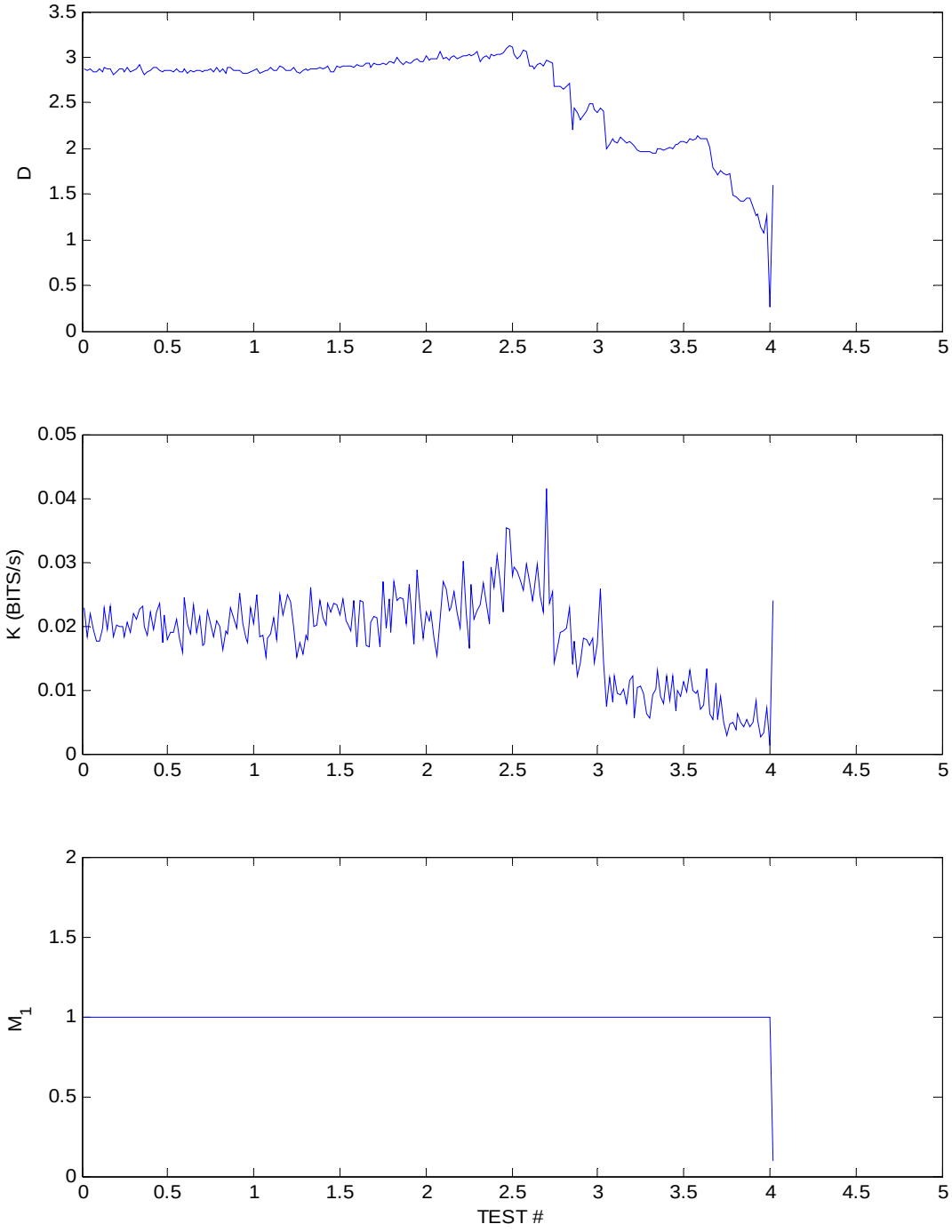

Fig. 23. Traditional nonlinear measures for the MDTB Run No. 38. This accelerated failure test used vibration power data: (top) correlation dimension, (middle) Kolmogorov entropy, and (bottom) first minimum in the mutual information function.

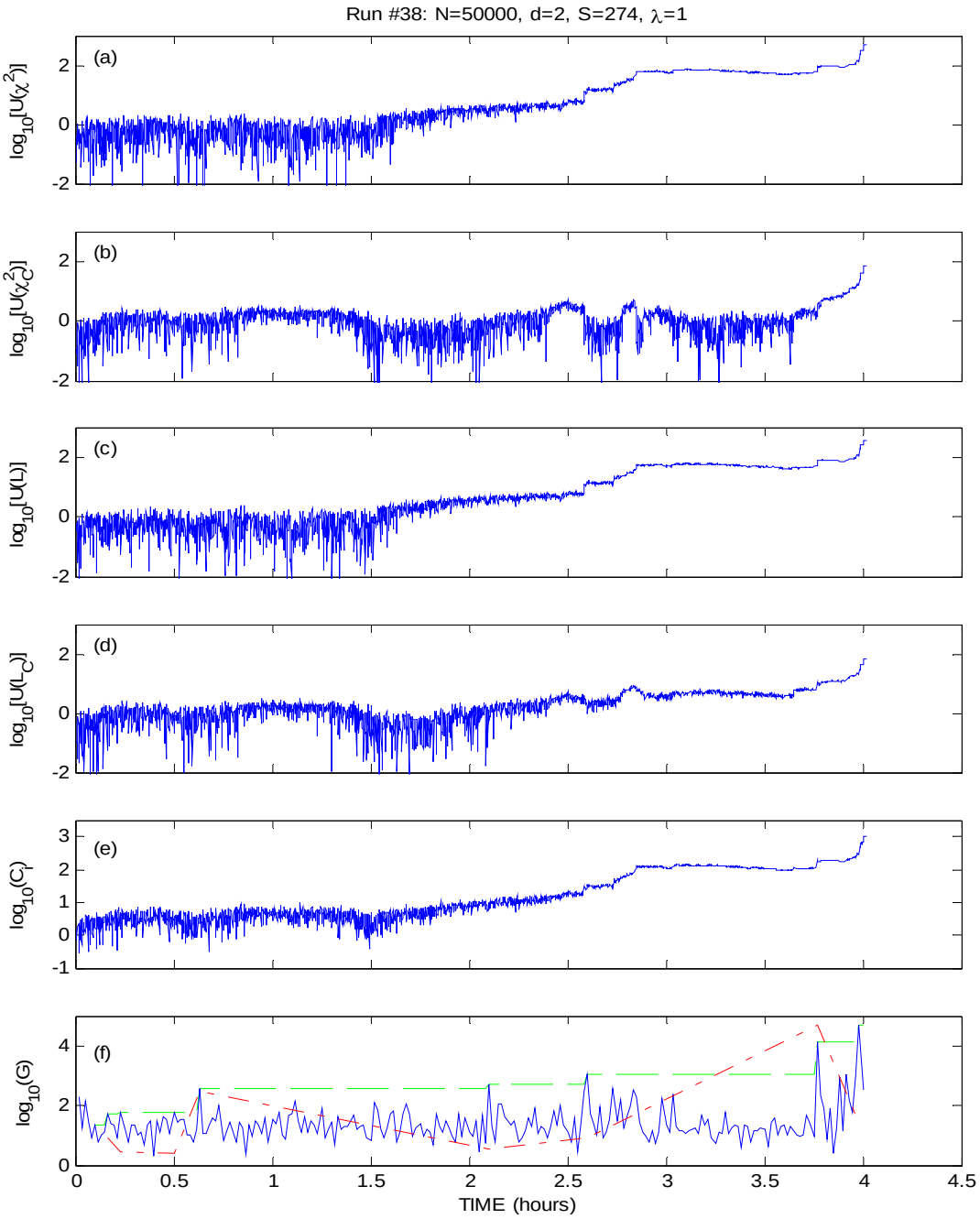

Fig. 24. Phase-space dissimilarity measures vs time for the MDTB (Run No. 38). The data are from vibration power: (a)–(d) the four renormalized PSDM; (e) composite measure, C_i, of the four PSDM; (f) end-of-life indicator, G (solid), running maximum of G (dashed), and ratio, r, of successive maxima (-.-) in G. Note that the vertical axis is the $\log_{10}$ of the parameter in subplots (a)−(f), and that $0.4r$ is plotted in (f) for clarity. The phase-space parameters are $S = 274$, $d = 2$, and $\lambda = 1$, which are identical to those used for analysis of PSU MDTB data in PY2 to show consistency.

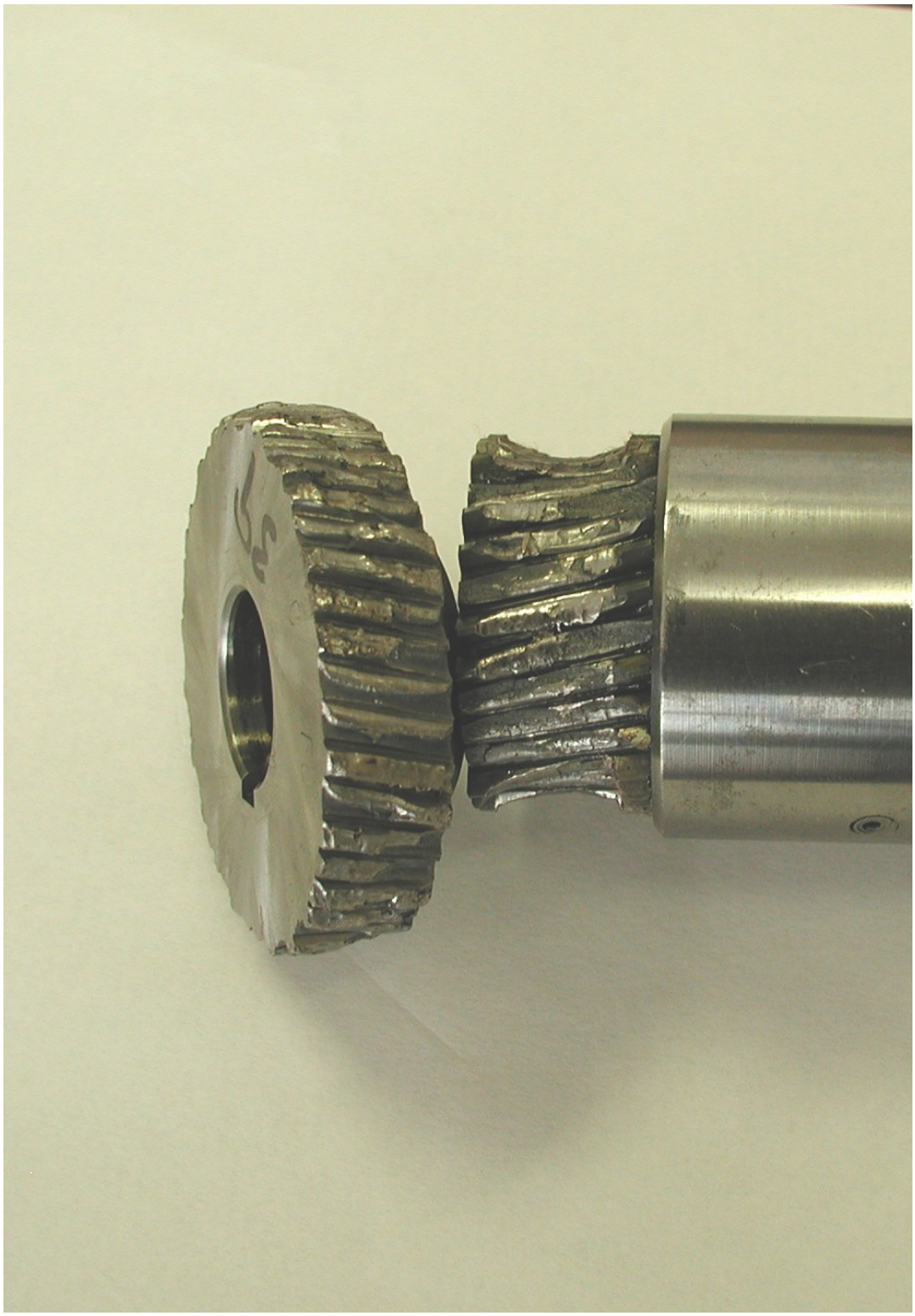

Fig. 25. End-of-life failure in PSU Run No. 39 (broken/rounded-off teeth on both the gear and pinion).

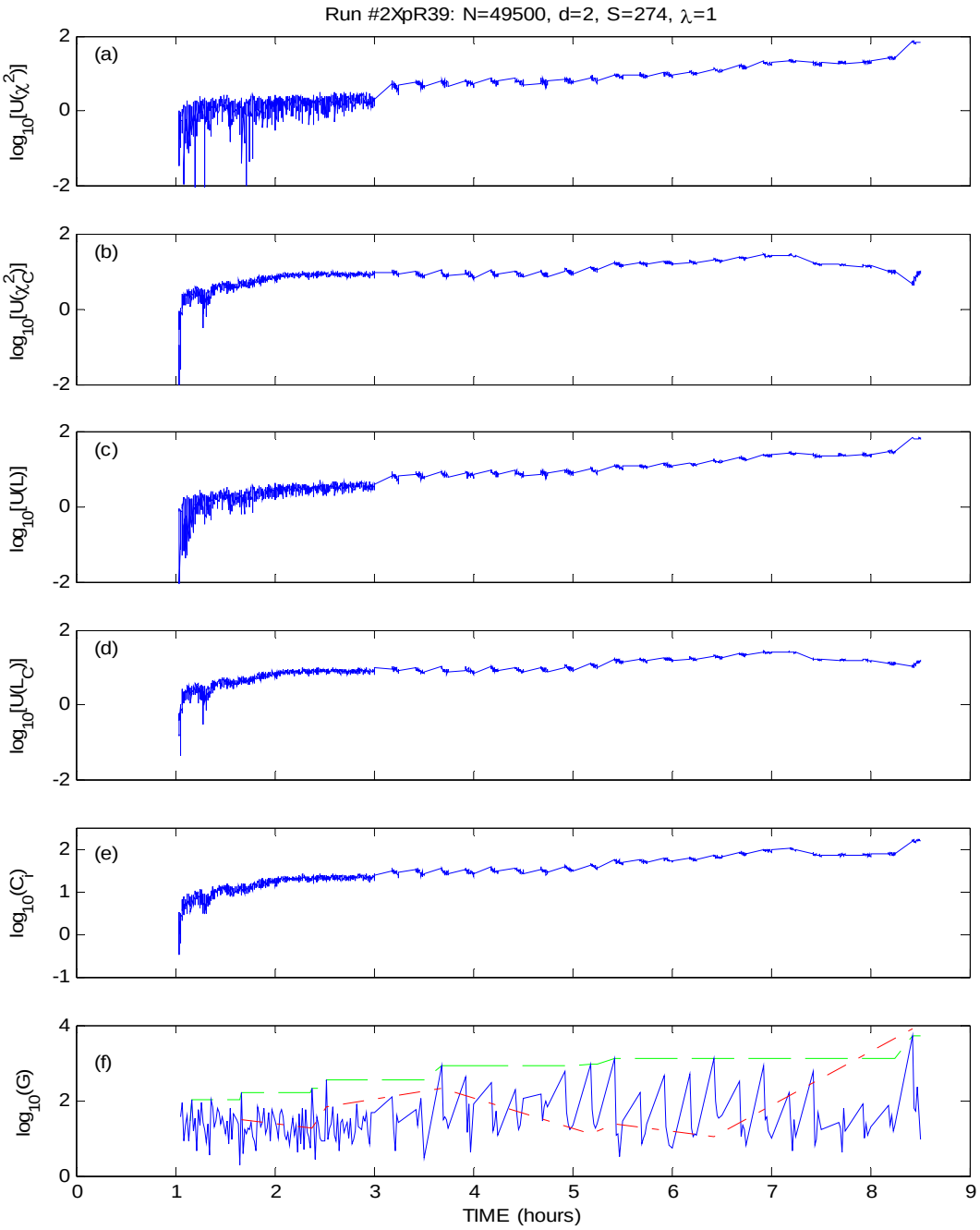

Fig. 26. Phase-space dissimilarity measures vs time for the MDTB (Run No. 39 at 2X load). The data are from vibration power: (a)–(d) the four renormalized PSDM; (e) composite measure, C_i, of the four PSDM; (f) end-of-life indicator, G (solid), running maximum of G (dashed), and ratio, r, of successive maxima (-.-) in G. Note that the vertical axis is the $\log_{10}$ of the parameter in subplots (a)−(f). The phase-space parameters are $S = 274$, $d = 2$, and $\lambda = 1$, which are identical to those used for analysis of PSU MDTB data in PY2 to show consistency.

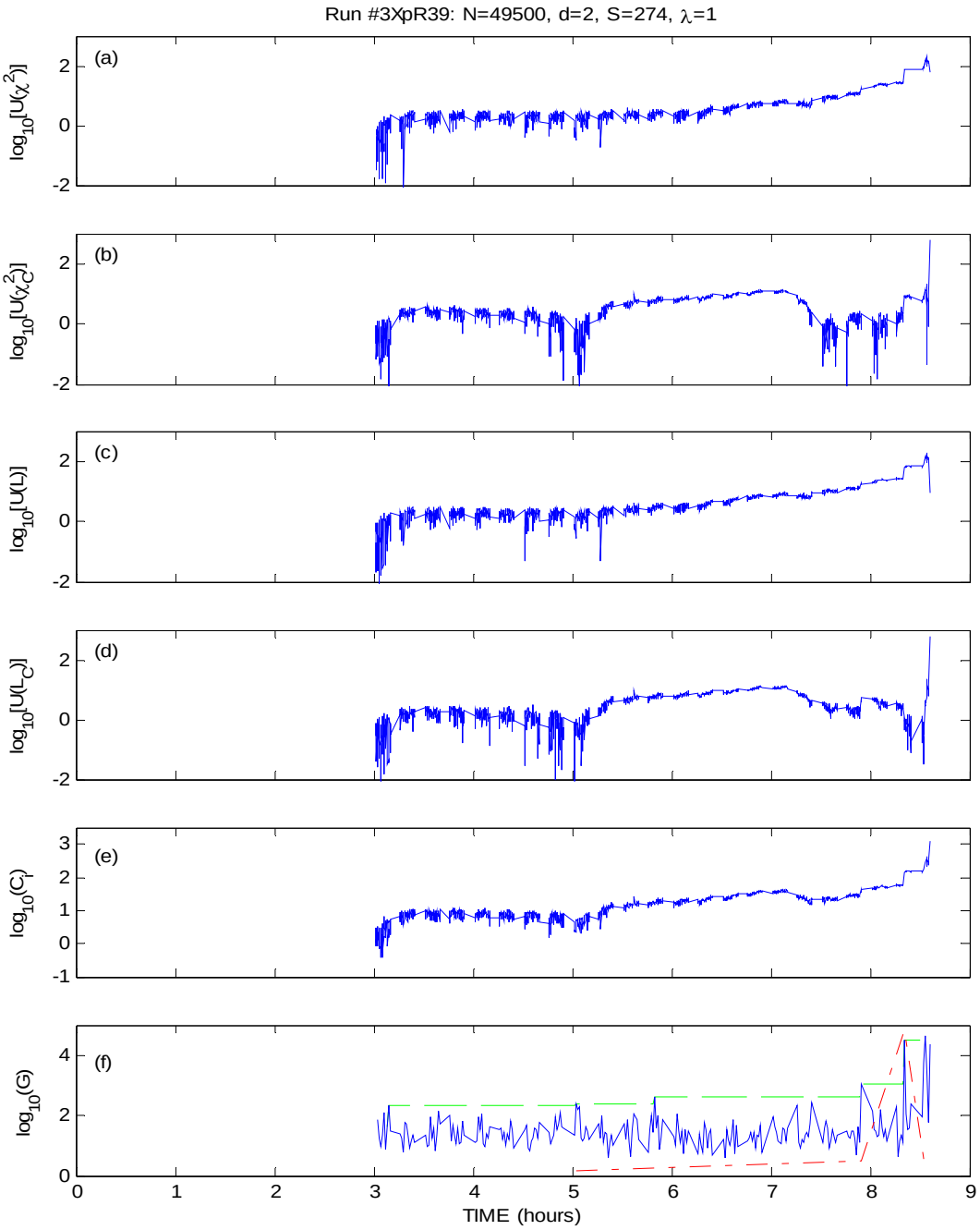

Fig. 27. Phase-space dissimilarity measures vs time for the MDTB (Run No. 39 at 3X load). The data are from vibration power: (a)–(d) the four renormalized PSDM; (e) composite measure, C_i, of the four PSDM; (f) end-of-life indicator, G (solid), running maximum of G (dashed), and ratio, r, of successive maxima (-.-) in G. Note that the vertical axis is the $\log_{10}$ of the parameter in subplots (a)−(f). The phase-space parameters are $S = 274$, $d = 2$, and $\lambda = 1$, that are identical to those used for analysis of PSU MDTB data in PY2 to show consistency.

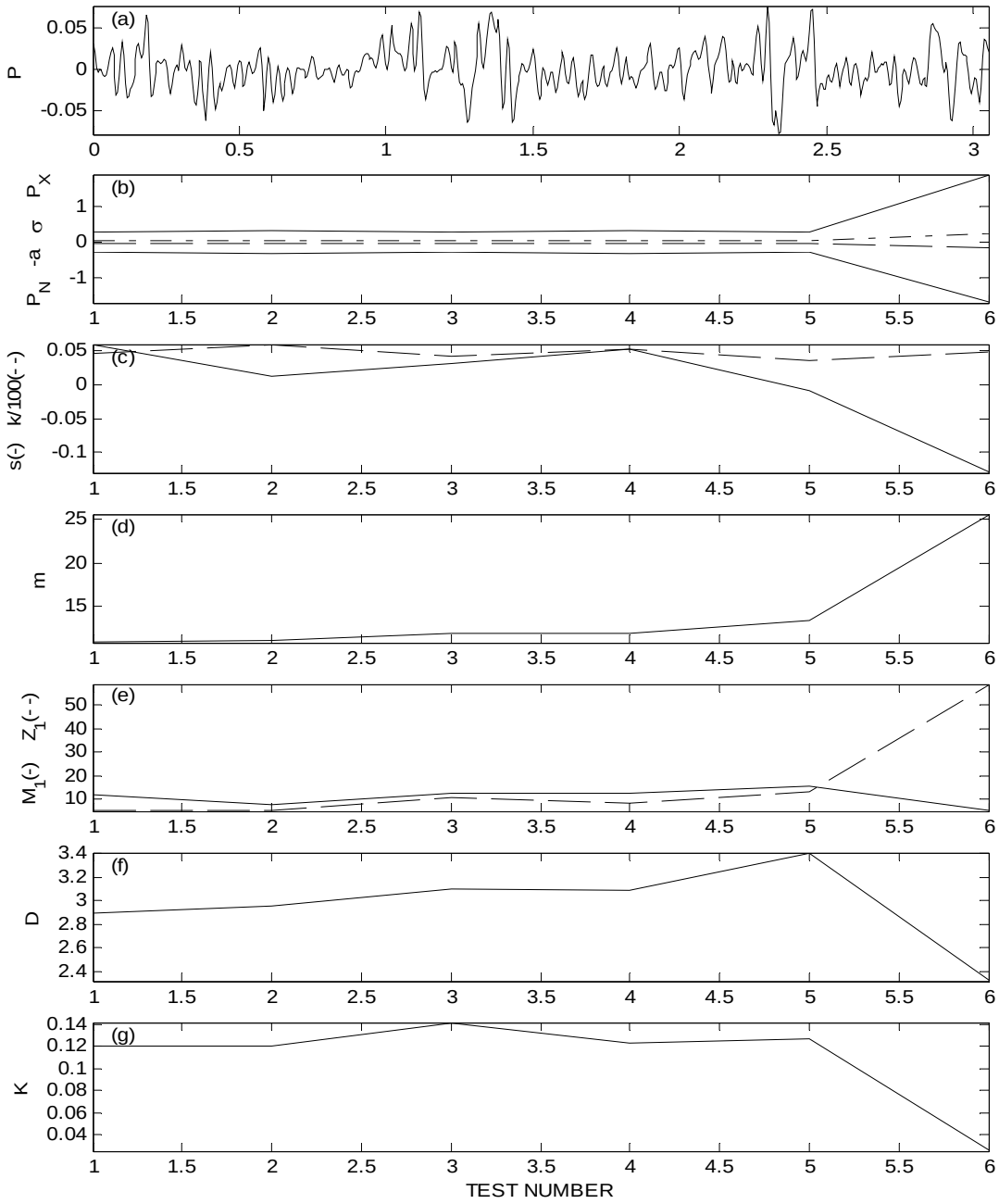

Fig. 28. Results for PSU shaft-crack seeded fault: (a) vibration power (*P*) vs time (ms); (b) minimum (P_N), negative of the absolute average deviation (-*a*), standard deviation (σ), and maximum (P_X) of *P* for each test; (c) skewness (*s*) and kurtosis (*k*); (d) number of time steps per cycle (*m*); (e) first minimum in the mutual information function (M_1) and first zero in the autocorrelation (Z_1); (f) correlation dimension (*D*); and (g) Kolmogorov entropy (*K*).

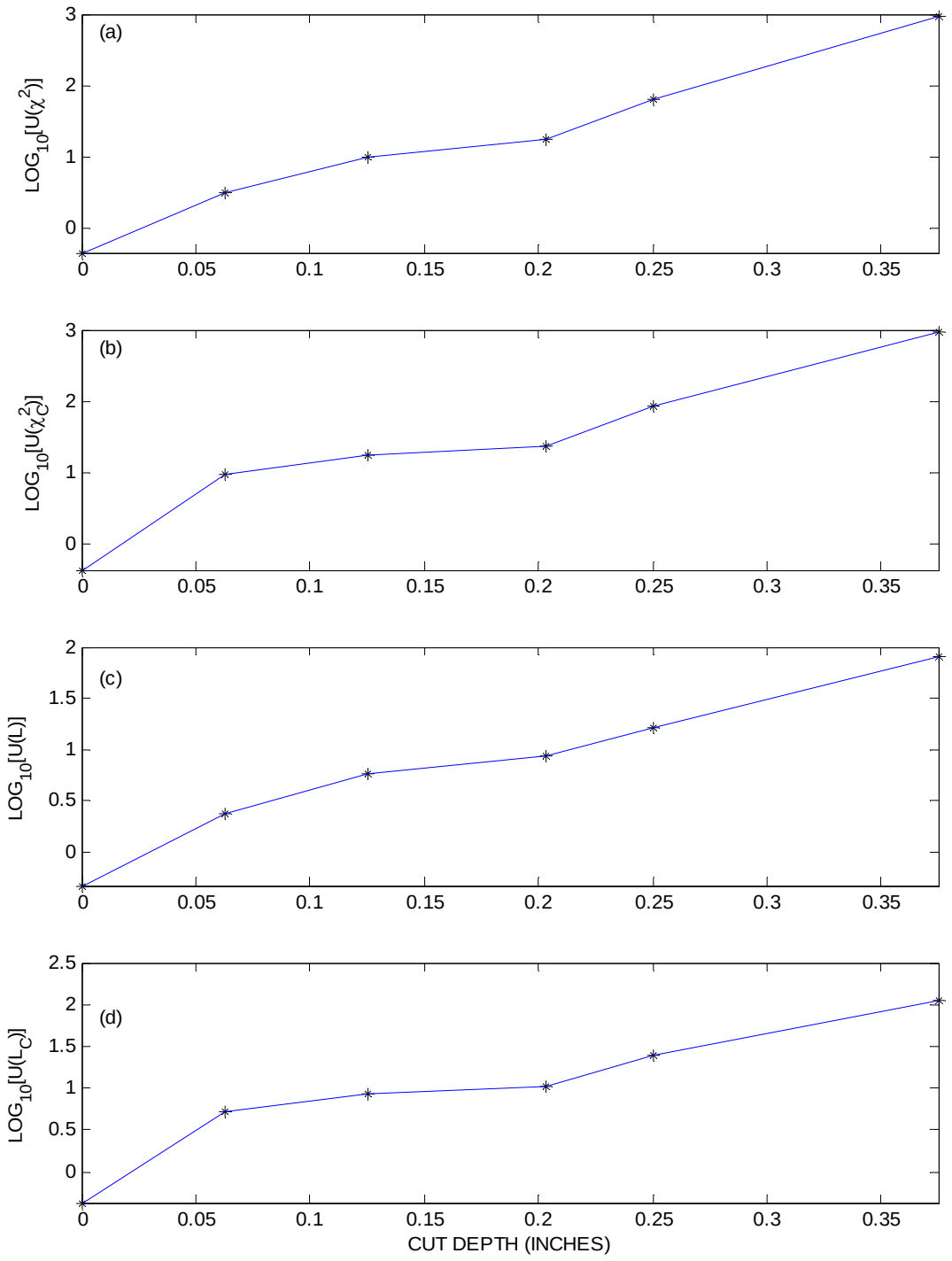

Fig. 29. The four PSDM vs cut depth for the shaft-crack seeded-fault. The data are from vibration power. This result is for the best set of phase-space parameters: $S = 2$, $d = 4$, $\lambda = 23$, $B = 10$, and $N = 100{,}000$.

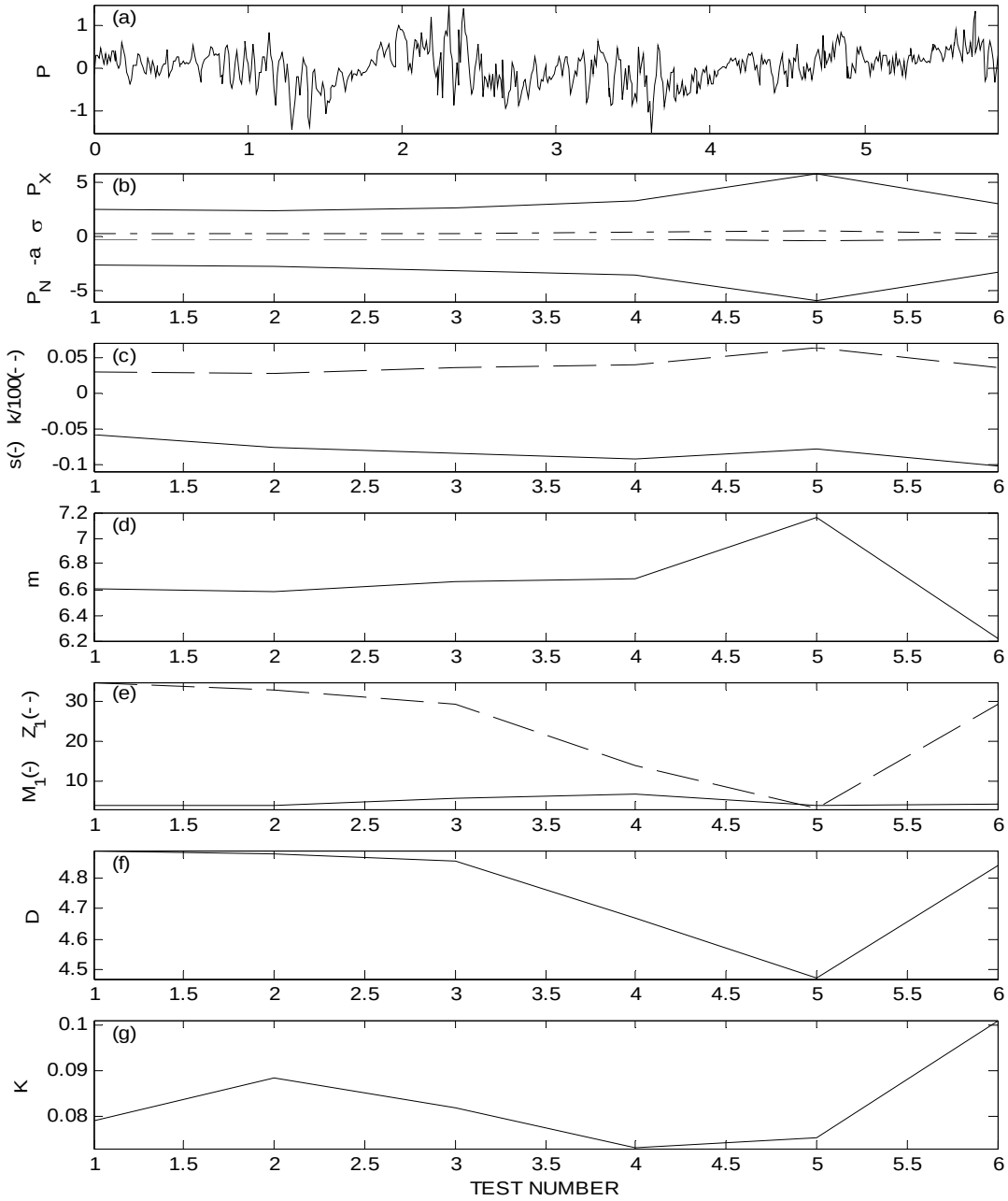

Fig. 30. Results for PSU turn-to-turn seeded generator fault: (a) vibration power (P) vs time (ms); (b) minimum (P_N), negative of the absolute average deviation ($-a$), standard deviation (σ), and maximum (P_X) of P for each test; (c) skewness (s) and kurtosis (k); (d) number of time steps per cycle (m); (e) first minimum in the mutual information function (M_1) and first zero in the autocorrelation (Z_1); (f) correlation dimension (D); and (g) Kolmogorov entropy (K).

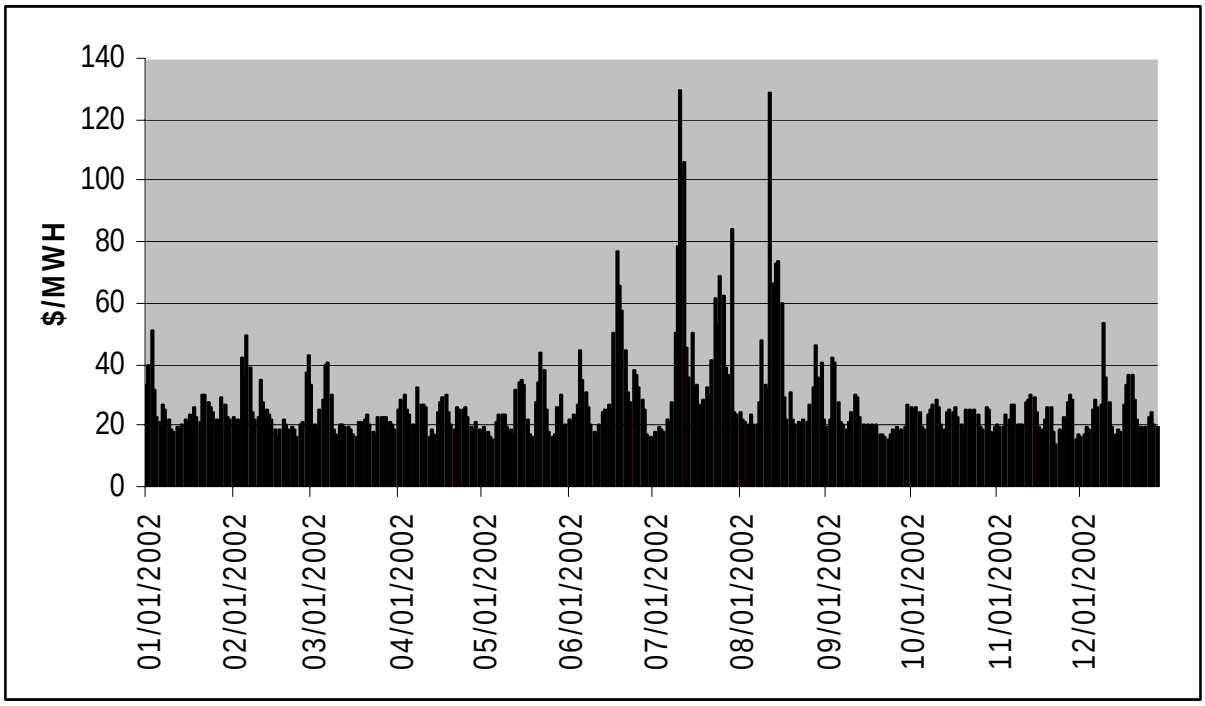

Fig. 31. Predicted daily average wholesale electricity price forecast for 2002.

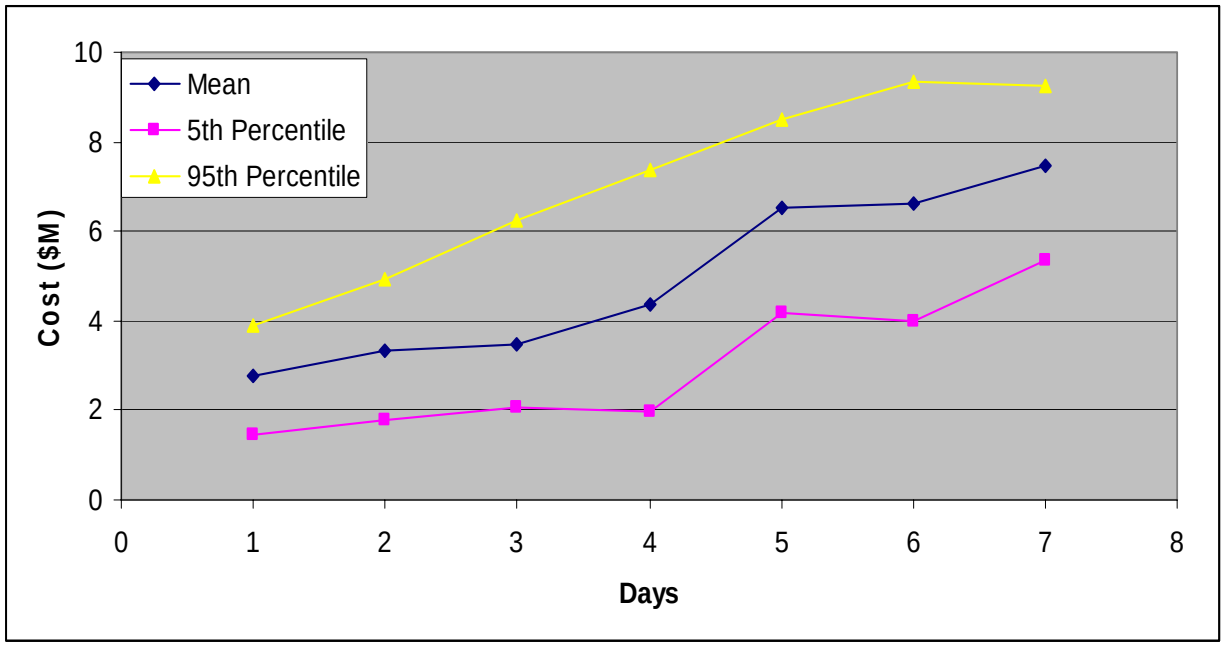

Fig. 32. Cost of lost electricity generation vs days delay in maintenance.

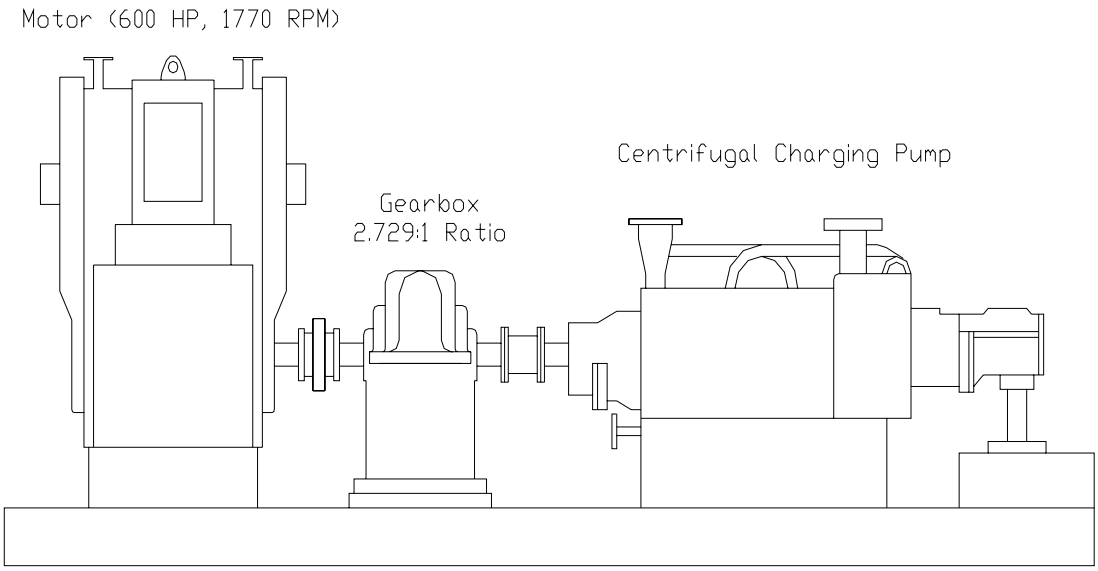

Fig. 33. Typical centrifugal charging pump installation.

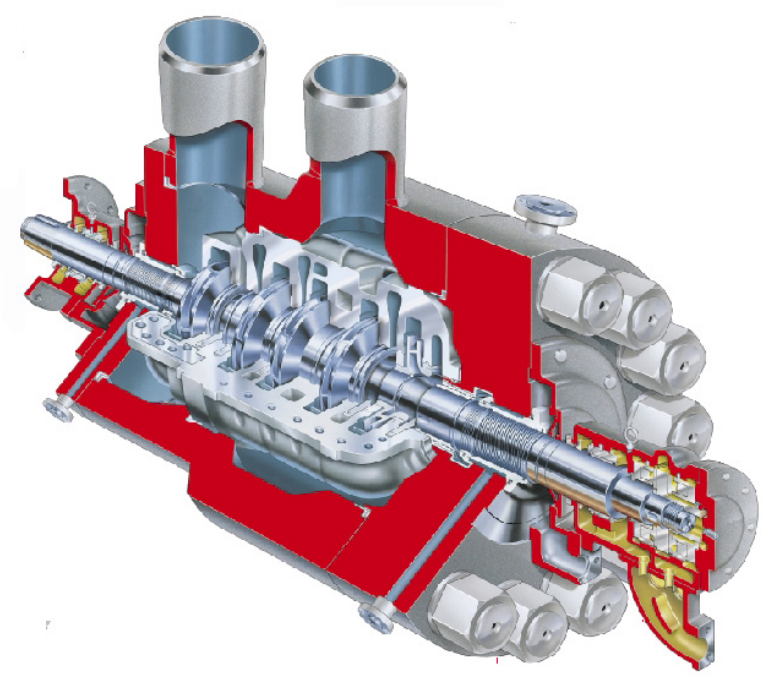

Fig. 34. Basic design of centrifugal charging pump (actual pump: 11 stages).

Fig. 35. Cross-section of cracked shaft.

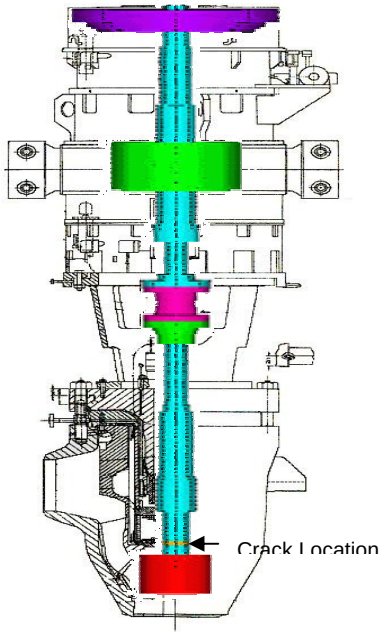

Fig. 36. Reactor coolant pump model with crack location.

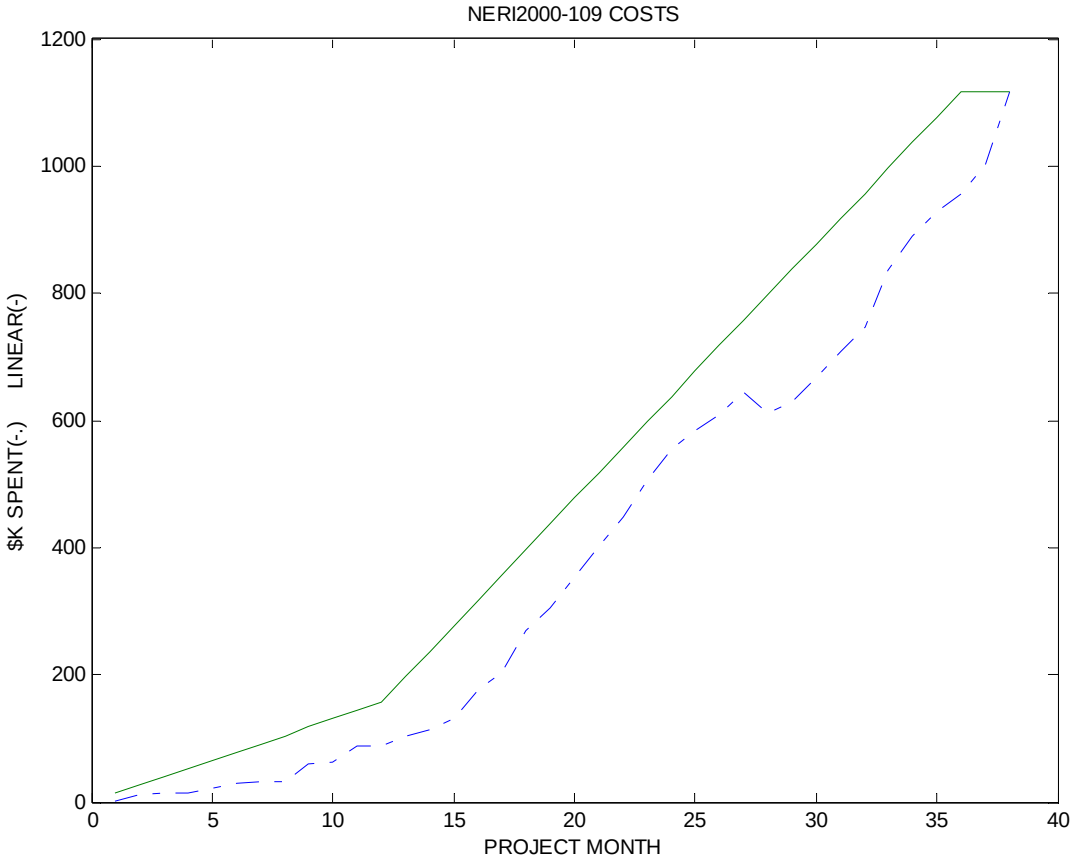

Fig. 37. Cost performance over project life.

APPENDIX A. DESCRIPTION OF TIME-SERIAL ANALYSIS METHODS

A.1 ARTIFACT REMOVAL

Data frequently include artifacts, such as sinusoidal variations in three-phase voltage and current. We remove essentially all of these artifacts with a novel zero-phase quadratic filter.[A.1] This filter uses a moving window of $2w + 1$ points of raw data, e_i, with the same number of data points, w, on either side of a central point. We fit the data to a quadratic equation, $F(t_i) = a_1 T_i^2 + a_2 T_i + a_3$, with $T_i = t_i - t_c$, and t_c as the time at the central point of the moving window. We obtain the best fit to the data by minimizing the function, $\Psi = \Sigma_i [F(t) - e_i]^2$. The sum is over the $2w + 1$ points in the moving window. The minimum in Ψ is found from the condition $\partial\Psi/\partial a_k = 0$, which yields three linear equations in three unknowns. The window-averaged signal is the fitted value at the central point, $F(t_c = t_i) = a_3$. The sums over odd powers of T_i are zero; symmetric sums over even powers of T_i (over i from $-w$ to w) can be converted to sums from 1 to w, giving a window-averaged solution for the artifact signal,

$$F(t = t_c) = \left[3(3w^2 + 3w - 1) \sum_{i=-w}^{w} e_{i+c} - 15 \sum_{i=-w}^{w} i^2 e_{i+c} \right] / (4w^2 + 4w - 3)(2w + 1). \tag{A.1}$$

Sums over even powers of i can be explicitly evaluated with standard formulas for $\Sigma_i i^2$ and $\Sigma_i i^4$ (ref. A.2). The effort to evaluate Eq. (A.1) can be reduced further by computing the sums initially with $c = w + 1$, and then using recursions thereafter for $c > w + 1$ (ref. A.1). Application of this filter to the N-point set of e_i-data yields $N - 2w$ points of artifact data, $f_i = F(t_c = t_i)$. The residue, $x_i = e_i - f_i$, has essentially no artifact. We subsequently use only the artifact-filtered data, x_i.

A.2 CONVENTIONAL STATISTICAL MEASURES

The analysis begins a process-indicative scalar signal, x, typically with unknown dynamical details. The signal is sampled at equal time intervals, $\tau = 1/f_s$, starting at an initial time, t_0, yielding a sequence of N points, $x_i = x(t_0 + i\tau)$. One useful linear measures is the mean, $\underline{x}$, or average over the N data points:

$$\underline{x} = \sum_{i=1}^{N} x_i / N \ . \tag{A.2}$$

The second is the sample standard deviation (σ), which follows from Eq. (A.2):

$$\sigma^2 = \sum_{i=1}^{N} \left(x_i - \underline{x} \right)^2 / \left(N - 1 \right). \tag{A.3}$$

Equation (A.3) is the second moment about the mean. The third moment about the mean is skewness, s:

$$s = \sum_{i=1}^{N} \left(x_i - \underline{x} \right)^3 / N\sigma^3. \tag{A.4}$$

A fourth moment about the mean is kurtosis, k:

$$k = \sum_{i=1}^{N} \left(x_i - \underline{x} \right)^4 / N\sigma^4 - 3. \tag{A.5}$$

Real data have significant values for skewness and kurtosis, while Gaussian random data have values that are not significantly different from zero.[A.3] A large positive (negative) skewness corresponds to a longer, fatter tail of the data distribution about the mean to the right (left). Kurtosis measures the flattening (negative k) or excess peakedness (positive k) about the mean.

Another measure involves counting the number of times, n_c, that the signal crosses the mean. Two sequential mean crossings delimit one-half of a wave period, implying for $n_c >> 1$ that the average number of time steps per wave cycle (m), or equivalently the inverse of the average frequency, is:

$$m = N/[(n_c - 1)/2] = 2N/(n_c - 1) \approx 2N/n_c \,. \tag{A.6}$$

These measures provide little (if any) discrimination of change; we include them only for comparison.

A.3 TRADITIONAL NONLINEAR MEASURES

Various nonlinear measures characterize process dynamics.[A.4,A.5] We discuss three, against which we compare the dissimilarity indicators. Specifically, we use: the first minimum in the mutual information function to measure de-correlation time, the correlation dimension to measure dynamic complexity, and the Kolmogorov entropy to measure of predictability.

The mutual information function (MIF) is a nonlinear version of the (linear) autocorrelation and cross-correlation functions and was originally developed by Shannon and Weaver[A.6] with subsequent application to time series analysis by Fraser and Swinney.[A.7] The MIF measures the average information (in bits) that can be inferred from one measurement about a second measurement and is a function of the time delay between the measurements. Univariate MIF measures predictability within the same data stream at different times. Bivariate MIF measures predictability of one data channel, based on measurements in a second signal at different times. Here, we use the first minimum in the univariate MIF, M_1, giving the average time for x_i to be independent of x_j. System entropy, H, defines MIF, $I(q, r)$:

$$I(q,r) = I(r,q) = H(q) + H(r) - H(r,q)\,, \tag{A.7}$$

$$H(q) = -\sum_i P(q_i)\log[P(q_i)]\,, \tag{A.8}$$

$$H(q,r) = -\sum_{i,j} P(q_i,r_j)\log[P(q_i,r_j)]\,. \tag{A.9}$$

One signal has data, $Q = \{q_1, q_2, \ldots, q_N\}$ with occurrence probabilities $P(q_1)$, $P(q_2)$, . . . , $P(q_N)$. A second signal has data, $R = \{r_1, r_2, \ldots, r_N\}$, having a time delay relative to the q_i values, with occurrence probabilities $P(r_1)$, $P(r_2)$, . . . , $P(r_N)$. The function $P(q_i, r_j)$ is the joint probability of both states occurring simultaneously. H and I are in units of bits if the logarithm is taken in base two.

The maximum-likelihood correlation dimension, D, is:[A.8,A.9]

$$D = \left\{ (-1/M) \sum_{ij} \ln[(\delta_{ij}/\delta_0 - \delta_n/\delta_0)/(1-\delta_n/\delta_0)] \right\}^{-1} \quad , \tag{A.10}$$

where M is the number of randomly sampled point pairs; δ_{ij} is the maximum-norm distance between the (randomly chosen) $i-j$ point pairs, as defined in Eq. (A.12) below. The distance (scale length) δ_n is associated with noise as measured from the time serial data. Note that the distances are normalized with respect to a nominal scale length δ_0, which is chosen as a balance between sensitivity to local dynamics (typically at $\delta_0 \lesssim 5a$) and avoidance of excessive noise (typically at $\delta_0 \geq a$). Here, the symbol a denotes the absolute average deviation as a robust indicator of variability[A.9] in the data,

$$a = (1/N) \sum_{i=1}^{N} |x_i - \underline{x}| \quad , \tag{A.11}$$

where $\underline{x}$ is the mean of x_i over the window of N points. The distances δ_{ij} are defined by

$$\delta_{ij} = \max_{0 \leq k \leq m-1} |x_{i+k} - x_{j+k}| \, , \tag{A.12}$$

where m is the average number of points per cycle, as determined by Eq. (A.6).

Kolmogorov entropy, K, measures the rate of information loss per unit time, or (equivalently) the degree of predictability. Positive, finite entropy is generally considered a clear demonstration that the time series and its underlying dynamics are chaotic. A very large entropy indicates a stochastic (nondeterministic) and therefore totally unpredictable phenomenon. K-entropy is the average time for two points on an attractor to go from an initial separation $\delta \leq \delta_0$ to a separation of more than that distance ($\delta > \delta_0$). We use the maximum-likelihood K-entropy of Schouten et al.[A.10]

$$K = -f_s \log(1 - 1/\underline{b}) \, , \tag{A.13}$$

$$\underline{b} = (1/M) \sum_{i=1}^{M} b_i \, , \tag{A.14}$$

with b_i as the number of time steps for two points, initially within $\delta \leq \delta_0$, to diverge to $\delta > \delta_0$.

Several problems arise in the use of these measures for condition change. The most serious is that these nonlinear measures are expressed as a sum or integral over (a region of) the PS, thus averaging out all dynamical details into a single number. Two (very) different dynamical regimes may lead to very close, or even equal measures. The situation is even murkier for noisy dynamics, in which case reliable determination of the nonlinear measures is very difficult. The second problem originates from the usual definitions of K-entropy and correlation dimension in the limit of zero scale length. However, all real data have noise, and even noiseless model data is limited by the finite precision of computer arithmetic. Thus, we choose a finite scale length that is larger than the noise ($\delta_0 = 2a$), at which to report the values of K and D. These finite-scale values of K and D are smaller than expected for the zero-scale-length limit ($\delta_0 \to 0$) and cannot capture dynamical complexity at length scales smaller than δ_0. A third difficulty is presented by the definition of some nonlinear measures as functionals of the distribution functions, because they do not satisfy the mathematical definition of distance. Specifically, symmetry and the

triangle inequality may be violated.[A.11] Such measures cannot define a metric in the mathematical sense, although they may indicate change that must be made precise for each situation. These traditional nonlinear measures characterize global features of the dynamics, and can clearly distinguish between regular and chaotic dynamics. However, they do not reveal slight dissimilarities between dynamical states. The same is true for other global indicators, such as fractal dimension, and Lyapunov exponents. This lack of discrimination occurs because such traditional measures average (or integrate) the dynamical features over the attractor, thus providing only a global picture of long-term dynamical behavior. The phase-space dissimilarity measures (discussed below) avoid these problems, and thus provide sensitive discrimination of condition change for forewarning of machine failure.

A.4 PHASE-SPACE DISSIMILARITY MEASURES

We begin this analysis by conversion of the continuously variable artifact-filtered signal, x_i, into discrete signal values (symbolization), s_i, which is one of S different integers:

$$0 \le s_i = INT[S(x_i - x_{\min})/(x_{\max} - x_{\min})] \le S - 1 . \tag{A.15}$$

The function (INT) converts a decimal number to the closest lower integer, and x_{min} and x_{max} denote the minimum and maximum values of x_i, respectively, over the base case (reference data). We require that $s_i(x_i = x_{max}) = S - 1$ in order to maintain exactly S distinct symbols. Thus, Eq. (A.15) creates symbols that are uniformly distributed between the minimum and maximum in signal amplitude (uniform symbols).

An alternative is equiprobable symbols. These symbols are formed by ordering the base case time-serial data from the smallest to largest value. The first N/S of these ordered data values correspond to the first symbol (0). Ordered data values $(N/S) + 1$ through $2N/S$ correspond to the second symbol (1), and so on up to the last symbol, S-1. Consequently, equiprobable symbols have non-uniform partitions in the signal amplitude so that each symbol has the same occurrence frequency (N/S) of x_i values. Much structure is inherent in uniform symbols before beginning the PS reconstruction, but no PS structure arises from equiprobable symbols. Thus, a key advantage of equiprobable symbols is that dynamical structure arises only from the phase-space reconstruction, as described below. Large negative and large positive values of x_i have little effect on equiprobable symbolization, but dramatically change the partitions for uniform symbols. Moreover, information theoretic measures (e.g., mutual information function) are a smooth function of the reconstruction parameters for equiprobable symbols, but are noisy functions for uniform symbols. We find that equiprobable symbols discriminate condition change better than uniform symbols.

PS reconstruction[A.12] converts time-serial s_i-data into a geometric form via the use of time-delay vectors to unfold the underlying dynamics. The single-channel reconstruction form is:

$$y(i) = [s_i, s_{i+\lambda}, \ldots, s_{i+(d-1)\lambda}]. \tag{A.16}$$

Local (single-channel) processes exchange dynamical information with one another. For example, the components of three-phase voltages and currents are dynamically related by electrical interactions. Likewise, the components of three-dimensional acceleration depend

nonlinearly on one another through mechanical interactions. This nonlinear inter-relation implies that multi-channel PS reconstruction can extract additional information.[A.13] The multi-channel PS vector has the form:

$$y(i) = [s(1)_i, s(1)_{i+\lambda}, \ldots, s(1)_{i+(d-1)\lambda}, \ldots, s(C)_i, s(C)_{i+\lambda}, \ldots, s(C)_{i+(d-1)\lambda}]. \quad \text{(A.17)}$$

Here, $s(1)$ denotes symbols from the first data channel, and $s(C)$ denotes symbols from the Cth channel. The PS reconstruction unfolds the underlying dynamics to extract event forewarning on the basis of the time delay, λ, dimensionality, d, and signal precision, S. If the dimension, d, is too large, then over-fitting can result. Moreover, different process observables contain unequal amounts of dynamical information. [A.14] Thus, PS reconstruction may be easier from one variable, but more difficult or even impossible from another. Our analysis seeks to balance these caveats for finite-length noisy data.

Symbolization discretizes the PS into S^d bins. We then count the number of PS points occurring in each bin to obtain the distribution function (DF) as a discretized density on the attractor. We denote the population of the ith bin of the distribution function, Q_i, for the base case (nominal operational state), and R_i for a test case (subsequent operational state), respectively. The parameters (w, S, N, d, λ) depend on the specific data. Preliminary analysis systematically varies each parameter with the others fixed, to obtain optimum sensitivity of the measures to process changes for each test sequence. We subsequently search in the vicinity of this optimally-sensitive location for improved discrimination of change.

Quantification of condition change requires comparison of the test case to the base case. In particular, we measure the dissimilarity between Q_i with R_i by the χ^2 statistic and L_1 distance:

$$\chi^2 = \sum_i (Q_i - R_i)^2 / (Q_i + R_i), \quad \text{(A.18)}$$

$$L = \sum_i |Q_i - R_i|, \quad \text{(A.19)}$$

where the summations in both equations run over all of the populated PS cells. The choice of these measures is based on the following considerations. The χ^2 statistic is one of the most powerful, robust, and widely used tests to measure discrepancies between two distribution functions. The χ^2 statistic is obviously symmetric, but does not always satisfy the triangle inequality. Thus, it does not define a distance in the mathematical sense. The L_1 distance is the natural metric for distribution functions by its direct relation to the total invariant measure on the attractor and does define a mathematical distance. These complementary measures account for changes in the geometry and visitation frequency of the attractor. Consistent calculation of χ^2 and L requires that the base case and test case contain the same number of points, identically sampled; otherwise the distribution functions have to be properly rescaled.

We can capture process flow[A.15] by adjoining two successive d-dimensional PS vectors, as prescribed by the dynamics, $y(i) \rightarrow y(i+1)$. The result is a connected-phase-space (CPS) vector:

$$Y(i) = [y(i), y(i+1)] \quad \text{(A.20)}$$

Symbolization of the x_i-data discretizes this 2D CPS into S^{2d} bins. As before, we count the number of CPS points occurring in each bin to obtain Q and R, which are the CPS DFs for the base case and test case, respectively. The dissimilarity measures are the L_1-distance and χ^2 statistic:

$$x_c^{\,2} = \sum_{ij} \left(Q_{ij} - R_{ij}\right)^2 / \left(Q_{ij} + R_{ij}\right) \tag{A.21}$$

$$L_c = \sum_{ij} | Q_{ij} - R_{ij} | . \tag{A.22}$$

The subscript c indicates the connected distribution function measure. The CPS measures have higher discriminating power than their non-connected counterparts, because they satisfy the following four inequalities: $\chi^2 \le L$, $\chi_c^{\,2} \le L_c$, $L \le L_c$, and $\chi^2 \le \chi_c^{\,2}$. Alternative forms are: $\chi^2 \le L \le L_c$ and $\chi^2 \le \chi_c^{\,2} \le L_c$.

Unbiased determination of the χ^2 statistic requires statistical independence between various samples. However, the (C)PS points depend on one another due to reconstruction from time delay vectors with dynamical structure.[A.16] The resulting statistical bias is avoidable by averaging contributions to Eqs. (A.18)−(A.22) over values of y(j) or Y(j) which satisfy $|i - j| < \Lambda$ (ref. A.16), where Λ is some largest typical correlation time lag. We tested the bias in typical data by sampling every Λ-th connected phase space point for $4 \le \Lambda \le 23$, resulting in Λ different samples for the base case (Q_i) and for each cutset (R_i). We then averaged the sampled χ^2 values over the Λ^2 different combinations of distribution functions for the base case and test case cutsets. As expected, a decrease proportional to $1/\Lambda$ occurs in the sampled χ^2 values, because the number of data points contributing to χ^2 decreases in the same proportion. The trend over time in sampled χ^2 values is the same as in χ^2 values without sampling, showing that no bias is present. Thus, we use unsampled χ^2 values for the remainder of this work as a relative measure, rather than as an unbiased statistic for accepting or rejecting a null statistical hypothesis.[A.17]

Use of the dissimilarity measures on finite length, noisy data requires a consistent statistical implementation and interpretation. We use the first B non-overlapping cutsets as base cases. The choice of this number of basecase datasets should strike a judicious balance between a reasonably short base case period to capture quasi-stationary, "normal" dynamics and a sufficiently long period for statistical significance. We typically use $B = 5$ for the noiseless, model generated data for fixed dynamical conditions, where the variability arises only from the location in and the discrete sampling of the PS. On the other hand, we use $B = 10$ for noisy machine data to provide a larger statistical sample.

The disparate range and variability of various nonlinear measures are difficult to interpret (especially for noisy data), so we need a consistent means of comparison. Thus, we renormalize the nonlinear measures.[A.17,A18] For each nonlinear measure, $V = \{D, K, M_1, L, L_c, \chi^2, \text{and } \chi_c^{\,2}\}$, we define V_i as the value of the nonlinear measure for the ith cutset. $\overline{V}$ is the mean value of the nonlinear measure over the base cases, with a corresponding sample standard deviation σ. The renormalized form is then $U(V) = |V_i - \overline{V}|/\sigma$, which measures the number of standard deviations that the test case deviates from the base case mean. Several successive occurrences, N_{OCC}, above a threshold, U_{th}, provide a clear indication of condition change. Alternatively, a systematic rise

in the phase-space dissimilarity measures will indicate a clear departure from the base case dynamics, and provides forewarning of failure.

The methodology and corresponding results have been published in recent peer-reviewed journal papers.[A.17,A18,A19,A20,A21,A.22] The strength of the approach is accurate and robust event forewarning from complex, nonlinear time-serial data. A weakness of the method is the need for much, high-quality, process-indicative data for the analysis.

The nonlinear analysis in this Appendix is implemented as research-class FORTRAN-77. This software was developed and used on a variety of different computers and operating systems since 1994: IBM RISC/6000 under IBM's version of UNIX, DEC-alpha under DEC's version of UNIX, Intel-PII under Windows NT and Windows 2000, and AMD-Athlon™ and Intel Pentium-4™ under Windows2000™ and Windows-XP™. The software required little or no change to move from one computer and/or operating system to the next. The program executable size is typically 5–55 MB. The dataset sizes have a typical range of 100 MB to 1.5 GB, necessitating a correspondingly large, fast harddrive for data storage. No user guide or manual exists for this software, due to its ongoing evolution for research-class analysis.

REFERENCES FOR APPENDIX A

A. 1. L. M. Hively, N. E. Clapp, C. S. Daw, and W. F. Lawkins, "Nonlinear analysis of EEG for epileptic events," *ORNL/TM-12961* (Oak Ridge National Laboratory, Oak Ridge, TN, 1995).

A. 2. I. S. Gradshteyn and I. M. Ryzhik, Tables of Integrals, Series, and Products, Academic Press publ., New York (4th ed., 1965).

A. 3. M. Abramowitz and I. A. Stegun (ed.), Handbook of Mathematical Functions, U. S. Government Printing Office, Washington, D.C. (1965), page 930.

A. 4. H. Kantz and T. Schreiber, Nonlinear Time Series Analysis, (Cambridge University Press) 1997.

A. 5. A. Rezek and S. J. Roberts, "Stochastic Complexity Measures for Physiological Signal Analysis," *IEEE Trans. Biomedical Eng.* **45** (1998) 1186−1191.

A. 6. C. E. Shannon and W. Weaver, The Mathematical Theory of Communication (Univ. of Illinois Press, Urbana) 1949.

A. 7. A. M. Fraser and H. L. Swinney, "Independent coordinates for strange attractors from mutual information." *Phys. Rev. A* **33** (1986) 1134−40.

A. 8. F. Takens, "On the numerical determination of the dimension of an attractor," *Lecture Notes in Mathematics* **1125** (1984) 99–106 (Springer publ., Berlin).

A. 9. J. C. Schouten, F. Takens, and C. M. van den Bleek, "Estimation of the dimension of a noisy attractor," *Phys. Rev. E* **50** (1994a) 1851−1861.

A. 10. J. C. Schouten, F. Takens, and C. M. van den Bleek, "Maximum likelihood estimation of the entropy of an attractor," *Phys. Rev. E* **49** (1994b) 126−129.

A. 11. R. Q. Quiroga, J. Arnhold, K. Lehnertz, P. Grassberger, "Kuhlback-Leibler and renormalized entropies: Applications to electroencephalograms of epilepsy patients," *Phys. Rev. E.* **62** (2000) 8380−8386.

A. 12. J. P. Eckmann and D. Ruelle, "Ergodic theory of chaos and strange attractors," *Rev. Mod. Phys*. **57** (1985) 617−55.

A. 13. S. Boccaletti, *et al.*, "Reconstructing embedding spaces of coupled dynamical systems from multivariate data," *Phys. Rev. E* (2002) 035204.

A. 14. C. Letellier, J. Maquet, L. Le Sceller, G. Gouesbet, L. A. Aguirre, "On the non-equivalence of observables in phase-space reconstructions from recorded time series," *J.Phys.A* **31** (1998) 7913−7927.

A. 15. H. D. I. Abarbanel, Analysis of Observed Chaotic Data (Springer pub., New York) 1996.

A. 16. C. Diks, W. van Zwet, F. Takens, and J. DeGoede, "Detecting differences between delay vector distributions," *Phys. Rev. E* **53** (1996) 2169−76.

A. 17. L. M. Hively, P. C. Gailey, and V. A. Protopopescu, "Detecting dynamical change in nonlinear series time series," *Phys. Lett. A* **258** (1999) 103−114.

A. 18. L. M. Hively, P. C. Gailey, and V. A. Protopopescu, "Sensitive Measures of Condition Change in EEG Data," in Proc. International Workshop: ''Chaos in Brain?,'' (Bonn, Germany, 10–12 March, 1999), ed. K. Lehnertz et al. (World Scientific, Singapore, 2000), p. 333−336.

A. 19. L. M. Hively, V. A. Protopopescu, and P. C. Gailey, "Timely detection of dynamical change in scalp EEG signals," *Chaos* **10** (2000a) 864-875.

A. 20. V. A. Protopopescu, L. M. Hively, and P. C. Gailey, "Epileptic Event Forewarning From Scalp EEG," *J. Clinical Neurophysiol.* **18** (May 2001) 223−245.

A. 21. L. M. Hively and V. A. Protopopescu, "Detection of Changing Dynamics in Physiological Time Series," *Proc. Nuclear Mathematical and Computational Sciences: A Century Anew* (publ Amer. Nucl. Soc., LaGrange, IL) 2003.

A. 22. L. M. Hively and V. A. Protopopescu, "Channel-Consistent Forewarning of Epileptic Events from Scalp EEG," *IEEE Trans. Biomed. Engr.* **50** (2003a) 584−593.

APPENDIX B. STATEMENT OF WORK FOR SUBCONTRACT WITH PSU/ARL

The U.S Department of Energy has funded an ORNL project, "Forewarning of Failure in Critical Equipment at Next-Generation Nuclear Power Plants." The goal is forewarning of failure via ORNL's nonlinear technology, using experimental data from typical equipment. We seek forewarning for different kinds of equipment, as well as consistency for the same fault(s) in the same equipment. The Applied Research Laboratory (ARL) is a center of excellence at the Pennsylvania State University. ARL provided ORNL with machinery failure data in support of this NERI2000-109 project during FY02. This statement of work describes three follow-on tasks under this same NERI project for FY03. The total cost of these three tasks will be no more than $100K.

Task No. 1 involves documentation of the test plans that will become appendices in the FY03 annual NERI report. The test plan(s) will specify the equipment to be tested (as in Sect. A.5 of App. A of the PY1 annual report), the test protocol for each failure mode (as in Sect. A.6.5 of App. A), and the data acquisition (as in Sect. A.7 of App. A). The deliverables are the test plans for each test sequence, which will be sent to ORNL before the start of testing. Table B1 summarizes the test apparatus, test parameters, and a general description of the test procedure for each experiment.

Task No. 2 will proceed immediately after completion of the applicable test plan from Task 1. This task involves ARL setting up and conducting a series of tests on mechanical and electrical equipment, as shown in Table B2, according to the test plan(s) from Task 1. The time-serial data for each test will be appropriate for the equipment and failure type (e.g., three-phase motor currents and voltages; tri-axial acceleration; torque and angular location; pressure and flow rate, etc.). The data for each snapshot in the test sequence should be sampled at no less than 50 kHz for 10 s (for a total of 500,000 data points). The goal of this task is acquisition of test sequences (TS), which refer to a unique combination of equipment and failure mode. Each TS will show the equipment initially in nominal operation, then with a small fault, and subsequently with successively larger faults until the equipment fails per test plan. The deliverables are the multi-channel digital datasets from each test sequence, provided on CD-ROM or DVD diskette, as appropriate. Table B2 shows an approximate schedule for completion of Task 2 testing.

Task No. 3 will proceed during and after completion of Task 2. This task involves assessment of the ORNL forewarning technology, in terms of safety and cost impact for next generation nuclear power plants. The assessment metrics include forewarning time, decrease in unexpected failures, increased safety margins, and lower costs for operations and maintenance. ARL will draw on internal resources, knowledge of the nuclear power industry, results from past cost-benefit analyses for other condition monitoring applications, and existing reports by other organizations such as EPRI. The deliverable for this task will be documentation of the assessment methodology and results, in a form that is suitable for inclusion as an appendix in the FY03 NERI annual report. The delivery date is close-of-business Thursday July 31, 2003.

Table B. 1. Summary of Test Sequences

Fault	Experiment Parameters	Procedure
Gear	Gear ratio, torque, speed	Run gearbox at constant speed with nominal load for break-in period, then increase load to 2X or 3X gearbox rating until gear failure
Cracked shaft	Crack depth	Collect baseline data (speed, 3-axis vibration, motor V&A) with undamaged shaft. Initiate shaft crack using EDM cut. Collect data. Grow crack using lateral bending fatigue apparatus. Repeat data collection. Goal is to collect 10−20 iterations of crack growth per experiment.
Generator – Field (rotor) deterioration	Load, location of winding deterioration, leakage current	Collect baseline data at each load condition (load conditions are dependent on available load resistors – TBD). Collect data for a series of increasing leakage currents. Data collection will include 3-axis vibration, line voltages and currents, exciter field current, and generator field current.
Generator – Stator deterioration	Load, location of winding deterioration, leakage current	Collect baseline data at each load condition (load conditions are dependent on available load resistors – TBD). Collect data for a series of increasing leakage currents. Data collection will include 3-axis vibration, line voltages and currents, exciter field current, and generator field current.
Generator – Diode deterioration	Load, polarity of diode, leakage current	Collect baseline data at each load condition (load conditions are dependent on available load resistors – TBD). Collect data for a series of increasing leakage currents. Data collection will include 3-axis vibration, line voltages and currents, exciter field current, and generator field current.

Table B.2. Anticipated Test Schedule

Test	Duration	Target Test Dates
MDTB	3 weeks ea.	
gearbox 1		January 2003
gearbox 2		March 2003
Shaft Crack	1 month ea.	
Shaft 1		November 2002
Shaft 2		December 2002
Electrical Gen.	2 weeks ea.	
Rotor fault		February 2003
Stator fault		April 2003
Diode fault		May 2003

APPENDIX C. TEST PLAN FOR MECHANICAL DIAGNOSTICS TEST BED IN SUPPORT OF NERI2000-109

This document is the test plan for the Mechanical Diagnostics Test Bed (MDTB) at the Applied Research Laboratory (ARL) of the Pennsylvania State University (PSU). This plan describes the MDTB, the equipment to be tested, instrumentation and data acquisition equipment, and the test sequence protocol. This work is funded by Oak Ridge National Laboratory (ORNL) under the U.S. Department of Energy's NERI2000-109 (Nuclear Energy Research Initiative) project.

C.1 TEST BED

Figure C.1 shows the MDTB, which is an ARL facility for the study of fault evolution in gearboxes. The alternating-current (AC) driver motor is rated at 30 HP and runs at a constant speed. The AC (absorption) motor is rated at 75 HP and applies a mechanical load (torque) to the gearbox. The maximum speed and torque are 3500 RPM and 225 ft/lbs, respectively. Speed is controlled by variation of the frequency to the driver motor with a digital vector unit. Torque is controlled by a similar vector unit to the absorption motor. The vector drives also provide output signals, which are sampled and stored. The set points for speed and torque are determined by

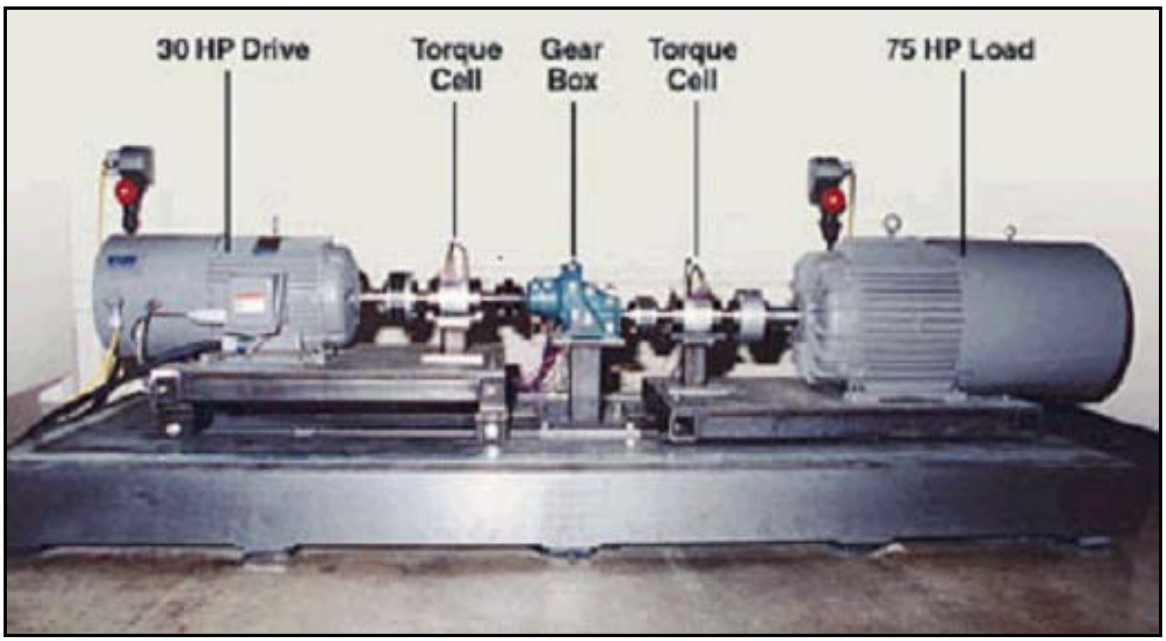

Fig. C.1. Mechanical diagnostics test bed.

analog signals (0-10 VDC) from the data acquisition computer. The MDTB is capable of parallel or right angle gear motor mounts.

The MDTB has the capability of testing single- and double-reduction industrial gearboxes with gear ratios between 1.2:1 to 6:1, and with power in the range of 5 to 20 HP. Duty cycle profiles can be prescribed for variable speed and load. Test speeds to date have been fixed at 1750 RPM with variable load profiles that increase to maximum values of 2 to 5 times the rated torque of the test gearbox. The motors and gearbox are hard-mounted to minimize vibration, and are precision aligned via laser technology. The shafts can be connected with either flexible or rigid

couplers. Torque limiting clutches are used on both sides of the gearbox to avoid excessive torque from gear jamming or bearing seizure. Torque cells on both sides of the gearbox monitor the overall and variable loads. Output data include: input power to the motors, root-mean-square (RMS) currents, winding temperatures, motor speed, and generator torque. These signals allow automation and shutdown of motors directly through the controller PC.

C.2 EQUIPMENT TO BE TESTED

These tests also will use the MDTB to collect run-to-failure data on single-reduction gearboxes during the fault evolution cycle. Table C.1 shows the characteristics of the gearbox that will be used for the two tests. Tables C.2 and C.3 show the gear mesh and bearing frequencies.

Table C.1. Gearbox Specifications

Brand	**Dodge (R86001)**
Model Number	APG Size 3
Description	Single Reduction Helical
Ratio	1.5
Rated Input Speed	1750 RPM
Rated Output Torque	530 in./lbs
Potential Failure	Gear tooth breakage

Table C.2. Dodge Gearbox Bearing Input and Output Frequencies (1.5 Gearbox Ratio)

Description	Ball Bearing (Input - outer)	Ball Bearing (Input - inner)	Tapered Roller Bearing (Output - inner)	Taper Roller Bearing (Output - outer)
Part Number	**6307**	**6309**	**15520/15578**	**2520/2581**
Inner Race Freq	29 Hz	29 Hz	19 Hz	19 Hz
BPFO	86 Hz	89 Hz	178 Hz	176 Hz
BPFI	147 Hz	145 Hz	133 Hz	135 Hz
FTF	11 Hz	11 Hz	11 Hz	11 Hz
BSF	52 Hz	57 Hz	54 Hz	61 Hz

Table C.3. Dodge Gearbox Gear Mesh Frequency (at 1750 RPM)

Gearbox Size 3 – Ratio 1.5	875.5 Hz
Gearbox Size 3 – Ratio 3.3	613.0 Hz

C.3 INSTRUMENTATION AND DATA ACQUISITION EQUIPMENT

Data is collected via a National Instruments (NI) PXI measurement system. Figure C.2 shows a typical system, including backplane, processor, control module, and data acquisition modules. These tests will use NI4472 dynamic signal acquisition and analysis modules (Fig. C.3). Each module has eight analog inputs with simultaneously-sampled, 24-bit, sigma-delta analog-to-

digital (A/D) converters. Table C.4 gives module operating characteristics, including the digital anti-aliasing filters. The maximum sampling rate is 102.4 kHz per channel. We will sample at 51.2 kHz for an alias-free bandwidth up to 23.2 kHz. The accelerometer resonance is >70 kHz, which will not interfere with the measurement bandwidth.

The following data will be collected: (a) 3-axis acceleration, via 3 single-axis accelerometers on a gearbox mounting block; (b) input and output torque; and (c) input and output tachometer signal. Data will be sampled across all channels, and saved to a computer hard drive. Table C.5 gives the specifications for the single-axial accelerometer. Additional sensor measurements may be added on open data acquisition channels for consistency with earlier gearbox tests. The full sensor list will be provided in the post-run test description along with a drawing showing sensor placement.

Fig. C.2. NI PXI measurement system.

Fig. C.3. NI dynamic DAC module.

Table C.4. DAQ Module Specifications

Channels per module	8
A/D resolution	24 bits
Dynamic range	120 dB
Measurement bandwidth	DC-45 kHz
Coupling	AC/DC
Alias-free bandwidth: pass-band	DC to 0.4535 f_s
Stop Band	0.5465 f_s
Alias rejection	110 dB

Table C.5. Accelerometer Specifications

Sensor Name	ICP Accelerometer
Sensor Make	PCB Piezotronics, Inc
Sensor Model #	353B16
Sensor Serial #	TBD
Sensor Type	Quartz Shear Piezoelectric
Sensor Volt Sensitivity	10 mV/g
Measurement Range	±500 g pk (± m/s2 pk)
Frequency Range (±5%)	1 to 10 000 Hz
Mounted Resonant Frequency	> or = 70 kHz
Broadband Resolution	0.005 g rms (0,05 m/s2 pk)
Conditioner Make	PCB Piezotronics, Inc.
Conditioner Model #	481A02
Conditioner Gain	1

C.4 DATA FORMAT

Data will be in MatLab™ binary format. Matlab™ m-files also will be provided to read the information from the files. Data will be delivered to ORNL on either CDR or DVDR media. We expect that the total size (T) for a one, 10-s snapshot containing 11 sensor channels is estimated as follows: T = (10 s) × (51.2 k samples/s) × (4 bytes/sample/channel) × (11 channels) = 22.5 MB. Alternatively, storage of each channel as a separate file will yield a 2 MB file per channel per snapshot.

C.5 TEST PROTOCOL

The test procedure is summarized below:

1. Disassemble gearbox and drain out the lubrication oil;
2. Index the gear if possible;
3. Place identification labels on each gear tooth;
4. Assemble the gearbox and refill with manufacturer-specified gear oil;
5. Mount the gearbox to the test stand and perform a laser alignment;
6. Attach all sensors to the gearbox and set up data acquisition system;
7. Calibrate all sensors and save results with time stamps;
8. Run the test matrix until failure;
9. Perform a post-test laser alignment before gearbox removal;
10. Disassemble and inspect the gearbox for characterization of the failure.

Table C.6 shows the test matrix, including the intended test conditions. Data will be collected until failure of the gearbox or until the damage to the gearbox threatens to induce damage in other system components.

Table C.6: Test Matrix

Test Condition	Speed (RPM)	Torque	Duration	Snapshot Rate
1	1750	100% of rated (530 in./lbs)	1 h	1 snapshot/min
2a (Run No.36)	1750	200% of rated (1060 in./lbs)	Until failure	1 snapshot/15 min
2b (Runs No.37−38)	1750	300% of rated (1590 in./lbs)	Until failure	1 snapshot/min

Appendix D. TEST PLAN FOR SHAFT-CRACK EXPERIMENT

Title: Seeded Crack Fault Test of Laboratory Bladed Disk Assembly

Personnel: Brian Resor, Martin Trethewey, Ken Maynard

Test Description

One failure mode in a turbo-machine begins with a crack at the base of a rotating blade, eventually causing blade loss. This Appendix describes an experiment to simulate such a failure. PSU conducted the experiment on the Torsional Vibration Test Rig during 2003. Figure D.1 shows the test rig. The objective was detection of dynamical changes with increasing crack size, thus simulating the change in dynamical frequencies due to crack initiation and growth.

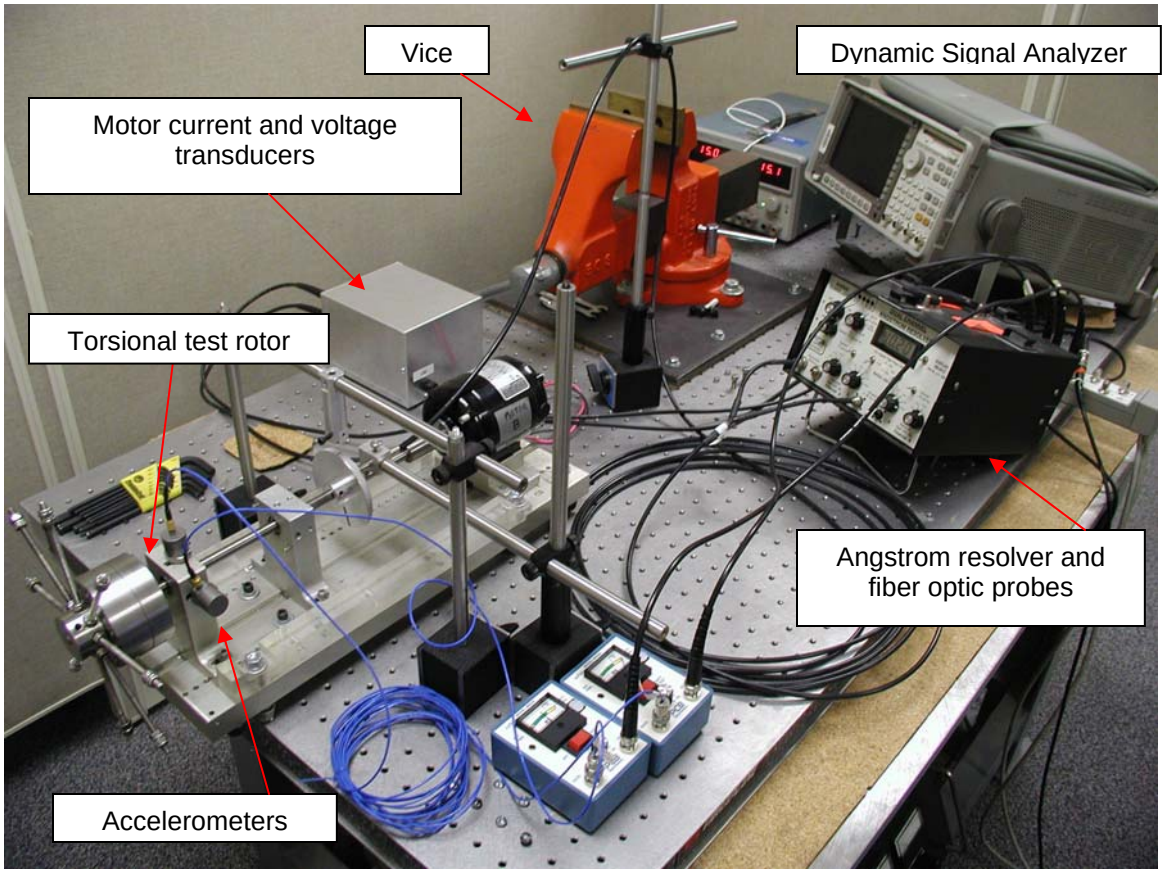

Figure D.1. Motor testing equipment setup

Figure D.2 shows the rotor assembly, which has eight equally spaced threaded rods that simulate the blades. The rotor is driven at a fixed rotational speed by a fractional horsepower DC motor that was made by Bodine Electric Company; this particular motor is no longer manufactured. Typical values for the motor power supply are 4 Volts and 2 Amps, depending on the rotor load. The DC power supply is by Sorenson Power Supplies, a Raytheon Company (part number DCR150-12B).

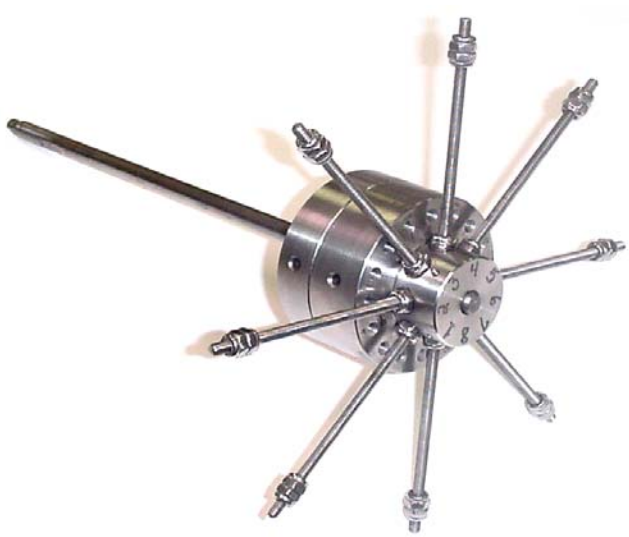

Figure D.2. Simulated bladed disk assembly

Earlier PSU work simulated the crack growth by changing the lock-nut locations along the threaded rods. The present experiment is an extension of earlier PSU work, involving a sequence of tests with a progressively deeper machined "crack" to change the rod frequencies, instead of moving the lock nuts. Figure D.3 shows a typical "crack" at the base of one of the eight blades of the rotor. Wire electric discharge machining (EDM) cutting is used to produce the smallest possible cut to simulate a crack. The wire diameter for these cuts is 0.010 inches and the over burn is approximately 0.001 inches. This adds up to a total cut width of 0.012 inches. The cut depth can be controlled to within about 0.0005 inches. We anticipate ten datasets, beginning with the nominal (no cut) state and ending with a crack depth of 70% of the blade diameter. The cut location is as close to the blade root as was practical. A fixture was created for Wire EDM machine, in which the whole bladed assembly (excluding shaft) is mounted. Computerized tooling controls the cut location and depth for each cut. The depth of the first cut was measured from the point that the 0.010 inch wire came in contact with thread surfaces at the deepest point of the thread.

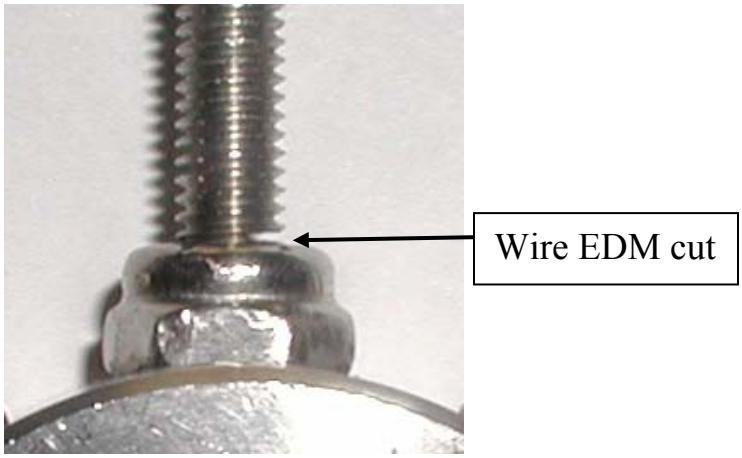

Figure D.3. Picture of blade cut

Test Protocol

The test protocol is as follows:

1. Acquire test data (items 3-5, below) for the no-cut (nominal) state of the rotor assembly.
2. Place an initial 0.010-inch cut in one rod and measure its depth.
3. Measure the bending natural frequency of the seeded fault rod.
4. Place the rotor assembly in the torsional vibration test stand.
5. Run the test stand at fixed RPM and acquire the time-serial data from the system sensors.
6. Remove the rotor assembly and increment the slot depth another 0.010 inch by EDM.
7. Repeat steps 2 and 6 until a "failed" state is achieved (after nine successive EDM cuts).

The vice in Fig. D.1 is used to hold the rotor assembly, while the "blade" static frequency is measured by placing the tip of the fiber optic probes very close to the end of the blade and plucking the blade. The probes measure the blade position versus time, which is analyzed in the DSA to determine the blade frequencies. Nominal disassembly-reassembly repeatability is about ± 0.3 Hz. Due the presence of occasional outliers, multiple disassembly-reassembly test runs will be performed. The data will be analyzed and the reassembly tests ceased only when it is concluded that a representative set of data has been acquired.

Deliverables for this experiment include:

1. Data for each of the seven tests of the rotor (one nominal state, plus six cuts).
2. Experimental characterization of each test state.

Data Acquisition

Test data at each depth of cut include tri-axial acceleration in three orthogonal directions on one bearing pillow block. Torsional vibration data also will be acquired at 1.675 MHz via a fiber optic sensor and a 180-tooth encoder wheel. Figure D.1 shows the data sensors. The data acquisition system uses a Hewlett Packard VXI Mainframe with an E1433A 8-channel data acquisition board with tachometer inputs. Data is sent from the VXI Mainframe to a desktop PC using the HP E8491A firewire card. The desktop PC uses a software package called HP DAQ Express to manage the data acquisition. Using this software along with the E1433 card, data are acquired at 196 kHz sample rate for a duration of 5.10204 seconds, yielding one million data points per snapshot.

Test Data

PSU will provide test data in MatLab™-formatted MAT-files for each wire EDM cut of the blade. Each data record will include: (channel 1) time stamp from the start of the snapshot (seconds), (channels 2-4) tri-axial acceleration (g), and (channel 5) rotational position (degrees). If other measurement units are used, conversion factors will be supplied, along with the appropriate offset and scaling factors. Data will be sent to ORNL on CD-ROM or DVD media, via Federal Express™ or equivalent one-day-delivery service.

APPENDIX E. TEST PLAN FOR GENERATOR SEEDED FAULTS

This appendix describes three types of seeded electrical faults in a 3-phase electrical generator, which is driven by an electric motor. The generator is a Kato Engineering, Model A267890000, (5 kW, 3-phase, 60 Hz, synchronous alternating current). The drive motor is a Kato Engineering, Model D267880000 (7.5 HP, synchronous, brushless, direct current). The three faults conditions are: (1) rotor turn-to-turn short circuit, (2) rectifier diode fault, and (3) stator turn-to-turn short circuit. The test procedure for each fault type is described in the subsequent paragraphs.

Data are collected for each type of fault at different severity levels and under different load conditions. All loads are purely resistive, corresponding to different output powers between zero to 3,600 watts in increments of 1,200 watts. Data are collected using the National Instruments PXI data acquisition system, which also is used to collect data from the MDTB experiment (App. B). Table E.1 lists the data for each test condition. Table E.2 shows the sensor details for current, voltage, and acceleration.

Table E.1. Data Channels For Generator Fault Tests

File ext.	Sample Rate	Data Type	Description
IA	52 kHz	Current	Phase A line current
IB	52 kHz	Current	Phase B line current
IC	52 kHz	Current	Phase C line current
VAB	52 kHz	Voltage	Phase AB line voltage
VBC	52 kHz	Voltage	Phase BC line voltage
VCA	52 kHz	Voltage	Phase CA line voltage
A01	52 kHz	Acceleration	x-axis acceleration
A02	52 kHz	Acceleration	y-axis acceleration
A03	52 kHz	Acceleration	z-axis acceleration
VAN	52 kHz	Voltage	Phase A line-to-neutral voltage
VBN	52 kHz	Voltage	Phase B line-to-neutral voltage
VCN	52 kHz	Voltage	Phase C line-to-neutral voltage
IEXC	52 kHz	Current	Exciter current
VNG	52 kHz	Voltage	Neutral-to-ground voltage

Table E.2. Generator Seeded-Fault Sensors

Data Type	Transducer
Current	AYA model CT8-50-1 Current Transformer with 1/2 ohm, 1 watt, 1% sense resistor
Voltage	LEM CV3-500 voltage transducer, 50:1 voltage reduction with +/- 15 V supply
Acceleration	PCB Piezotronics, Inc Model 353B16 ICP 3-axis Accelerometer

Data file names correspond to the snapshot number, followed by the file extension for the corresponding fault. For example, 0.A01 corresponds to the zeroeth (0) snapshot (baseline data) for acceleration data (A) in the first (01) direction; 1.A01 is for the first fault snapshot for

acceleration (A) in the first (01) direction, etc. Testing begins with the acquisition of baseline (no fault) conditions for each load level, as shown in Table E.3.

The rotor fault test uses one large connector wire (8 or 10 gauge) from Terminal 1 to Terminals 2−6 on the generator, corresponding to shorting out a specified number of turns on pole number three of the generator, as shown in Table E.4. Use of Terminals 7–9 is unnecessary, because the readings are too low, too high, or non-existent in these cases. Rotor test conditions are listed in Table E.4.

Table E.3. Snapshot Numbers For No Fault Baseline Tests

Load (W)	Snapshot
0	0,1
1200	2,3
2400	4,5
3600	6,7
0	8,9

Table E.4. Snapshot Numbers For Rotor Fault Tests

Load (W)	Rotor Fault Condition				
	T1-2 5 Turns	T1-3 10 Turns	T1-4 25 Turns	T1-5 50 Turns	T1-6 100 Turns
0	10,11	20,21	30,31	40,41	50,51
1200	12,13	22,23	32,33	42,43	52,53
2400	14,15	24,25	34,35	44,45	54,55
3600	16,17	26,27	36,37	46,47	56,57
0	18,19	28,29	38,39	48,49	58,59

Three types of diode faults were simulated. The first fault uses one 3-ohm 100-watt resistor to create a short circuit across the positive diode. The load is attached to generator set. The leakage current is about 1 ampere. The second diode fault disconnects the diode creating an open circuit. The third fault uses a variable resistor in series with the diode to create different levels of leakage current. Table E.5 shows the corresponding test matrix.

Table E.5. Snapshot Numbers For Diode Fault Tests

Load	Diode Fault							
	S.C.	O.C	R=1 Ω	R=2 Ω	R=3 Ω	R=4 Ω	R=5 Ω	R=6 Ω
No load	60,61	70,71	80,81	90,91	100,101	110,111	120,121	130,131
1200 W	62,63	72,73	82,83	92,93	102,103	112,113	122,123	132,133
2400 W	64,65	74,75	84,85	94,95	104,105	114,115	124,125	134,135
3600 W	66,67	76,77	86,87	96,97	106,107	116,117	126,127	136,137
No load	68,69	78,79	88,89	98,99	108,109	118,119	128,129	138,139

The stator fault uses two 16-ohm, 6-A, 576-W slide resistors to short several windings in one stator leg. This shunt resistance is gradually lowered to simulate a short circuit in the stator leg. The test protocol is as follows: (a) reconnect the 50-ohm shunt resistor; (b) connect the load to the generator set; (c) connect resistors in series to terminals T-31 to T-35 on terminal block for line 3. The leakage current should not exceed 12 A. Table E.6 shows the corresponding test matrix.

The stator fault test data files also are listed in Table E.6. During the stator fault test, we monitored the resistor value during the test and noticed thermal drift in the resistance value. Table E.7 shows the measured resistor values. The resistor values appear to drift monotonically with time (increasing snapshot number). For a give load condition, the actual resistance corresponding to each snapshot should be consistently decreasing although there is clearly some uncertainty in the actual resistance used in the fault simulation.

Table E.6. Stator Fault Test Snapshot Numbers

Load	Stator Fault Condition (Resistance, Ohms)											
(W)	33Ω	27 Ω	21 Ω	15 Ω	9 Ω	6 Ω	5 Ω	4 Ω	3 Ω	2 Ω	1 Ω	.8 Ω
0	140, 141	150, 151	160, 161	170, 171	180, 181	190, 191	200, 201	210, 211	220, 221	230, 231	240, 241	250, 251
1200	142, 143	152, 153	162, 163	172, 173	182, 183	192, 193	202, 203	212, 213	222, 223	232, 233	242, 243	252, 253
2400	144, 145	154, 155	164, 165	174, 175	184, 185	194, 195	204, 205	214, 215	224, 225	234, 235	244, 245	254, 255
3600	146, 147	156, 157	166, 167	176, 177	186, 187	196, 197	206, 207	216, 217	226, 227	236, 237	246, 247	256, 257
0	148, 149	158, 159	168, 169	178, 179	188, 189	198, 199	208, 209	218, 219	228, 229	238, 239	248, 249	258, 259

Table E.7. Stator Fault Resistor Values

Load	Stator Fault Condition (Resistance, Ohms)											
(W)	33Ω	27 Ω	21 Ω	15 Ω	9 Ω	6 Ω	5 Ω	4 Ω	3 Ω	2 Ω	1 Ω	.8 Ω
0	33	27	21	15	9	6.01	4.98	4.01	3.02	2.003	1.0	.79
1200	33	27	21	15	9	6.14	5.28	4.19	3.27	2.37	1.41	1.43
2400	33	27	21	15	9	6.32	5.57	4.55	3.63	2.77	1.80	1.96
3600	33	27	21	15	9	3.40	5.68	4.73	3.81	3.00	2.21	2.30
0	33	27	21	15	9	6.48	5.72	4.91	4.01	3.19	2.47	2.51

APPENDIX F. INTELLECTUAL PROPERTY FOR THE ORNL NONLINEAR TECHNOLOGY

1. L. M. Hively, "Methods for Improved Forewarning of Critical Events Across Multiple Data Cannels," patent pending (ORNL ERID# 1300) submitted to U.S. Patent Office (September 22, 2003).

2. L. M. Hively, P. C. Gailey, V. A. Protopopescu, "Condition Assessment of Nonlinear Processes," U.S. Patent #6,484,132 (November 19, 2002).

3. D. E. Welch, L. M. Hively, and R. F. Holdaway, "Nonlinear Prediction of Fatigue Failure," U.S. Patent #6,460,012 (October 1, 2002).

4. L. M. Hively, "Methods for Consistent Forewarning of Critical Events Across Multiple Data Channels," patent pending (ORNL ERID#0885) submitted to U.S. Patent Office (July 12, 2002).

5. L. M. Hively, N. E. Clapp, C. S. Daw, W. F. Lawkins, "Epileptic Seizure Prediction by Nonlinear Methods," U.S. Patent #5,857,978 (January 12, 1999).

6. L. M. Hively and E. G. Ng, "Integrated Method for Chaotic Time Series Analysis," U.S. Patent #5,815,413 (September 29, 1998).

7. L. M. Hively, N. E. Clapp, C. S. Daw, W. F. Lawkins, "Apparatus and Method for Epileptic Seizure Detection using Nonlinear Techniques," U.S. Patent #5,743,860 (April 28, 1998).

8. N. E. Clapp, L. M. Hively, "Method and Apparatus for Extraction of Low-Frequency Artifacts from Brain Waves for Alertness Detection," U.S. Patent #5,626,145 (May 6, 1997).

APPENDIX G. PUBLICATIONS ON MACHINE FAILURE FOREWARNING UNDER THIS PROJECT

L. M. Hively, V. A. Protopopescu, and M. Maghraoui "NERI2000-109 Project Review," invited presentation to DOE/NE-20 at ORNL (July 25, 2001).

L. M. Hively, V. A. Protopopescu, M. Maghraoui, and J. W. Spencer, "Annual Report for NERI Proposal #2000-0109 on Forewarning of Failure in Critical Equipment at Next-Generation Nuclear Power Plants," ORNL/TM-2001/195 (November 2001).

L. M. Hively, V. A. Protopopescu, "NERI2000-109 Project Review," invited presentation of FY02 project at U.S. Department of Energy, Germantown Headquarters to NE-20 staff (October 16, 2002).

L. M. Hively, "Forewarning of Failure in Critical Equipment at Next-Generation Nuclear Power Plants," FY02 annual summary of NERI2000-109 project to DOE/NE20 (October 22, 2002).

L. M. Hively and V. A. Protopopescu, "Forewarning of Failure in Critical Equipment at Next Generation NPP," Annual Report for NERI2000-109 project, ORNL/TM-2002/183, Oak Ridge National Laboratory (February 2003).

V. Protopopescu, J. Barhen, Y. Braiman, and L. M. Hively, "Predictability and Control Issues in Complex Dynamical Systems," presentation to DOE/NSF/SIAM Workshop on Predictability of Complex Phenomena, Santa Fe, New Mexico, December 16−18, 2002.

L. M. Hively, "Forewarning of Failures in Critical Equipment at Next Generation Nuclear Power Plants," invited presentation to DOE/NE-20 and peer reviews at Rockville, MD (20 May 2003).

V. A. Protopopescu and L. M. Hively, "Forewarning of Machine Failure via Nonlinear Analysis," *Proc. ANS* (June 2003).

T. Haywood, "Graphical User Interface for Nonlinear-Condition Assessment," draft of ORNL/TM (2003).

L. M. Hively and V. A. Protopopescu, "Machine Failure Forewarning via Phase-Space Dissimilarity Measures," accepted for publication in *Chaos* (2003).

L. M. Hively, V. A. Protopopescu, K. M. Reichard, and, K. Maynard, "Failure Forewarning in NPP Equipment – NERI2000-109 Final Project Report," ORNL/TM-2003/222, Oak Ridge National Laboratory (2003).

APPENDIX H. RECENT PUBLICATIONS ON FOREWARNING OF STRUCTURAL FAILURES AND BIOMEDICAL EVENTS

D. E. Welch, L. M. Hively, R. F. Holdaway, "Nonlinear Crack Growth Monitoring," *Proc. 2000 ASM Materials Solutions Conference and Exposition* (October 11, 2000) St. Louis, Missouri.

D. E. Welch, L. M. Hively, R. F. Holdaway, "Nonlinear Crack Growth Monitoring," *Proc. Int'l Mech. Engr. Congress and Exposition* (November 5−10, 2000) Orlando, Florida.

L. M. Hively, N. E. Clapp, V. A. Protopopescu, J. Joseph, C. E. Merican, T. Lucht, "Epileptic Seizure Forewarning by Nonlinear Techniques," ORNL/TM-2000/333, Oak Ridge National Laboratory (November 2000).

L. M. Hively, V. A. Protopopescu, P. C. Gailey, "Timely Detection of Dynamical Change in Scalp EEG Signals," *Chaos* 10 (December 2000) 864−875.

D. E. Welch, L. M. Hively, R. F. Holdaway, "Nonlinear Crack Growth Monitoring," *Proc. 33rd National Symp. On Fracture and Fatigue*, Moran, Wyoming (June 2001).

L. M. Hively, N. E. Clapp, V. A. Protopopescu, "Forecasting Epileptic Seizures," *ORNL Review* 33, No. 2 (2000) 21.

V. A. Protopopescu, L. M. Hively, P. C. Gailey "Epileptic event forewarning from scalp EEG," invited review paper in *J. Clin. Neurophysiol.* 18 (May 2001) 223−245.

L. M. Hively, V. A. Protopopescu, J. Joseph, "CRADA Final Report for CRADA Number ORNL99-0559 – Epileptic Seizure Forewarning by Nonlinear Techniques," C/ORNL99-0559, Oak Ridge National Laboratory (January 2002).

L. M. Hively, "Forewarning of Medical Events," invited presentation to ORNL/OTT Conference on Overcoming Barriers Facing Persons with Disabilities Through the Applications of Technologies, Roane State Community College (July 16, 2002).

L. M. Hively, "Nonlinear Analysis of Physiological Data for Event Forewarning," invited presentation to weekly Biomedical Engineering seminar at University of Kentucky, Louisville, KY (September 16, 2002).

L. M. Hively, V. A. Protopopescu, N. B. Munro, "Prediction of Sepsis Onset in Trauma Victims Using Advanced Nonlinear Analysis," FY02 Progress report to ORNL LDRD Manager (October 3, 2002).

L. M. Hively, "Forewarning of Biomedical Events via Nonlinear Analysis of Physiologic Data," one page abstract to DOE Office of Medical Science for 2003 summary booklet (January 30, 2003).

L. M. Hively and V.A. Protopopescu, "Detection of Changing Dynamics in Physiological Time Series," presentation and *Proc. ANS Conf. on Nucl. Math. Computational Sci.* (Gatlinburg, TN) April 6−11, 2003.

L. M. Hively and V. A. Protopopescu, “Need for High Performance Computing in Analysis of Biomedical Data,” invited presentation to Cray Biology Workshop at Oak Ridge National Laboratory (May 9, 2003).

L. M. Hively and V. A. Protopopescu, “Channel-Consistent Forewarning of Epileptic Events from Scalp EEG,” *IEEE Trans. Biomed. Engr.* 50 (May 2002) 584−593.

L. M. Hively, V. A. Protopopescu, N. B. Munro “Detection of Changing Dynamics in Physiological Time Series for Biomedical Event Forewarning,” *Biomed. Engr. Soc. Mtg.* Nashville, TN, October 03, 2003.

APPENDIX I. DEVELOPMENT OF GRAPHICAL USER INTERFACE

I.1 INTRODUCTION

ORNL has developed and patented a model-independent methodology to assess condition change in complex systems from noisy, process-indicative data of limited precision and modest length. Condition change is typically indicative of impending machine failure or biomedical event (e.g., epileptic seizure or breathing difficulty). Practical use of this technology for machine and biomedical applications will require a user-friendly GUI. This report describes the development of the first essential GUI function, namely graphical presentation of the analysis results. Subsequent sections explain the functional requirements, software design, implementation, testing, and demonstration of the GUI for visualization of representative results.

I.2 FUNCTIONAL REQUIREMENTS

The user-friendly GUI features include clear presentation of the results and an intuitively obvious use that requires little or no user training. The GUI should be implementable on many different computer platforms that run various operating systems. Remote access should also be possible via Internet.

I.3 SOFTWARE DESIGN

The use of the commercial MATLAB^{TM} software for construction of the GUI satisfies all of the functionality requirements for creating plots, images, surfaces, and volumetric representations. MATLAB implements GUIs as windows containing various control objects, such as pushbuttons, pull down menus, and toggle buttons, that can be used for implementation of functions such as saving a plot. Each object must be programmed separately to perform the intended action. These tasks are simplified by GUIDE, MATLAB's Graphical User Interface Development Environment. The specific design involves buttons to select the type of plot, a menu to choose the appropriate data file for plotting, and buttons for saving the plot, and termination of the GUI.

I.4 IMPLEMENTATION

GUI implementation involves two basic tasks: laying out the options on the GUI control panel and programming the function(s) of each GUI component. GUIDE includes a set of layout tools. GUIDE also generates a procedure file (called an “M-file” or MATLAB file) that contains code to handle the initialization and launching of the GUI. This M-file provides a framework for the implementation of the callbacks, which are the active GUI functions. GUIDE allows interactive layout of the components, and generates two files that save and launch the GUI. The first is a FIG-file that contains a complete description of the GUI figure and all of its attributes, as well as the values of all object properties. The second is an M-file that contains the (sub)functions that launch and control the GUI and the callbacks.

After launching the GUI, five push buttons appear on the right-hand side of the top-level menu (Fig. I.1), corresponding to plots for the five different kinds of data. The user clicks on one of the push buttons for the corresponding data plot. A file selection box then appears. The user next clicks on the appropriate file for plotting from this file selection box. The GUI extracts the

numerical data from that file and displays the resulting plot on the GUI screen. Two additional choices appear on the GUI menu under the "Options" button. One is for printing or saving the plot to a file in a chosen format. The user then can import the file into MS-Word™ or PowerPoint™. The other button closes the GUI.

I.5 RESULTS AND TESTING

This section shows examples of the data plots for five different types of data. Figure I.1 shows the completed top level GUI screen. Figure I.1 also shows the dialog box that appears for selection of a file for plotting. The top button on the far right of the GUI screen with the label, "3_Chan_Raw" plots the data as shown in Fig. I.2. The second button, "1_Chan_Raw," plots the data as shown in Fig. I.3. The third button, "Trad_NLM", plots the data as shown in Fig. I.4. The fourth button, "PSDM," plots the data as shown in Fig. I.5. The fifth button, "Data Quality," plots the data as shown in Fig. I.6.

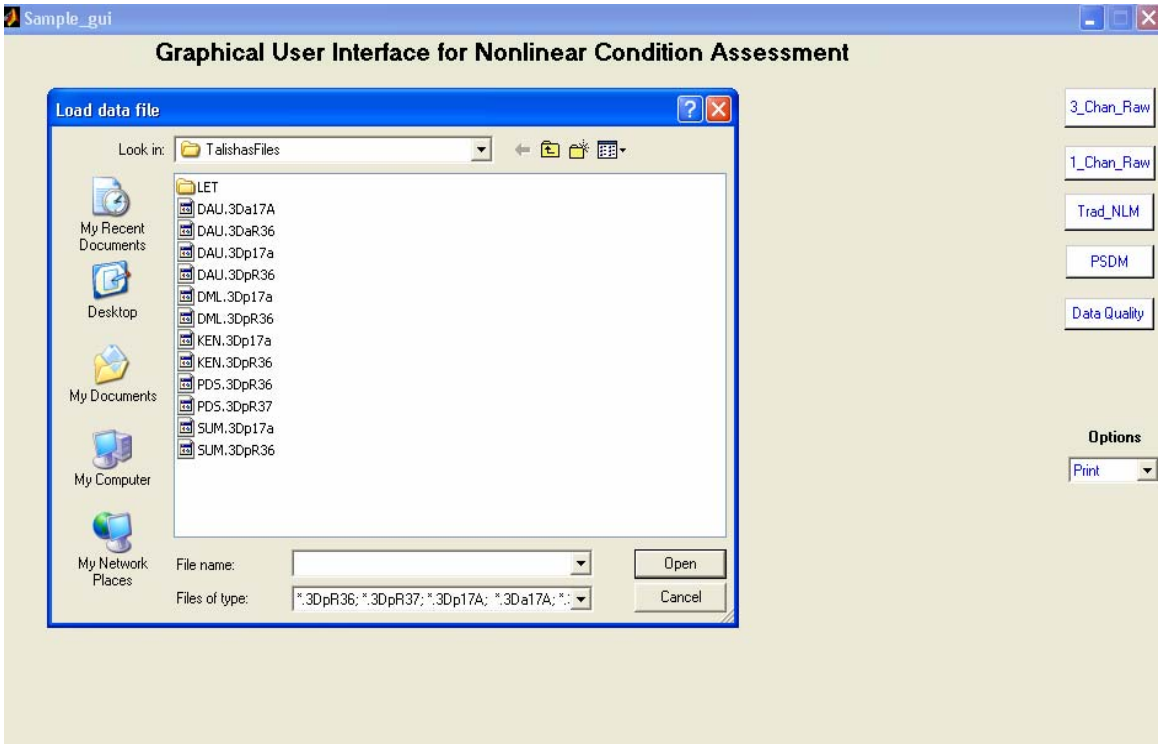

Fig. I.1. Display of the GUI when a plot push-button is clicked.

Figure I.2 shows raw tri-axial accelerometer data in three orthogonal directions, corresponding to each of the three columns. The top row shows roughly one second of data for each of the three channels at a sample rate of 52 kHz. The second row shows more detail in the same data over 200 ms for each channel. The third row shows still more detail for each of the three channels over roughly 40 ms. The bottom plot in Fig. I.2 shows the most detail in complex, nonlinear waveforms for each of the three channels over roughly 8 ms.

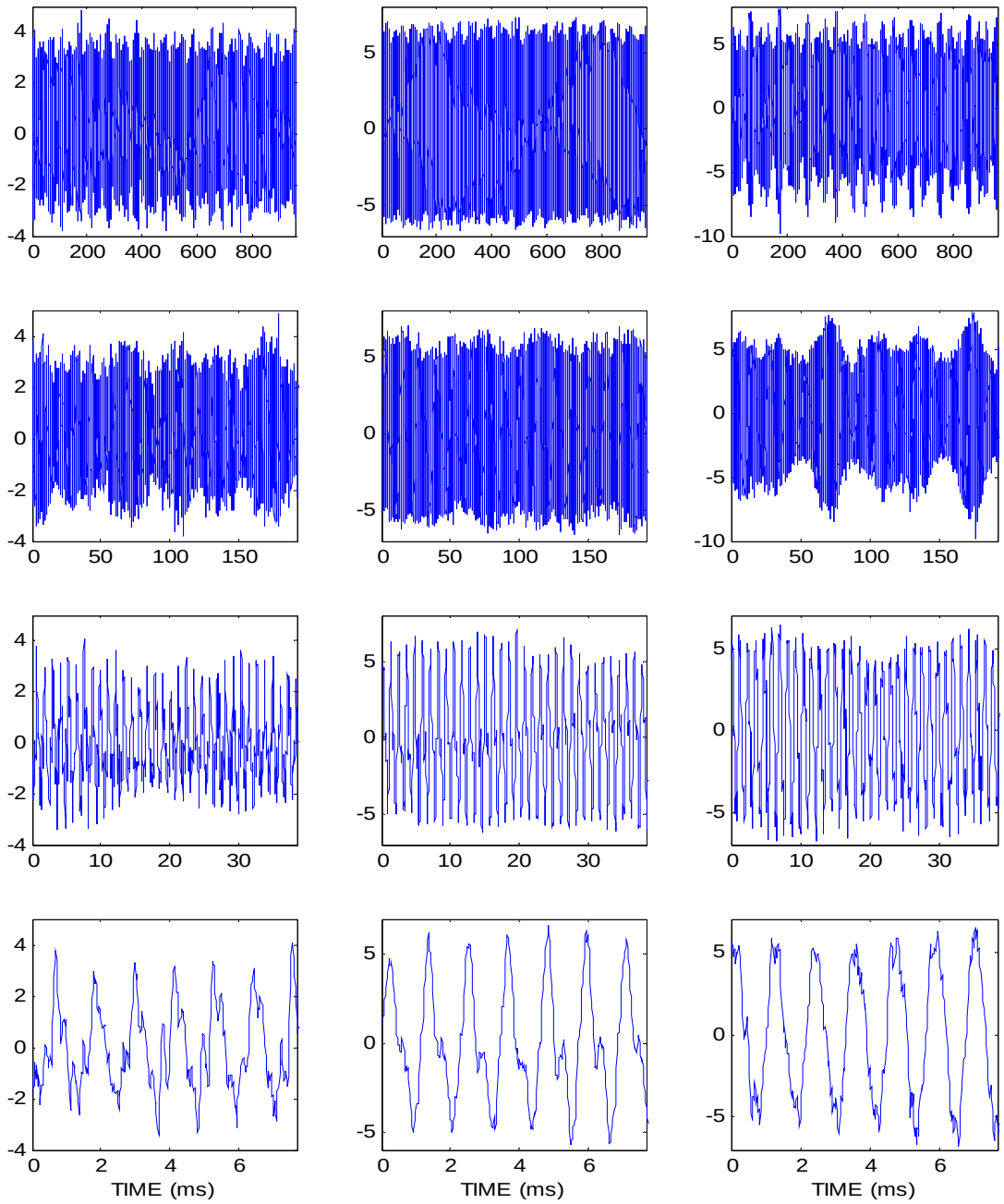

Fig. I.2. Plot of tri-axial accelerometer data (columns) over successively shorter time intervals (row from top to bottom).

Figure I.3 shows the complex, nonlinear features in vibration power over the same successively shorter time intervals as in Fig. I.2. This single-channel of power data was obtained from the tri-axial accelerometer data via the following combination of calculus and elementary mechanics. Acceleration, $\underline{\mathbf{a}}$, is a three dimensional vector that can be integrated once in time to give velocity, $\underline{\mathbf{v}}$. Mass, m, multiplied by acceleration equals force vector, $\underline{\mathbf{F}} = m\underline{\mathbf{a}}$. The vector dot product of force and velocity is scalar vibration power, $P = \underline{\mathbf{F}} \bullet \underline{\mathbf{v}}$. Vibration power captures the dynamical features of all three acceleration directions in a single scalar signal vs time.

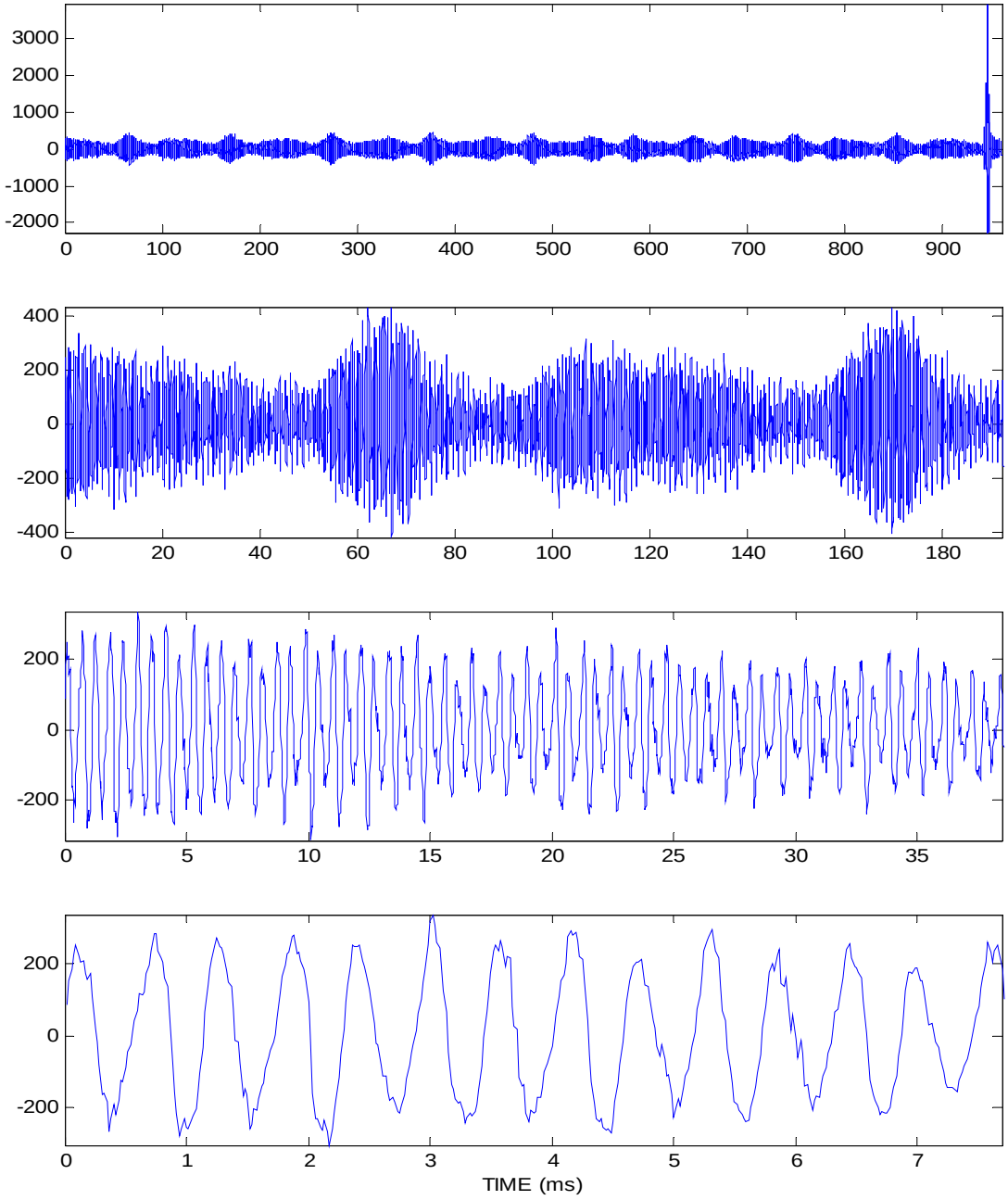

Fig. I.3. Plot of single-channel raw data over successive shorter timescales.

Figure I.4 shows a plot of three traditional nonlinear measures versus time. The top subplot is the correlation dimension, *D*, which is a measure of the data complexity. *D* is a decimal number, which, when rounded up to the next higher integer, indicates the number of simultaneous ordinary differential equations required to model the process dynamics adequately. The middle plot is the Kolmogorov entropy, *K*, which measures the rate of information lost per unit time (in BITS/s), or the degree of predictability. The bottom plot shows the value of the first minimum in the mutual information function (MIF), which is a nonlinear version of the (linear) autocorrelation function. MIF measures the average information (in bits) that can be inferred from one measurement about a second measurement as a function of the time delay between the observations. The first minimum in MIF, M_1, is a measure of the nonlinear decorrelation time between the two signals.

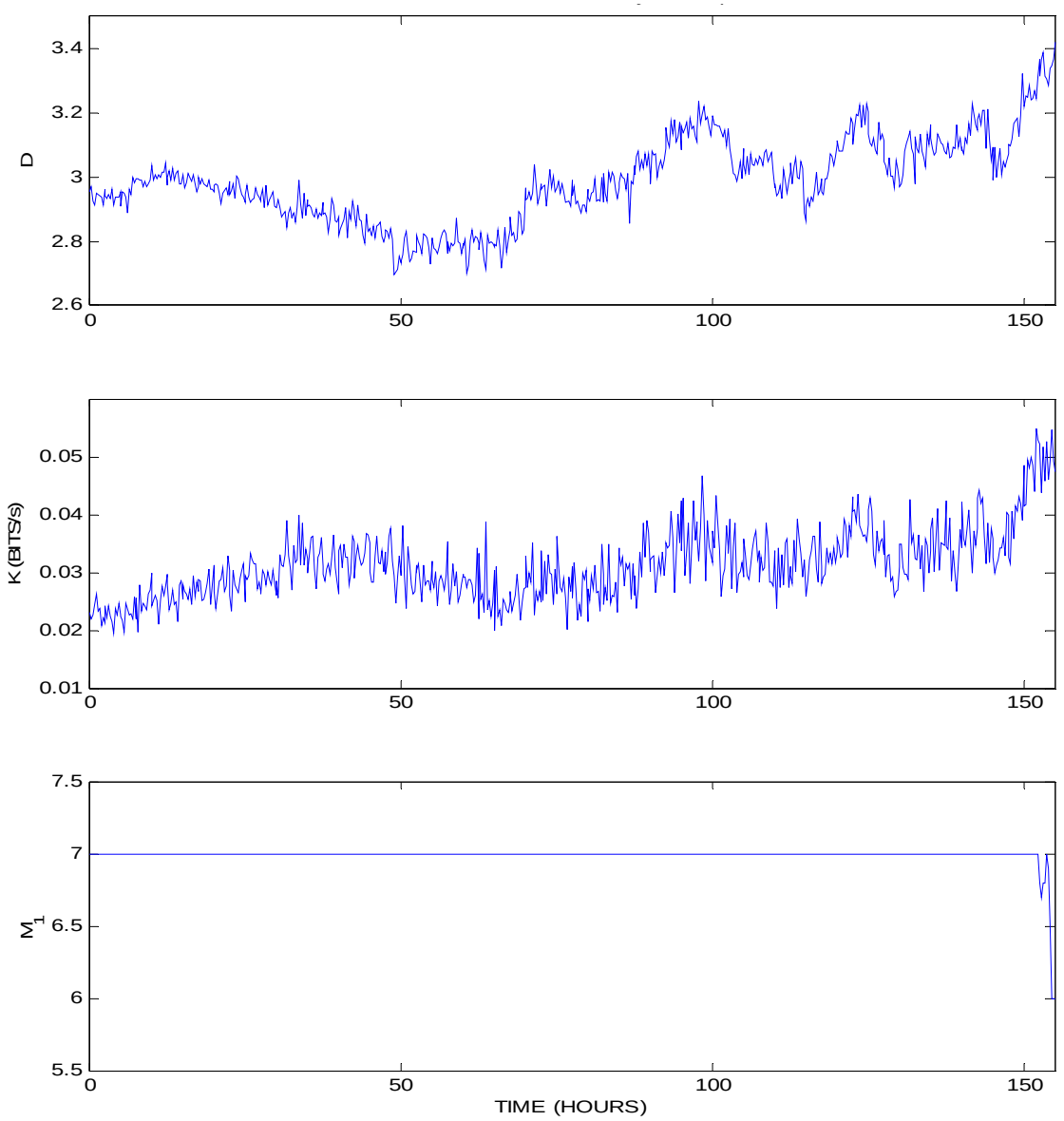

Fig. I.4. Plot of three traditional nonlinear measures: correlation dimension (top), Kolmogorov entropy (middle), and first minimum in the mutual information function (bottom).

Figure I.5 shows measures of condition change. The time-serial vibration power data in Fig. I.3 were converted to a discrete distribution function (DF) that captures the essential features of the underlying dynamics. Condition change assessment compares test case DFs to a base case (nominal state) DF via novel measures of dissimilarity. Forewarning is indicated by several sequential occurrences of the dissimilarity measures above a threshold. While traditional nonlinear measures compare averaged (global) quantities, the enhanced discrimination power of these measures is achieved by focusing on the absolute difference between the two DFs.

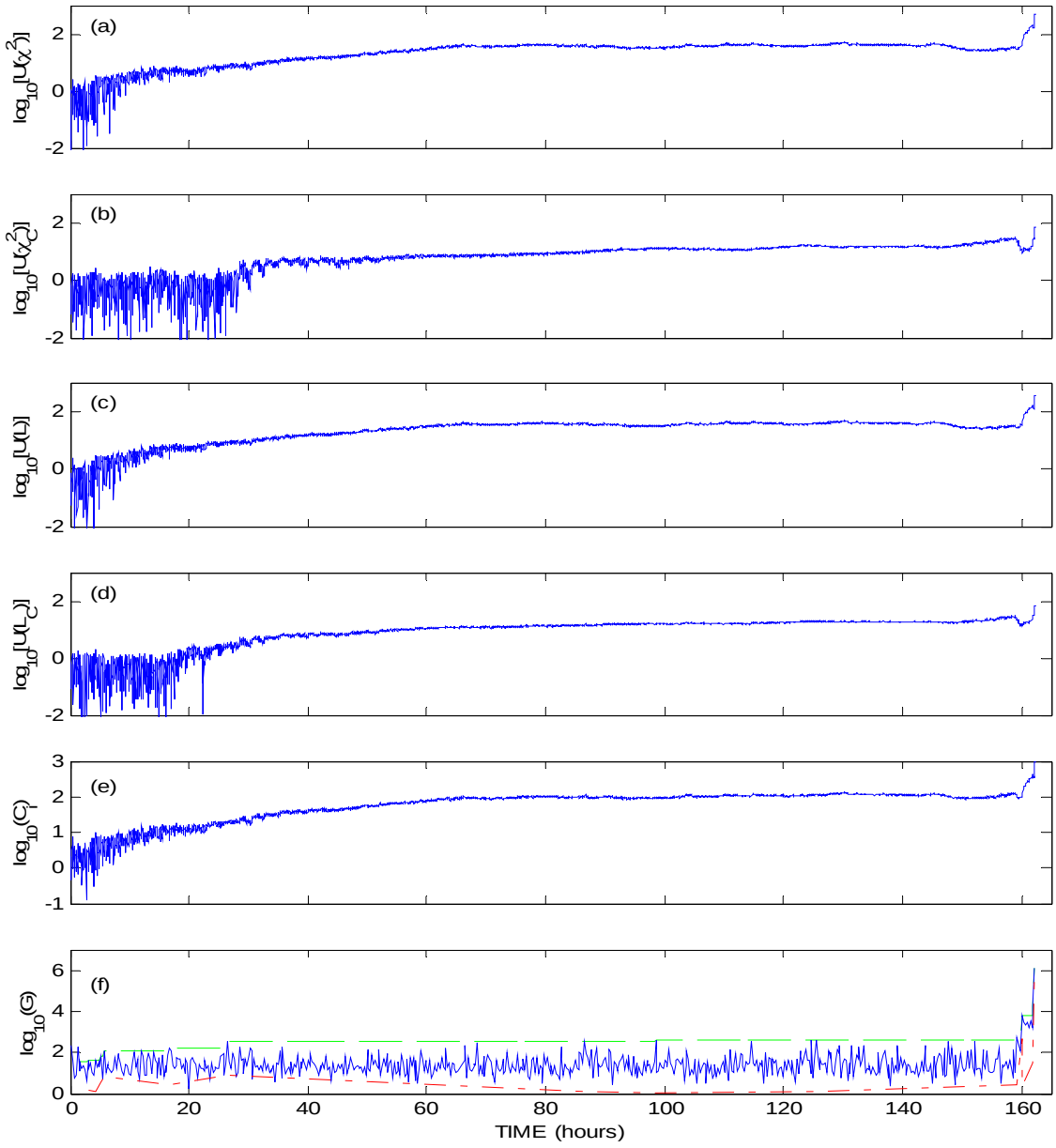

Fig. I.5. Measures of condition change vs time: (subplots a-d) four phase-space measures of dissimilarity between the DFs for baseline dynamics and subsequent test states; (e) composite measure, namely the sum of the measures from subplots (a)-(d); and (f) statistical criteria for forewarning of failure, based on a straight-fit to the data in subplot (e).

Figure I.6 illustrates results that assure adequate data quality for the above analyses. This analysis first sorts the time-serial data into ascending order, from the smallest to largest value. This sorted sequence is then converted into a histogram of occurrence frequency vs each unique signal value in the raw data. The left subplot shows the result, indicating a problem with singlet occurrences of signal values for both the largest and smallest values. The first difference of these sorted values is next obtained, sorted, and plotted as a histogram, as before. The result is the right subplot, which shows the expected result of many small increments between successively larger signal values and few large differences.

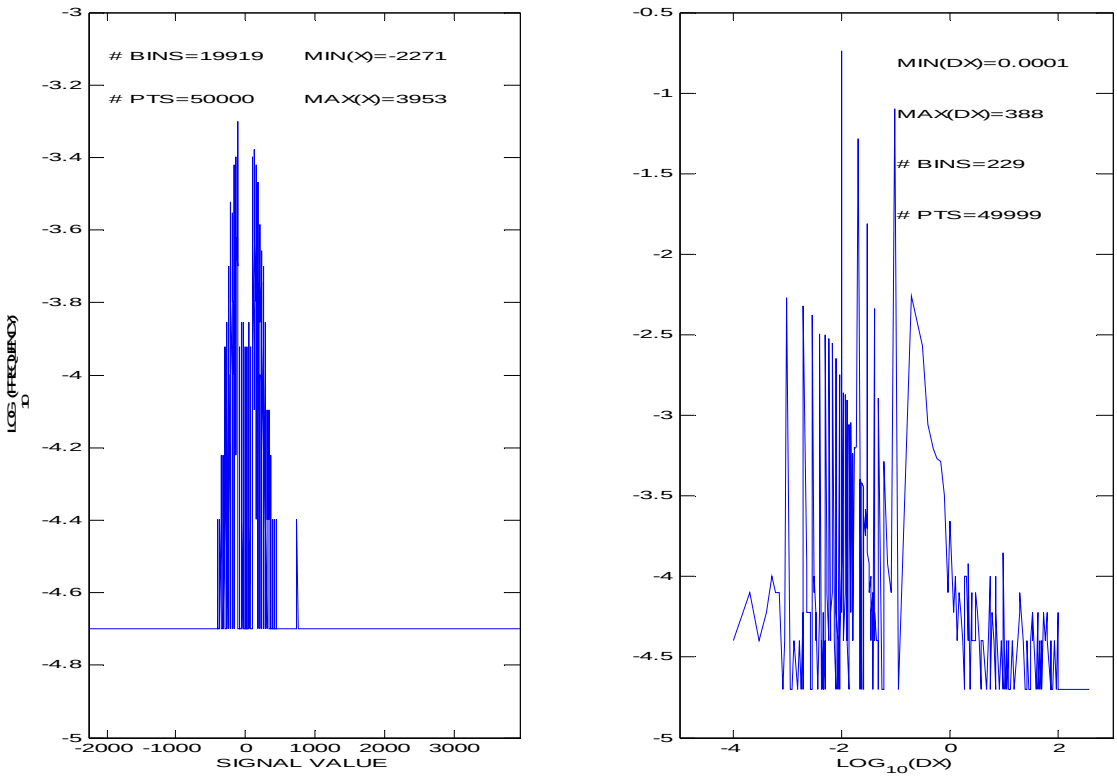

Fig. I.6. Plot of data quality measures.

I. 6 TESTING/RESULTS

Each data file was tested individually to assure that the GUI was functioning properly. When the user selects a particular type of visualization and the corresponding data file, the GUI generates the appropriate plot. The user has the choice of printing the plot or saving it to desired file.

INTERNAL DISTRIBUTION

1. R. K. Abercrombie
2. D. M. Hetrick
3-7. L. M. Hively
8. T. Sjoreen
9. T. D. Vane
10. B. A. Worley
11. Central Research Library
12. ORNL Laboratory Records – RC
13. ORNL Laboratory Records – OSTI

EXTERNAL DISTRIBUTION

14. Jan Stein, Electric Power Research Institute, P.O. Box 10412, Palo Alto, CA94303-0813